EXPERIMENTAL VERIFICATION OF MONTE CARLO CALCULATED DOSE DISTRIBUTIONS FOR CLINICAL ELECTON BEAMS

by

ROBERT DOUCET JR.

Medical Physics Unit
McGill University, Montreal
November 2001

A thesis submitted to the
Faculty of Graduate Studies and Research
in partial fulfilment of the requirements
of the degree of Master of Science

Abstract

Current electron beam treatment planning algorithms are inadequate to calculate dose distributions in heterogeneous phantoms. Fast Monte Carlo algorithms are accurate in general but their clinical implementation needs validation. Calculations of electron beam dose distributions performed using the fast Monte Carlo system XVMC and the well-benchmarked general-purpose Monte Carlo code EGSnrc were compared with measurements. Irradiations were performed using the 9 MeV and 15 MeV beams from the Clinac 18 accelerator with standard conditions. Percent depth doses and lateral profiles were measured with thermoluminescent dosimeter and electron diode respectively. The accelerator was modelled using EGS4/BEAM, and using an experiment-based beam model. All measurements were corrected by EGSnrc calculated stopping power ratios. Overall, the agreement between measurement and calculation is excellent. Small remaining discrepancies can be attributed to the non-equivalence between physical and simulated lung material, precision in energy tuning, beam model parameters optimisation and detector fluence perturbation effects.

Résumé

Présentement, les algorithmes pour la planification des traitements par faisceaux d'électrons sont inadéquats pour le calcul des distributions de dose dans des phantômes hétérogènes. Les algorithmes de Monte Carlo rapides sont adéquats en général mais leur implémentation clinique nécessite une validation. Les distributions de dose pour des faisceaux d'électrons calculés utilisant le système de Monte Carlo rapide XVMC et le système d'usage général EGSnrc ont été comparées à des mesures expérimentales. Les irradiations ont été performées en utilisant les faisceaux d'électrons d'énergie 9 MeV et 15 MeV de l'accélérateur Clinac 18 selon les paramètres standards. Les rendements en profondeur et les profils latéraux ont été respectivement mesurés avec des dosimètres thermoluminescents et des diodes à électrons respectivement. L'accélérateur a été simulé en utilisant EGS4/BEAM, et en utilisant un modèle de faisceaux basé sur des mesures expérimentales. Toutes les mesures ont été corrigées par les rapports de pouvoir d'arrêt calculés avec EGSnrc. En général, l'accord entre les mesures et les calculs est excellent. Les légers désaccords peuvent être attribués à la non-équivalence entre le matériel d'imitation de poumons utilisé et celui simulé, à la précision dans l'optimisation de l'énergie, à la précision dans l'optimisation des paramètres du modèle de faisceaux et à la perturbation du flux causée par la présence du détecteur.

Acknowledgements

My sincere gratitude goes to my supervisor Dr. Jan P. Seuntjens. His enthusiasm, expertise, availability and good supervision skills made my work with him a very good experience.

I would also like to express my sincere recognition to Dr. Ervin B. Podgorsak. His encouragements and his high demands throughout my studies are greatly appreciated.

I also thank Michael Evans, Russell Ruo and Kristin Stewart for their help at some points in the experiments. I would also like to acknowledge Dr. François DeBlois and Wamied Abdel-Rahman for their help in various computer-related aspects and Monte Carlo calculations. I also want to thank Yanic Bercier, Jennifer Barker, Russell Ruo, and Kristin Stewart for their help on writing the thesis and Margery Knewstubb for her administrative help during my studies. My acknowledgements also go to Marina Olivares for her guidance in my use of thermoluminescent dosimeters and Shoukry Aboulehaf for machining various pieces of equipment used in this work.

I would also like to thank Dr. François DeBlois, Wamied Abdel Rahman and Kristin Stewart for sharing the student lab with me and making it a nice environment.

Last but not least, I would like to express my thankfulness to my parents Georgette and Robert. Without their constant love and support I would have never gone this far.

Table of Contents

Chapter 1

Introduction

I Radiotherapy

In Canada, cancer is the most severe health problem in terms of the number of years of life lost[1]. In the year 2001, the diagnosis of 134,100 new cancers[1] and 65,300 deaths due to cancer are expected[1]. The most popular cancer treatments are either radiotherapy, chemotherapy or surgery, alone or a combination of these modalities.

The goal of radiotherapy, which involves the use of ionising radiation, is to give a large amount of radiation to the tumour while minimising the amount of radiation given to surrounding healthy tissues in order to reduce complications.

Ionising radiation interacts with the medium by depositing energy either directly or indirectly. Directly ionising radiation consists of charged particles that deposit their energy in the medium by creating excitations and ionisations of the atoms due to the Coulomb force between the charged particles and the orbital electrons or nucleus of the atoms. Indirectly

ionising radiation, on the other hand, consists of neutral particles such as photons and neutrons. These neutral particles must first create charged particles that will proceed to ionise the medium directly and deposit their energy. The most important photon interactions are the photoelectric effect, Compton effect and pair production which release high energy electrons and positrons while neutrons mostly interact with the nuclei of atoms in the medium and eject charged particles such as protons and alpha particles.

In biological systems, the interactions of ionising radiation can be direct or indirect. During indirect interactions, ionising radiation interacts with water molecules liberating aqueous electrons, hydroxyl radicals, hydrogen radicals which then interact with the DNA in a cell. In direct interactions, the ionising radiation interacts directly with the DNA. It is believed that the damages to the DNA, more precisely double-strand breaks, are the primary cause of radiation induced cell killing[2].

Radiotherapy treatments can be given as either external beam therapy or brachytherapy. Brachytherapy deals with the insertion of radioactive sources into the patient and in principle, is the best solution because it provides better sparing of the healthy tissues since the radiation sources are closer to the tumour. However, external beam therapy is the most common modality and can deliver either photon or electron beam therapies. Electron beam therapy is mostly used to treat superficial lesions.

The sequence of a treatment typically consists of many steps including patient diagnosis, tumour staging, image acquisition (usually from computed tomography), delineation of the target and critical structures, treatment planning, and finally treatment. A discussion on treatment planning systems will be presented in Section III. The desired accuracy of a treatment should be within 5%[3] with a recommended accuracy of 2.5% for each of the following steps[4]: determination of absorbed dose to water at a reference point, determination of relative dose, calculation of relative dose, and patient irradiation.

II Radiation dosimetry techniques

Radiation dosimetry deals with the measurement of absorbed dose. The absorbed dose D represents the amount of energy absorbed per unit mass and is given in units of Gray (Gy), where 1Gy = 1 J/Kg.

One usually considers two types of dosimeters. Dosimeters, which are capable of measuring absorbed dose (or exposure) in absolute terms can serve as so-called *reference dosimeters*. Dosimeters that only provide information on the variation of absorbed dose relative to some reference point, are termed *relative dosimeters*.

The traditional reference dosimeters are the (water) calorimeter, the free-air ionisation chamber, the cavity ionisation chamber, the extrapolation (or gradient) chamber and the Fricke dosimeter. Of these dosimeters, only the calorimeter can be considered as an *absolute* instrument for the realisation of the quantity absorbed dose since the instrument can be fully characterised without the use of ionising radiation hence allowing the measurement of absorbed dose according to its definition. The free-air ionisation chamber is an absolute instrument for the realisation of the quantity exposure (C/kg). However, both the cavity ionisation chamber and the extrapolation chamber require the knowledge of the energy required to produce an ion pair, W_{air}, which cannot be determined in the absence of ionising radiation. Similarly, the Fricke dosimeter requires the knowledge of the radiation chemical yield G. However, with accepted values of W_{air} or G these latter dosimeters are perfectly suited to measure absorbed dose at a reference point.

Cavity ionisation chambers are also used as relative dosimeters and in that context are denoted briefly as ionisation chambers. The other clinically important relative dosimeters are films, diodes and thermoluminescent dosimeters. The most common measurements performed with relative dosimeters are depth doses and lateral profiles. A depth dose represents the relative dose at different points as a function of depth. Lateral profiles represent the relative dose as a function of lateral displacement at a fixed depth.

In this thesis, the work was performed with ionisation chambers, diodes and thermoluminescent dosimeters. These techniques will be discussed in more detail.

II.A Ionisation chamber

Ionisation chambers are the most widely used dosimeters and consist of different configurations: parallel-plate, cylindrical and spherical. Figure 1- 1 shows a diagram of a parallel-plate chamber with its operating circuit.

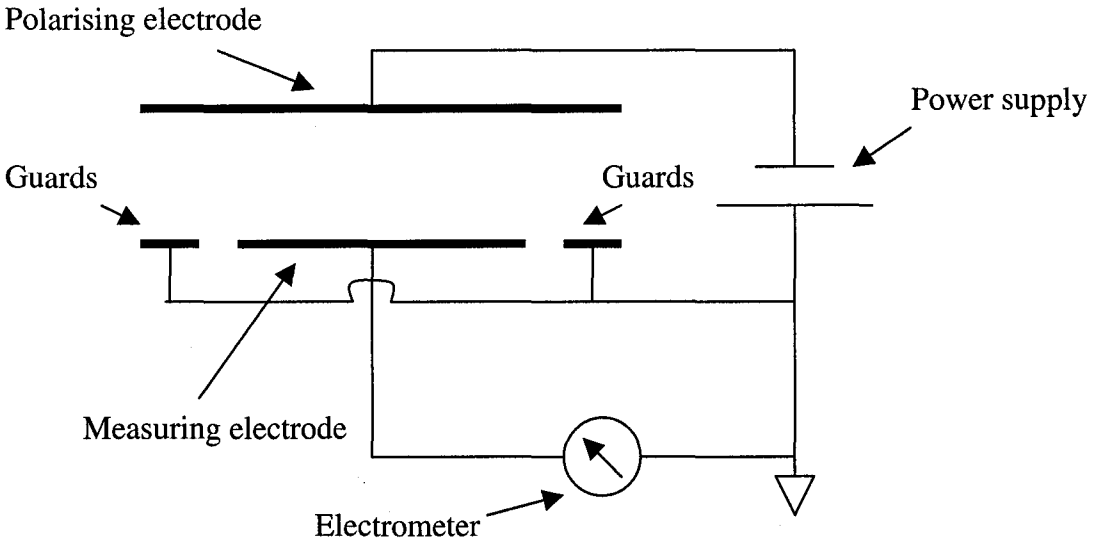

Figure 1- 1. Diagram of a parallel-plate chamber and its operating circuit.

The chamber is composed of a polarising electrode connected to a power supply, a measuring electrode and two guard electrodes. The roles of the guard electrodes are to prevent the leakage current from being measured and to allow for a uniform electric field across the sensitive volume of the chamber. A wall surrounding the chamber is made of a material with absorption and scattering properties similar to the phantom to minimise the differences in scatter and attenuation. When the chamber is placed in the medium in the presence of radiation, positive and negative ions are formed in the gas cavity of the chamber, which is

typically air. The ions are collected at the measuring electrode due to the presence of the electric field between the two electrodes. The ratio of the charge collected to the mass of air can be converted to dose in the gas using $\overline{W}_{air}$, the average energy required to produce an ion pair, which has a value of 33.97 eV/ion pair in air.

In practice, the mass of air is not known and a calibration factor for the ionisation chamber is obtained from a standards lab instead. Some correction factors must be applied to the chamber reading. The most important corrections account for polarity effect, collection efficiency, non-equivalence between the wall and medium and atmospheric corrections. The dose to the medium in the absence of the detector can be related to the dose to the gas using cavity theory (see section II of chapter 2). The end-point is to determine the dose-to-water. The data required to convert a reading into absorbed dose is summarised in various protocols, the most recent of which are based on dose-to-water calibration such as the AAPM TG-51 protocol[5].

In the case of electron beam dosimetry, parallel-plate chambers are more suitable than cylindrical chambers because of their smaller sensitive volume, which is required to accurately characterise the steep fall-off in dose of electron beams.

II.B Diode

Silicon diodes have been used for photon and electron dosimetry for many years. Their main advantage is their small size due to a much higher sensitivity than a gas filled ionisation chamber (a factor of about 18 000)[6]. In typical diodes used for radiation dosimetry, the active volume is on the order of 0.3 mm^3 with a thickness between 50 and 100 μm. For their application to electron beam dosimetry, an ionisation curve measured with a silicon diode does not need to be converted to a percent depth dose curve because the stopping power ratio of water to silicon is almost constant (5% variation between 1-20 MeV). Silicon itself is a poor conductor, but it can be doped with impurities. The silicon diode can be either p-type (doped with an electron acceptor) or n-type (doped with an electron donor). It has been shown[7] that p-type diodes are a better choice for radiation dosimetry because of their smaller dependence

on dose rate and pre-irradiation level. In order to behave like a diode, a p-n junction must be present, so that in a p-type diode, a small amount of n-type material is present on one side of the p-type silicon layer. In this case, the doping level of the n-type material is very high resulting in poor collection efficiency, so only interactions in the p-type silicon are considered. Between the p and n side, there is a depletion layer with a voltage barrier of 0.7 volts.

When radiation hits the diode, electron-hole pairs are created which result in an electrical current. The signal is due to charge carriers created in the depletion layer and minority carriers (electron in a p-type and holes in an n-type) created in the base region that diffuse to the depletion layer. The latter is the most important[7]. Diodes can be operated with or without bias. If they are operated with bias, the dose is obtained from a measurement of the electrical resistance of the diode and the current is measured as a function of the biasing voltage. If the diode is operated without bias, it operates like a solar cell, a mode that is referred to as the photovoltaic mode. The voltage generated by the diode is proportional to the dose rate. This voltage leads to a current and the charge can be measured, which will be proportional to the dose. In radiation dosimetry, diodes are usually operated without bias.

II.C Thermoluminescent dosimeter (TLD)

The luminescence process consists of the emission of light by a material. One refers to the term thermoluminescence when a material needs a certain amount of heat to emit light. The thermoluminescence process is not possible in a pure material. A small amount of impurities or imperfections must be added to the material, a process referred to as doping. One of the advantages of TLDs is their small size, which permits measurements with high resolution. Also, they don't need any biasing voltage and have no dose rate dependence for the range of clinical interest. They usually come in chips or in powder, but chips are more popular because they are easier to manipulate.

In solid state physics, the energetic properties of a material are determined by the relative level of the valence band and the conduction band. In a pure material, an electron is not allowed to stay at an energy level between these two bands. If the material is doped, these

quantum mechanically forbidden energy levels become available. When radiation strikes the TLD, electron-hole pairs are formed in the valence band. These pairs acquire energy and get trapped in impurities at energy levels between valence and conduction bands. This forms a latent signal. In TLD dosimetry, thermal energy is given intentionally or by a stochastic process at room temperature to release the signal by emptying the traps. If the energy necessary for the electron to be released and fall back to its ground state is less than the energy required for the hole, their traps are respectively called storage traps and recombination centres. In the opposite case, if the energy necessary for the electron to be released and fall back to its ground state is more than the energy required for the hole, their traps are respectively called recombination centres and storage traps. Recombination will occur at the recombination centre and light will be emitted.

In the reading process, the TLD is placed on a heating planchet and the light emitted is converted into an electrical signal by a photomultiplier tube. The output of the reading process is a glow curve. A glow curve represents the thermoluminescence as a function of the temperature or as a function of time if there is a linear temperature rise. The area under the glow curve is proportional to the dose. A typical glow curve for LiF:Mg:Ti is shown in Figure 1- 2.

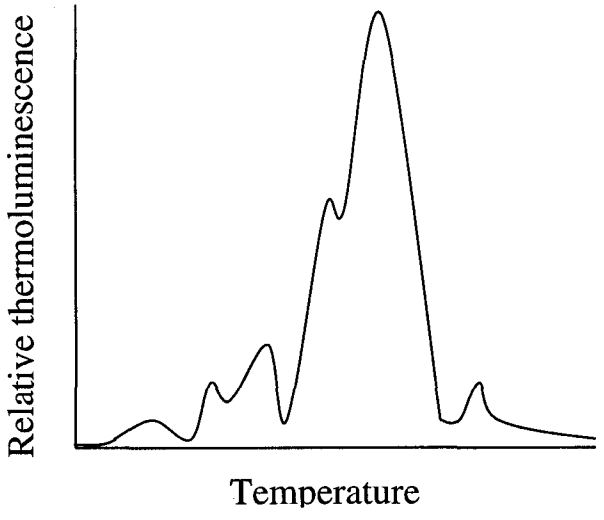

Figure 1- 2. Typical glow curve for a LiF:Mg:Ti TLD.

The probability that recombination occurs is proportional to $e^{-E/kT}$, where E is the activation energy for the specific trap in Joules, T the temperature in °K and k the Boltzman constant which is equal to 1.38×10^{-23} J/°K. There is a small probability that recombination will happen at room temperature, a process termed fading. The first and second lowest temperature peaks in Figure 1- 2 have half lives of a few minutes and a few hours respectively, and are thus unstable at room temperature. There are two ways to take this into account. One way is to perform an integration of the glow curve with certain temperature limits with special software. The second way is to wait a constant time, which would be sufficiently long so that the amplitude of the unstable peaks would be significantly reduced. After TLD reading and before the next irradiation, TLD annealing must be performed. In the annealing process, the TLDs are placed in an oven and heated to a high temperature to empty the traps that have not been emptied during the reading process. The protocol used for annealing and cool down is of extreme importance for accurate dosimetry.

The TLD response as a function of dose is linear up to a limit of about 1 Gy. Above this dose, the response becomes supralinear, which means that the TLD response starts to increase with dose faster than linearly. The response has been shown to be fairly independent of energy for photon beams except at energies below about 300 keV depending on the material of the TLD[8]. For electron beams, the response is quite independent of energy for high energy electron beams, but is lower for low energy electron beams. An energy response of 0.87 or less for low energy electrons (up to 3 MeV) in comparison to that for 25 MeV electrons has been reported[9]. It is also known that the energy dependence of TLDs is more pronounced for large TLDs. The TLDs must be calibrated individually as often as possible and ideally under the same radiation quality in which the TLDs are intended to be used. A loss of about 1.5% in sensitivity per 10 Gy of absorbed dose is typical[10]. Typically, the TLDs are cross-calibrated against a calibrated chamber.

In the context of radiation dosimetry, the most common TLD material are the LiF:Mg:Ti family, first investigated by Daniels et al[11]. LiF is an alkali halide with a density of 2.64 g/cm^3 and an effective atomic number of 8.2, which is close to normal tissue. The Harshaw company (Harshaw Chemical Company, Solon, OH) produces the popular LiF

phosphors TLD 100, TLD 600 and TLD 700 which differ in their proportion of ^{6}Li and ^{7}Li. In this thesis, the work was performed with TLD 700 and the proportions are 0.01 ^{6}Li and 99.99 ^{7}Li. The details of the procedure for using the TLDs in this work are presented in section II.A of Chapter 4.

III Treatment planning systems (TPS)

As mentioned previously, the goal of radiotherapy is to deliver a large dose to the tumour and to spare the healthy tissues. Unfortunately, a compromise has to be made and a tolerance dose, which is the maximum dose an organ can receive, must be specified. The optimal dose distribution would reduce the dose to healthy tissues and maximise the dose to the tumour. The number of beams and their configurations must be selected in order to obtain this optimal dose distribution. A treatment planning system allows one to vary the configuration of different beams in order to achieve an optimal dose distribution. Current treatment planning systems require beam data for each machine to be entered in a computer prior to planning. These data consist of central axis percent depth doses and lateral profiles at different depths. From this, for each beam, a dose matrix is obtained. The computer adds up contributions of different beams and corrects for heterogeneities. Especially for electrons, due to the large number of interactions, current algorithms are unable to predict accurately dose distributions in the presence of heterogeneities. Most of the current electron algorithms are based on pencil beam algorithms. The dose distribution in a heterogeneous phantom is calculated by superposition of pencil beams, appropriately scaled for the difference in electron density between water and the non-water heterogeneity. For this reason, heterogeneities are treated using semi-infinite slab approximation, which has been shown to produce large uncertainties when calculating dose distributions in the presence of a cavity or a dense heterogeneity[12].

Especially for electron beams, it has been shown that the Monte Carlo algorithms are the most accurate method to determine the dose distributions in the presence of heterogeneities[13,14]. Unfortunately, for many years, these algorithms could not be used clinically because they required too long calculation times. An algorithm used for treatment planning must be able to calculate dose distributions with an accuracy better than 2-2.5% in a time frame of a few minutes.

IV Rationale and structure of the thesis

In recent years, many efforts have been made to reduce the calculation times of Monte Carlo based algorithms. Over the last half decade a large amount of work has addressed the clinical implementation of Monte Carlo calculation techniques for treatment planning and the first Monte Carlo based treatment planning systems are making their way into the clinic[13,14]. Clinical Monte Carlo systems are usually based on *fast Monte Carlo* models that calculate 3-D dose distributions in a time frame of typically 1 to 2 orders of magnitude faster than conventional Monte Carlo systems such as the standard EGS4 (Electron Gamma Shower version 4)[15]. In particular, for electron beam calculations, the VMC (Voxel Monte Carlo)[16] algorithm[16] offers significant speed improvement (see Section III of Chapter 3). XVMC[17] is the photon-electron transport algorithm based on VMC (see Section III.A of Chapter 3). The accuracy of these fast algorithms is usually validated in homogeneous water phantoms against experiments or in heterogeneous phantoms against traditional Monte Carlo systems. For traditional Monte Carlo systems, experimental validation goes back one or two decades[14,18,19], well before systematic beam characterisation were available.

The main objective of this thesis is to examine the *fast Monte Carlo* system XVMC in terms of its ability to determine dose distributions in the presence of heterogeneities and to compare it to the well-benchmarked Monte Carlo system EGSnrc (Electron Gamma Shower

version 1 from the National Research Council of Canada)[20]. Also, the accuracy and speed of a dose calculation using XVMC will be investigated with the intent to use XVMC for clinical dose calculations. Dose distributions calculated with XVMC and with EGSnrc will be compared with accurate measurements in heterogeneous phantoms made of materials of clinical interest. More specifically, the dose distributions will consist of percent depth doses in solid slab phantoms and lateral profiles in water phantoms below heterogeneities.

In the second chapter, the main concepts describing the physics behind electron beam therapy are reviewed. In the third chapter, the basic concepts behind Monte Carlo techniques and the codes used in this work are discussed. In the fourth chapter, the main work of this thesis is presented. The *fast Monte Carlo* system XVMC and the general-purpose Monte Carlo code EGSnrc are evaluated against measurements. The method used is presented as well as some results of dose distributions. In the fifth chapter, a summary of the thesis is presented and some future work is suggested.

References:

[1]National Cancer Institute of Canada, "Canadian Cancer Statistics 2001," Toronto, Canada (2001).

[2]M.M. Elkind, "DNA damage and cell killing: cause and effect?," Cancer **56**, 2351-2363 (1985).

[3]ICRU, "Determination of absorbed dose in a patient irradiated by beams of X or gamma rays in radiotherapy procedures," ICRU Report 24, International Commission on Radiation Units and Measurements, Washington D.C. (1976).

[4]J. Van Dyk (editor), *The modern technology of radiation oncology : a compendium for medical physicists and radiation oncologists* (Medical Physics Pub., Madison, Wis., 1999).

[5]P. R. Almond, P. J. Biggs, B. M. Coursey *et al.*, "AAPM's TG-51 protocol for clinical reference dosimetry of high-energy photon and electron beams," Med. Phys. **26**, 1847-1870 (1999).

[6]S.M. Sze, *Physics of Semiconductor devices* (Willey, New York, 1969).

[7]G. Rikner and E. Grusell, "General specifications for silicon diodes for use in radiation dosimetry," Phys. Med. Biol. **32**, 1109-1117 (1987).

[8]A.F. McKinley, *Thermoluminescence dosimetry* (Adam Hilger Ltd, Bristol, 1981).

[9]J.G. Holt, G.R. Edelstein, and T.E. Clark, "Energy Dependance of the Response of Lithium Fluoride TLD Rods in High Energy Electron Fields," Phys. Med. Biol. **20**, 559-570 (1975).

[10]T. Kron, P. Metcalfe, and T. Wong, "Thermoluminescence dosimetry of therapeutic x-rays with LiF ribbons and rods," Phys. Med. Biol. **38**, 833-845 (1993).

[11]F. Daniels, C.A. Boyd, and D.F. Saunders, Science **117**, 343-349 (1953).

[12]I. Lax, "Inhomogeneity corrections in electron-beam dose planning. Limitations of the semi-infinite slab approximation.," Phys. Med. Biol. **31**, 879-892 (1986).

[13]C. M. Ma, E. Mok, A. Kapur *et al.*, "Clinical implementation of a Monte Carlo treatment planning system," Med. Phys. **26**, 2133-2143 (1999).

[14]K. R. Shortt, C. K. Ross, A. F. Bielajew *et al.*, "Electron beam dose distributions near standard inhomogeneities," Phys. Med. Biol. **31**, 235-249 (1986).

[15]W. R. Nelson, H. Hirayama, and D. W. O. Rogers, "The EGS4 Code system," Stanford Linear Accelerator Center Report SLAC-256 (Stanford Calif.) (1985).

[16]I. Kawrakow, M. Fippel, and K. Friedrich, "3D electron dose calculation using a Voxel based Monte Carlo algorithm (VMC)," Med. Phys. **23**, 445-457 (1996).

[17]M. Fippel, "Fast Monte Carlo dose calculation for photon beams based on the VMC electron algorithm," Med. Phys. **26**, 1466-1475 (1999).

[18]E. El-Khatib, J. Antolak, and J. Scrimger, "Evaluation of film and thermoluminecsent dosimetry of high energy electron beams in heterogeneous phantoms," Med. Phys. **19**, 317-323 (1992).

[19]J. Seuntjens, A. Van Der Plaetsen, and H. Thierens, "Comparison of measured and calculated dose distributions in lung after electron beam treatment of the chest wall," Med. Phys. **21**, 1959-1968 (1994).

[20]I. Kawrakow and D. W. O. Rogers, "The EGSnrc Code System: Monte Carlo simulation of electron and photon transport," Technical Report PIRS-701, National Research Concil of Canada, Ottawa, Canada (2000).

Chapter 2

The Physics of Electron Beam Therapy

I Electron interactions with matter

When electrons traverse a medium, they undergo many interactions. Typically, an electron having an energy of 10 MeV will interact about 100 000 times. The electron, surrounded by its electric field, will interact by the Coulomb force with orbital electrons or with the nucleus. The electron can interact elastically resulting only in a change of its direction or inelastically transferring part of its energy to the surrounding medium through different energy loss mechanisms, which will be discussed in the next section. Therefore, in most of these interactions, the electrons will transfer none or only a small part of their kinetic energy. The changes in directions are treated using scattering theories and the energy loss is treated using stopping powers. These two concepts will be discussed later in this chapter. It is important to understand the process by which electrons lose their energy, since a basic quantity, the dose, is determined by the energy deposited per unit mass, as explained in Chapter 1.

It is common to characterise the type of interaction by the magnitude of the classical impact parameter *b* relative to the classical atomic radius *a* as shown in Figure 2- 1.

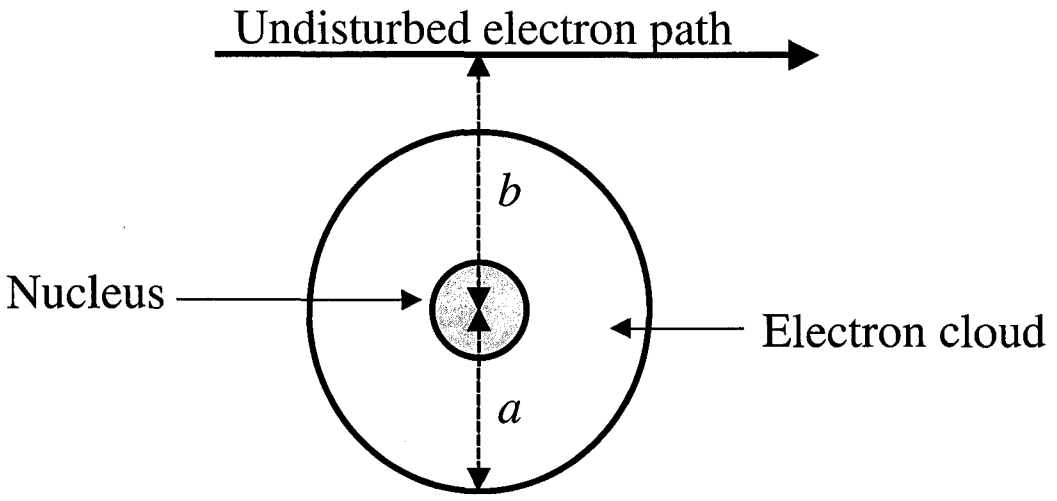

Figure 2- 1. Representation of an electron traversing the field of an atom where *a* denotes the classical atomic radius and *b* is the classical impact parameter.

The different types of interactions will be explained in the next section by referring to Figure 2- 1.

I.A Energy loss mechanisms

There are mainly three ways in which electrons lose their energy. In soft collisions, the electron interacts with the atom as a whole. In hard collisions, the electron interacts with an orbital electron. The energy loss by soft and hard collisions is commonly referred to as collisional loss. The electron can also interact with the Coulomb field of the nucleus in what is called radiative loss. For positrons, annihilation is another energy loss mechanism. Annihilation essentially consists of a positron that annihilates with an electron in-flight or at rest, which results in the production of two photons. The first three processes will be discussed in greater detail.

I.A.1 Collisional losses

Collisional losses can result in excitation or ionisation of the atoms in the medium. In a soft collision, which is considered a collision with the whole atom, the impact parameter b is much larger than the atomic radius a and only a small part of the incident electron energy is transferred to the medium to produce either excitation of the atom or ejection of an electron with low kinetic energy. The majority of electron interactions are soft collisions and about half of the energy loss is the result of these.

In hard collisions, the impact parameter b is on the order of magnitude of the radius a. This is considered an electron-electron collision and results in the ejection of an orbital electron with high kinetic energy. In the Møller theory that derives cross sections for this process, the orbital electron is assumed to be free. When the energy transferred is large, the ejected electron is called a delta-ray and it has sufficient energy to produce its own track (sometimes called a spur), that also results in a series of ionisations and excitations. The number of hard collisions is very low compared to the number of soft collisions. In the slowing down of an electron, hard collisions represent roughly half of the energy loss.

I.A.2 Radiative losses

If the impact parameter b is much smaller than the atomic radius a, the electron interacts with the Coulomb field of the nucleus. These interactions are mostly elastic, but in a small fraction of these interactions, about 2%, energy loss occurs through the emission of radiation. The Coulomb force results in a change in direction and a slowing down of the incident electron. From classical electromagnetism, charged particles emit radiation as they are accelerated or decelerated following the Larmor relationship:

$$\frac{dE}{dt} = -\frac{e^2 a^2}{6\pi\varepsilon_0 c^3} \quad . \tag{2.1}$$

From Coulomb's law the acceleration is proportional to the ratio of the atomic number of the medium and the mass of the incident charged particle. Therefore, the energy

loss by this process is only significant in the case of light charged particles such as electrons and positrons. It is also insignificant in low Z media for energies below 10 MeV. The resulting radiation is commonly called bremsstrahlung, the German word for "braking radiation". The energy of the bremsstrahlung photon can be between zero and the kinetic energy of the incident electron; however, a larger proportion of low energy photons is emitted. The angular distribution of these photons is dependent on the incident electron energy. If the electron's kinetic energy is low, like in conventional x-ray tubes, the photons are distributed perpendicular to the direction of the incident electron. On the other hand, if the kinetic energy of the electron is large, as in the production of radiotherapy photon beam from the target of a linear accelerator, the bremsstrahlung photons are forwardly directed.

The energy loss per atom by radiative collisions is proportional to Z^2. The energy loss if stated in terms of the number of electrons is proportional to Z. In very rare cases, the emission of a bremsstrahlung photon from a radiative collision between the incident electron and an orbital electron can occur. In this case, the energy loss per atom is proportional to Z.

The bremsstrahlung production is the process by which clinical photon beams are created from electron accelerators. In a clinical electron beam, the bremsstrahlung production is responsible for the energy deposited at greater depths.

I.B Stopping power

The average rate of energy loss of an electron in a medium is called the linear stopping power $\frac{dE}{dx}$ which represents an energy loss dE in a path length dx and is usually denoted by S and given in units of MeV/cm. In practice, it is common to use the mass stopping power S/ρ in units of MeVcm^2/g, which removes the density dependence except for a small contribution due to the density-effect which will be discussed later.

The mass stopping power is usually separated in two major quantities: the mass collisional stopping power $\left(S/\rho\right)_{coll}$ and the mass radiative stopping power $\left(S/\rho\right)_{rad}$. It is useful to separate these two different contributions to the energy loss since collisional losses happen close to the electron tracks while the energy loss due to radiative processes may be carried far away by bremsstrahlung photons. Also, these two contributions of the total stopping power have different dependencies on the characteristics of the incident charged particle and on the medium. The total mass stopping power can therefore be expressed as:

$$\left(S/\rho\right)_{total} = \left(S/\rho\right)_{coll} + \left(S/\rho\right)_{rad}. \tag{2.2}$$

The dependencies of the radiative and collisional stopping powers on energy of the incident particle and atomic number of the medium are quite different, as shown in Figure 2-2.

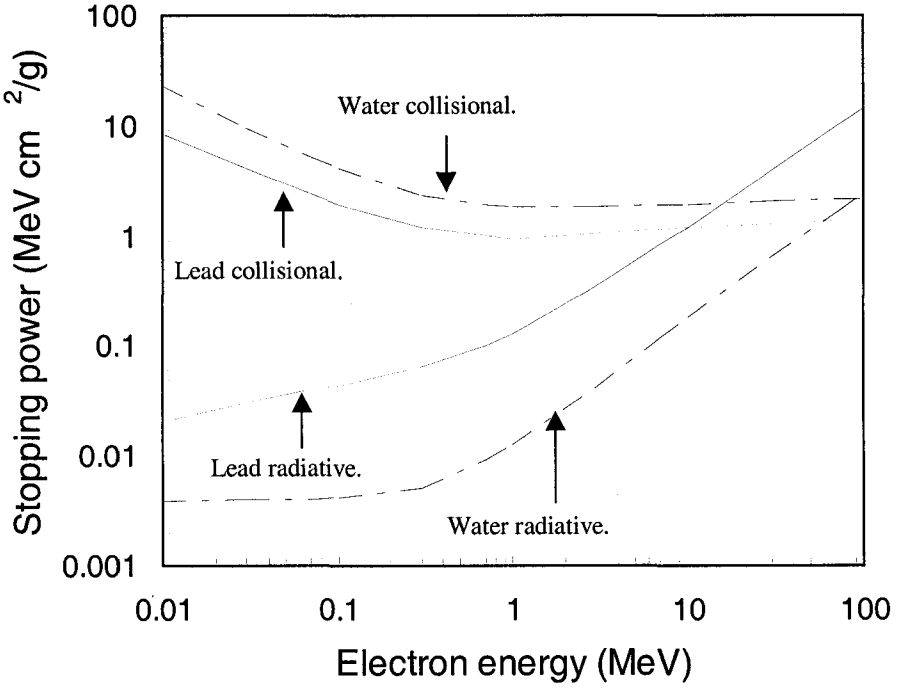

Figure 2- 2. Plot of the radiative and collisional stopping powers for lead and water.

The stopping powers for mixtures are obtained using Bragg's additive rule[1]. It states that since atoms contribute independently to the stopping power, their effect is additive. Thus, the mass stopping power for a mixture is:

$$\left(\frac{S}{\rho}\right)_{mix} = f_{Z_1}\left(\frac{S}{\rho}\right)_{Z_1} + f_{Z_2}\left(\frac{S}{\rho}\right)_{Z_2} + \ldots f_{Z_n}\left(\frac{S}{\rho}\right)_{Z_n}, \tag{2.3}$$

where f_{Z_1} to f_{Z_n} are the fractional weights of elements with atomic numbers Z_1 to Z_n respectively.

I.B.1 Collisional stopping power

A general expression for the mass collisional stopping power as given by Berger and Seltzer[1] is:

$$\left(\frac{S}{\rho}\right)_{coll} = \frac{N_a Z}{A}\int \frac{d\sigma}{dW} W dW, \tag{2.4}$$

where N_a is Avogadro's number, Z the atomic number, A the mass number and $\frac{d\sigma}{dW}$ is the differential cross section (per atomic electron) for inelastic collisions resulting in an energy transfer W. The integral is commonly separated into an integration with W smaller than W_c and W larger than W_c, where W_c is an energy boundary distinguishing soft and hard collisions. Bethe[2] has derived the low energy component of the collisional stopping power:

$$\left(\frac{S}{\rho}\right)_{coll}(W < W_c) = \frac{2\pi r_e^2 m_o c^2 N_a}{\beta^2}\frac{Z}{A} z^2 \left[\ln\left(\frac{2m_o c^2 \beta^2 W_c}{\left(1-\beta^2\right) I^2} - \beta^2\right)\right], \tag{2.5}$$

where r_e is the classical electron radius, z is the charge of the incident particle, I is the mean excitation energy, m_o is the electron mass, β is the incident particle's velocity normalised to the speed of light. This equation is only valid if the Born approximation is satisfied, implying that

the velocity of the incident electron (positron) is much larger than the velocity of the orbital electrons. For the higher energy term $(W > W_c)$, the differential cross sections for the production of delta electrons is given by Møller[3] for electrons and by Bhabba[4] for positrons. The integration goes from W_c to W_m, where W_m is the maximum energy transfer:

$$\left(\frac{S}{\rho}\right)(W > W_c) = \frac{N_a Z}{A}\int_{W_c}^{W_m} \frac{d\sigma}{dW} W dW \tag{2.6}$$

By convention, the faster of the two electrons after a collision is taken as the incident electron, so the maximum energy transfer is equal to half the kinetic energy of the incident electron. However, if the incident particle is a positron, the maximum energy transfer is equal to its kinetic energy. The resulting mass collisional stopping power is[5]:

$$\left(\frac{S}{\rho}\right)_{coll} = \frac{2\pi r_e^2 m_o c^2}{\beta^2} N_a \frac{Z}{A}\left[\ln(T/I)^2 + \ln(1+\tau/2) + F^{\pm}(\tau) - \delta\right], \tag{2.7}$$

where τ is the kinetic energy of the incident particle in units of $m_o c^2$, T is the kinetic energy of the incident particle and δ the density-effect correction, which will be discussed later. The term $F^{\pm}(\tau)$ is:

$$F^{-}(\tau) = (1-\beta^2)\left[1 + \tau^2/8 - (2\tau+1)\ln 2\right], \tag{2.8}$$

for an electron and:

$$F^{+}(\tau) = 2\ln 2 - (\beta^2/12)\left[23 + 14/(\tau+2) + 10/(\tau+2)^2 + 4/(\tau+2)^3\right]. \tag{2.9}$$

for a positron.

The mean excitation energy I in Eq.(2.5) and Eq.(2.7) is usually derived from experiments and represents the average of all excitations and ionisations of all atoms in the

medium. As an approximation, $I = CZ$ where C is a constant equal to about 11.5 eV. An extensive study of mean excitation energies is presented in the ICRU Report 37[1].

The density-effect correction in Eq.(2.7) is due to the polarisation of the medium that results from the passage of the charged particle and, as a consequence, reduces the stopping power. The electric field that the electron feels due to distant atoms is weakened by the presence of closer atoms. This effect is only important in dense material, not in gases and its importance increases with energy. An extensive review on this subject is presented in the ICRU Report 37.

The dependence of the collisional stopping power on energy for electrons, as expected by Eq.(2.7), is a result of the initial decrease with energy due to the β^{-2} in front of the bracketed term and a slow increase with energy due to the overall effect of the β terms inside the bracket. The collisional stopping power decreases with Z as can be seen from Eq.(2.7). The Z/A term in front of the bracket decreases as Z increases and the mean excitation energy I increases as Z increases.

I.B.2 Radiative stopping power

The rate of production of bremsstrahlung photons by charged particles is called the radiative stopping power. As mentioned previously, bremsstrahlung production is only important for light charged particles such as electrons and positrons. The expression for the mass radiative stopping power is:

$$\left(\frac{S}{\rho}\right)_{rad} = \sigma_0 \frac{N_a Z^2}{A}\left(T + m_0c^2\right)\overline{B_r}, \tag{2.10}$$

where $\sigma_0 = \frac{1}{137}\left(\frac{e^2}{m_0c^2}\right)$, $\overline{B_r}$ is a function of energy with values between 16/3 for $T \ll 0.5$ MeV and 15 for T=100 MeV[6].

The radiation yied $Y(T_0)$ of a charged particle of kinetic energy T_0 represents the fraction of energy loss that occurs through radiative processes and is given by:

$$Y(T_0) = \int_0^{T_0} \frac{\left(S/\rho\right)_{rad}}{\left(S/\rho\right)_{total}} dT \,. \tag{2.11}$$

Note that this yield does not exactly correspond to the energy lost to bremsstrahlung in a realistic slowing down of an electron since delta ray production is ignored (this is the continuous slowing down approximation (CSDA) and will be discussed in Section I.D).

The ratio of the radiative stopping power to collisional stopping power can be expressed as:

$$\frac{\left(S/\rho\right)_{rad}}{\left(S/\rho\right)_{coll}} = \frac{ZT}{n}, \tag{2.12}$$

where n is a constant usually between 700 and 800 MeV[6]. As can be seen in Figure 2- 2, the radiative stopping power increases with Z as predicted by Eq.(2.10). In addition, it can be seen that the radiative stopping power increases with energy as expected by the proportionality to T and $\overline{B_r}$ in Eq.(2.10).

I.B.3 Restricted stopping power

As mentioned earlier, an electron slows down mainly through many small energy transfers and this gives rise to the approximation that the electron loses its energy continuously, which is referred to as the continuous slowing down approximation (CSDA). Apart from the excitations and ionisations that take place near the track of the incident particle, some electrons (delta-rays) may be ejected with sufficient energy to create their own tracks, thus depositing their energy further away from the initial track.

The concept of restricted stopping power is to distinguish between the energy deposited locally and the energy deposited further away by delta-rays. This concept is very useful in radiobiology and microdosimetry and is referred to as linear energy transfer (LET) and represents the energy deposited along a particle's track. This can be characterised as a linear restricted stopping power L_Δ with the cut-off energy Δ. For example, $L_{100\,\mathrm{eV}}$ represents the energy losses with energy transfer less than or equal to 100 eV. When the cut-off value is equal to the maximum energy transfer ($T/2$ for electrons and T for positrons), the restricted stopping power becomes equal to the unrestricted stopping power. In the context of radiation dosimetry, it will be seen later that the dose deposited inside a cavity is proportional to the ratio of the stopping power of the cavity material to the stopping power of the medium in which the cavity is located. Some delta-rays may deposit their energy far away from the cavity, so using the unrestricted stopping power will overestimate the dose to the cavity. It is therefore useful to use the restricted stopping power to differentiate between the energy deposited inside and far away from the cavity. In this context, the cut-off value would represent the energy needed by an electron to cross the cavity. The expression for the mass restricted stopping power for electrons and positrons is obtained from the substitution of W_m by Δ in Eq.(2.6):

$$\left(\frac{L}{\rho}\right)_\Delta = \frac{2\pi r_e^2 m_0 c^2}{\beta^2}\frac{N_a Z}{A}\left[\ln\left(T/I\right)^2 + \ln\left(1+\tau/2\right) + G^{\pm}\left(\tau,\eta\right) - \delta\right]. \tag{2.13}$$

For electrons,

$$\begin{aligned} G^{-}\left(\tau,\eta\right) &= 1-\beta^2 + \ln\left[4\left(1-\eta\right)\eta\right] + \left(1-\eta\right)^{-1} + \\ &\left(1-\beta^2\right)\left[\frac{\eta^2\tau^2}{2} + \left(2\tau+1\right)\ln\left(1-\eta\right)\right] \end{aligned} \tag{2.14}$$

and for positrons,

$$G^{+}\left(\tau,\eta\right) = \ln 4\eta - \beta^2\left[\begin{array}{l} 1+\left(2-\xi^2\right)\eta - \left(3+\xi^2\right)\left(\xi\tau/2\right)\eta^2 + \\ \left(1+\xi\tau\right)\left(\xi^2\tau^2/3\right)\eta^3 - \left(\xi^3\tau^3/4\right)\eta^4 \end{array}\right], \tag{2.15}$$

where $\eta = \Delta/T$, $\xi = (\tau+2)^{-1}$ and the other symbols have been defined previously.

I.C Scattering processes

For many years, physicists only considered the energy loss processes in the transport of electrons. This was sufficient to calculate the energy deposition in an infinite homogeneous medium, but with the advent of methods to calculate dose distributions in heterogeneous media, the scattering processes were also investigated. In general there are two approaches to analysing scattering; scattering may be viewed as a single scattering process or a multiple scattering process. Single scattering events result in large angular deflections and multiple scattering events result in smaller angular deflections. There are two major processes by which single scattering take place: nuclear Coulomb scattering and electron-electron scattering.

The probability of nuclear Coulomb scattering is high when the distance of closest approach is smaller than the atomic radius. The electron will be scattered and when this is accompanied by the emission of radiation, it is disregarded in most scattering theories. The probability for scattering through an angle θ into an element of solid angle $d\omega$ is:

$$P(\theta) = \frac{d\sigma}{d\omega} N x d\omega, \tag{2.16}$$

where N is the number of nuclei per unit volume, x the thickness of the scattering material and $\frac{d\sigma}{d\omega}$ is the differential scattering cross section.

The differential elastic scattering cross section is given by the Rutherford formula:

$$\frac{d\sigma}{d\omega} = \frac{\pi e^4 Z^2}{2m_0{}^2 v^4} \frac{\sin\theta d\theta}{\sin^4(\theta/2)}. \tag{2.17}$$

In the derivation of this expression, the finite size of the nucleus, the screening of the electrons and the electron spin were ignored. Despite this, the Rutherford formula gives good agreement with experimental results.

In the Møller theory[3] for electron-electron scattering (inelastic), the orbital electrons are treated as free. The differential cross section for this process has been given by:

$$\frac{d\sigma}{dx} = 2\pi r_e^2 \frac{(T+1)^2}{T^2(T+2)}\left[\frac{1}{x^2} - \frac{1}{x(1-x)}\frac{(2T+1)}{(T+1)^2} + \frac{1}{(1-x)^2} + \frac{T^2}{(T+1)^2}\right], \qquad (2.18)$$

where T is the sum of the kinetic energy of the two electrons in units of m_oc^2, x is the fraction of T representing the kinetic energy of the lowest energy electron in the pair. For positron-electron scattering, the differential cross section is given by Bhabba[4].

Multiple small angle scattering is used to describe the scattering process when electrons traverse a thick layer of material. The net angle after the many scattering events is the result of the accumulation of many single scattering events and the net result is small angle multiple scattering. In the context of Monte Carlo calculations, the most well known small angle multiple elastic scattering theories are the Fermi-Eyges, Goudsmit and Saunderson[7] and Moliere[8]. These theories are based on single elastic scattering (Rutherford and screened Rutherford) and they ignore the inelastic electron-electron scattering.

I.C.1 Scattering power

As mentioned previously, an electron undergoes many interactions before coming to rest. The net effect in terms of deviations due to the many collisions is toward small angles. The probability of scattering at a certain angle after an absorber of density ρ and thickness l is related to the mean square angle (MSA) $\overline{\theta^2}$ through the following equation derived by Rossi[9]:

$$\frac{\overline{\theta^2}}{\rho l} = 16\pi N_a \frac{Z^2}{M_a} r_e^2 \left(\frac{m_0c^2}{\beta pc}\right)^2 \log\left[196Z^{-1/3}\left(\frac{Z}{A_r}\right)^{1/6}\right], \qquad (2.19)$$

where p is the momentum ($m_0 v$) of the electron, M_a is the molar mass of substance a, A_r is the relative atomic mass number.

The mass angular scattering power is defined as:

$$\frac{T}{\rho} = \frac{1}{\rho}\frac{d\overline{\theta^2}}{dl}, \tag{2.20}$$

and is proportional to the ratio Z^2/T^2, as can be seen from Eq.(2.19). This observation is useful when choosing the proper material for the scattering foil, an important component inside the treatment head of a linear accelerator operating in electron mode, since its use is to spread the electron beam.

I.D Range and related quantities

The range R of a charged particle of initial kinetic energy T_0 is the expectation value of its pathlength before it comes to rest regardless of direction of movement. The projected range t is the farthest depth of penetration in the initial direction of the particle. Figure 2- 3 illustrates these two concepts.

In practice, the range is related to the rate of energy loss or the stopping power. It is an average value and the energy loss fluctuations known as energy straggling are ignored. The electrons are assumed to lose their energy linearly and continuously. This approximation is known as the continuous slowing down approximation (CSDA). The CSDA range R_{CSDA} (in g/cm^2) is an approximation of the true range and is given by:

$$R_{CSDA} = \int_0^{T_0} \left(\frac{S}{\rho}\right)^{-1} dT . \tag{2.21}$$

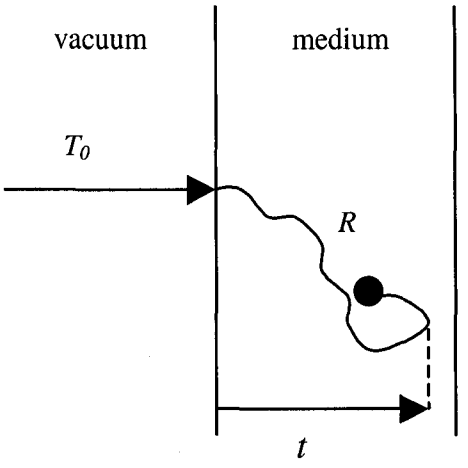

Figure 2- 3. Illustration of the concepts of range R and projected range t.

The CSDA range is the value that is tabulated in many references such as the ICRU Report 37. In practice, the practical range R_p is used and is obtained from an electron percent depth dose curve (see Section III.B).

II Cavity theory

In practice, the dose to a medium is determined from the dose measured by a dosimeter. Cavity theory thus relates the dose to the dosimeter to the dose in the medium.

II.A General considerations

It can be shown that if a medium is crossed by monoenergetic electrons of fluence Φ and of kinetic energy T, the dose can be determined by:

$$D = \Phi \left(\frac{S}{\rho} \right)_{coll} . \tag{2.22}$$

The particle fluence Φ is equal to the number of particles per unit area. In terms of dose deposition, the collisional stopping power is used and from now on, the subscript *coll* will be ignored. If the electrons have a distribution of energy, the dose can be expressed as:

$$D = \int \Phi_T (T) \frac{S(T)}{\rho} dT , \tag{2.23}$$

where $\Phi_T = \frac{d\Phi}{dT}$ is the electron fluence differential in energy. The average stopping power becomes:

$$\frac{\overline{S}}{\rho} = \frac{\int \Phi_T (T) \frac{S(T)}{\rho} dT}{\int \Phi_T (T) dT} = \frac{D}{\Phi} . \tag{2.24}$$

Then, for a spectrum of electrons,

$$D = \Phi \frac{\overline{S}}{\rho} . \tag{2.25}$$

II.B Bragg-Gray cavity theory

To illustrate the principles behind the Bragg-Gray theory, we consider a small cavity of medium *c* inside an otherwise uniform medium *m* as shown in Figure 2- 4.

Two conditions must be met in order for the Bragg-Gray theory to be applicable:

1- the size of the cavity must be small in comparison to the range of the charged particles crossing it.

2- the dose deposited in the cavity is assumed to be entirely due to charged particles crossing it.

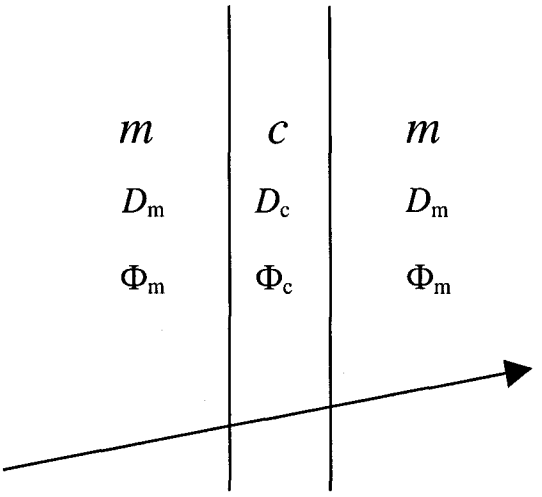

Figure 2- 4. Illustration of a small cavity *c* in a medium *m*.

If the first condition is satisfied, the electron fluences are identical in both mediums ($\Phi_c = \Phi_m = \Phi$). If the second condition is satisfied, the dose to the cavity *c* is:

$$D_c = \Phi\left(\frac{\overline{S}}{\rho}\right)_c, \tag{2.26}$$

and the dose to the medium *m* is:

$$D_m = \Phi\left(\frac{\overline{S}}{\rho}\right)_m. \tag{2.27}$$

From this,

$$D_m = D_c\left(\frac{\overline{S}}{\rho}\right)_c^m. \tag{2.28}$$

The Bragg-Gray theory does not take into account the production of delta-rays that have a range much larger than the cavity size and deposit part of their energy outside the cavity.

II.C Spencer-Attix cavity theory

The Spencer-Attix[10] cavity theory takes the production of delta-rays into account. An energy threshold Δ is defined and its value is usually taken as the energy of a charged particle to have a range equal to the average chord length of the cavity. A distinction is made between the creation of fast and slow secondary electrons. The slow electrons have energy below Δ and their energy is deposited locally. The fast electrons have energies between Δ and the maximum energy in the spectrum and are able to cross the cavity. According to the Spencer-Attix theory, energy deposition in the cavity is entirely due to electrons crossing the cavity. To calculate the dose to the cavity due to these electrons, the restricted stopping power for the cavity gas with energy transfers less than Δ is employed. Referring to Figure 2- 4, the dose to the medium is:

$$D_m = D_c \left(\frac{\bar{L}_\Delta}{\rho} \right)_c^m . \tag{2.29}$$

The mean restricted mass collisional stopping power ratio from Nahum's[11] formulation of Spencer-Attix theory is:

$$\left(\frac{\bar{L}_\Delta}{\rho} \right)_c^m = \frac{\int_\Delta^{T_0} \Phi_T^{m,\delta}(T) \left(L_{\Delta,m}/\rho \right) dT + TE_m}{\int_\Delta^{T_0} \Phi_T^{m,\delta}(T) \left(L_{\Delta,c}/\rho \right) dT + TE_c} . \tag{2.30}$$

The terms TE_m and TE_c are the track-end terms that account for energy deposited at the end of the tracks by electrons that have initial energy between Δ and 2Δ. These electrons can have an energy deposition that brings them below Δ and their energy would then be deposited on the spot. The expressions for the track-end terms are:

$$TE_m = \Phi_T^{m,\delta}(\Delta) \frac{S_m(\Delta)}{\rho} \Delta , \tag{2.31}$$

and

$$TE_c = \Phi_T^{m,\delta}(\Delta)\frac{S_c(\Delta)}{\rho}\Delta. \tag{2.32}$$

The dose deposited in the cavity from track-ends typically amounts to 5 to 10% of the total dose.

The electron fluence inside the detector when placed in a medium is different in energy, angle and space than it would be in the medium without the detector since the detector is usually not of the same composition as the medium. The relationship between the dose in the medium to the dose in the cavity is usually treated as a correction to the Spencer-Attix equation as follows:

$$D_m = D_c\left(\frac{\bar{L}_\Delta}{\rho}\right)_c^m P(d,med), \tag{2.33}$$

where $P(d,med)$ is the fluence perturbation correction factor. The magnitude of the correction has been shown to depend on the atomic number and physical density of the detector's sensitive volume relative to the medium[12]. Also, the correction is known to be greater at lower energies and to increase with the size of the detector[12].

III Electron beam characteristics

III.A Energy specification

Electron beams are usually characterised by a nominal energy that represents the energy of the electrons before they enter the treatment head of the accelerator. At this point, the spectrum is very narrow and a monoenergetic beam usually adequately characterises the spectrum of electrons. After passing through the treatment head, the spectrum gets wider and can no longer be described by a single energy. The two most popular ways of characterising the spectrum at the phantom surface are the *most probable energy* and the *mean energy*. The most probable energy is slightly larger than the mean energy.

The *most probable energy* at the phantom surface $E_{p,0}$ can be related to the practical range R_p by the following formula:

$$E_{p,0} = C_1 + C_2 R_p + C_3 R_p^2 . \tag{2.34}$$

The NACP[13] and the ICRU[14] found that the values C_1 = 0.22 MeV, C_2 = 1.98 MeV/cm and C_3 = 0.0025 MeV/cm^2 are accurate to within 2% for energies between 1 and 50 MeV.

The *mean energy* at phantom surface $\overline{E}_0$ can be related to R_{50} using the following relationship:

$$\overline{E}_0 = C_4 R_{50} . \tag{2.35}$$

The parameter R_{50} will be discussed in the next section. The AAPM[15] and the NACP[13] protocols recommend the value of C_4 equal to 2.33. However, it has been shown by Monte Carlo calculations[16] that the constant C_4 does depend on energy and if a constant value were to be chosen, it would be closer to 2.4 than to 2.33.

Of obvious importance is the knowledge of the energy variation with depth. The Harder relationship[15] gives an analytical expression for the *most probable energy* at depth:

$$E_{p,z} = E_{p,0}\left(1 - \frac{z}{R_p}\right). \tag{2.36}$$

The *mean energy* at depth can be approximated using the same relationship:

$$\overline{E}_z = \overline{E}_0\left(1-\frac{z}{R_p}\right). \tag{2.37}$$

III.B Percent depth dose curve

A typical electron beam percent depth dose curve is shown in Figure 2- 5 with its relevant parameters. The percent depth dose represents the dose at points on the central axis normalised to the maximum dose on the central axis. There is an initial dose build-up, followed by a rapid dose fall-off and a long tail. These characteristics make electron beam therapy suitable for treating lesions near the surface of the skin. Also, it offers greater dose uniformity to the target than orthovoltage x-rays.

For electron beams, the build-up is not due to the increasing fluence of electrons as in photon beams, instead it is due to the scattering properties of the beam in the medium. As the beam penetrates the phantom, the scattering angle increases with depth and the contribution on the central axis increases until a maximum is reached. The depth of maximum dose d_{max} increases with the nominal energy of an electron beam until a maximum value is reached, usually at about 12 to 15 MeV. The variation of d_{max} with the nominal energy can be explained by looking at the variation of the fluence and the stopping power with depth. The variation of d_{max} with energy is highly dependent on the type of collimation device.

Uncontaminated photon beams have a small electron fluence at the surface which increases with depth until a maximum is reached. Therefore, the surface dose is larger in the case of an electron beam. The surface dose increases with the nominal energy of an electron beam.

The parameter R_{50} represents the depth at which the dose falls to 50% of the maximum dose. This parameter is very useful since it is easy to measure and can be related to the mean electron energy at the surface of the phantom, as in Eq.(2.35).

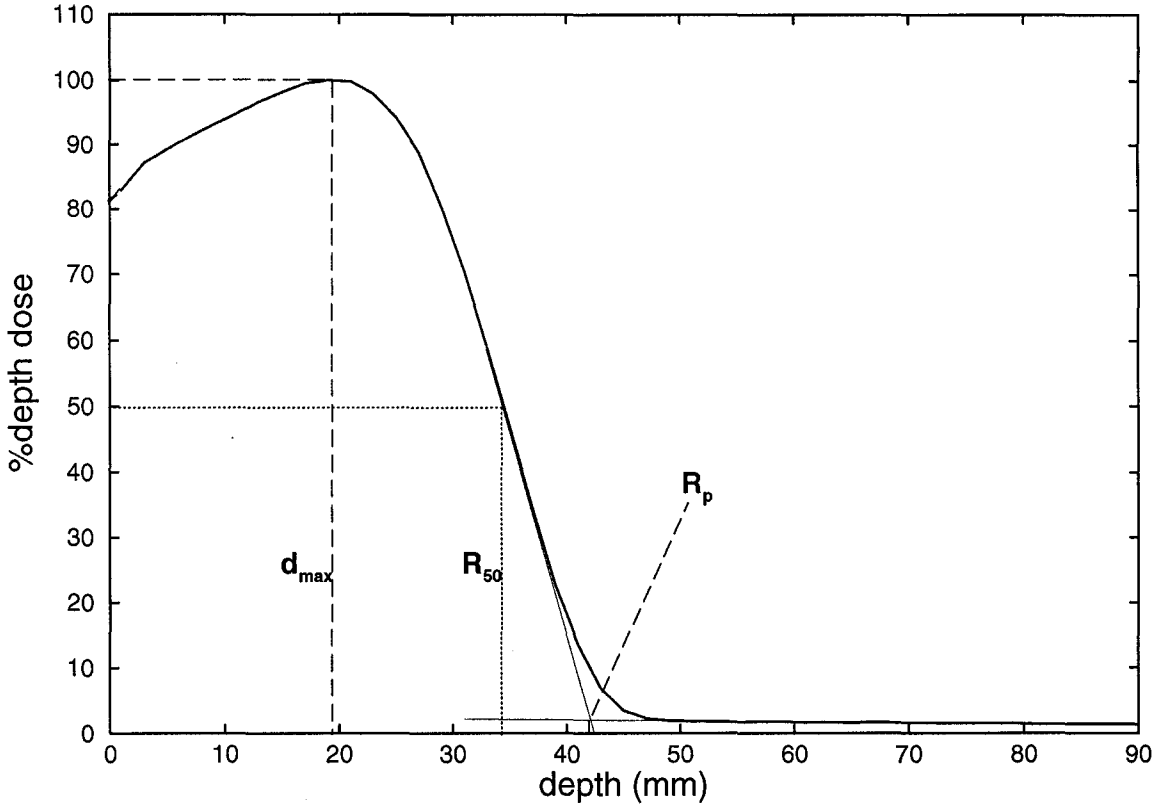

Figure 2- 5. A typical percent depth dose curve in water for a 9 MeV electron beam with a 10 x10 cm^2 applicator and an SSD of 100 cm with some important parameters.

The parameter R_p is the practical range. It is found at the depth at which tangent to the inflection point of the fall-off portion of the percent depth dose curve intersects with the tangent to the bremsstrahlung tail as seen in Figure 2- 5. The variation of R_p as a function of energy can be obtained by inverting Eq.(2.34).

The long tail in Figure 2- 5 is due to the production of bremsstrahlung photons. These photons are produced in the treatment head, in air, and in the phantom and, as explained in Section I.A.2, are responsible for dose deposition at large depths. The importance of the bremsstrahlung tail increases with energy since the radiative losses are more important at high energies, as explained in Section I.A.2.

The variation of the percent depth dose with field size is only important for small field sizes. When the field size becomes larger than the average range of the electrons in the field, the effect of field size variations is less pronounced.

References:

[1]ICRU, "Stopping powers for electrons and positrons," ICRU Report 37, International Commission on Radiation Units and Measurements, Bethesda, Maryland (1984).

[2]H. Bethe and W. Heitler, "On the stopping of fast particles and on the creation of positive electrons," Proc. Roy. Soc. A. **146**, 83-112 (1934).

[3]C. Moller, "Zur Theories des Durchgangs schneller Elektronen durch Materie," Ann. Phys. **14**, 568-577 (1932).

[4]H.J. Bhabba, "The scattering of positrons by electrons with exchange on Dirac's theory of the positron," Proc. Roy. Soc. **A154**, 195-206 (1936).

[5]F. Rohlrich and B.C. Carlson, "Positron-electron differences in energy loss and multiple scattering," Phys. Rev. **93**, 38-44 (1953).

[6]Frank H. Attix, *Introduction to radiological physics and radiation dosimetry* (Wiley & Son, New York, 1986).

[7]S. Goudsmit and J. L. Saunderson, "Multiple Scattering of Electrons," Phys. Rev. **57**, 24-29 (1940).

[8]G. Z. Molière, "Theorie der Streuung schneller geladener Teilchen I: Einzelstreuung am abgeschirmten Coulomb-Feld," Z. Naturforsch **2a**, 133-145 (1947).

[9]B. Rossi, *High Energy Particles* (Prentice-Hall, Englewood Cliffs NJ, 1952).

[10]L.V. Spencer and F.H. Attix, "A theory of cavity ionization," Radiat. Res. **3**, 239-254 (1955).

[11]A. E. Nahum, "Water/Air Mass Stopping Power Ratios for Megavoltage Photon and Electron Beams," Phys. Med. Biol. **23**, 24-38 (1978).

[12]P. N. Mobit, G. A. Sandison, and A. E. Nahum, "Electron fluence perturbation correction factors for solid state detectors irradiated in megavoltage electron beams," Phys. Med. Biol. **45** (2), 255-265 (2000).

[13]Supplement to the recommendations by the Nordic Association of Clinical Physics NACP, "Electron Beams with Mean Energies at the phantom surface below 15 MeV," Acta Radiol. Oncol. Rad. Phys. **20**, 402-415 (1981).

[14]ICRU, "Radiation dosimetry : electron beams with energies between 1 and 50 MeV," ICRU Report 35, International Commission on Radiation Units and Measurements, Bethesda, Maryland (1984).

[15]American Association of Physicists In Medicine AAPM TG-21, RTC Task Group, "A Protocol for the Determination of Absorbed Dose from High-Energy Photon and Electron Beams," Med. Phys. **10**, 741-771 (1983).

[16]D.W.O. Rogers, I. Kawrakow, and B. Walters, "Revised relationship between R_{50} and E_0 for electron beams," Conf. Proc. of the IEEE 2000 (2000).

Chapter 3

Monte Carlo Techniques

I Introduction

Monte Carlo techniques are used to provide solutions to a wide variety of mathematical problems that depend on probability and in cases where it is not possible to get a solution from experiment or from a simple formula. One of the first uses of a form of Monte Carlo goes back to 1777 with the Buffon's needle[1]. Comte de Buffon found a way to calculate the number π using a "hit or miss Monte Carlo" which is the least accurate Monte Carlo method. The procedure consists of tossing a needle in a random fashion onto a sheet of paper where a series of parallel lines separated by twice the length of the needle have been drawn. Based on mathematical principles, the number of times the needle will land on the lines should converge to $1/\pi$.

The term Monte Carlo was first used during the Second World War when two mathematicians, John von Neumann and Stanislas Ulam, suggested a method to study neutron diffusion[2]. Goldberger was the first one to actually use the method to study nuclear

disintegrations produced by high-energy particles and published a paper on this subject in 1948[3]. The popularity of the Monte Carlo method was later extended to many problems involving interactions of different particles. For example, Wilson published a historical paper on shower production in 1952 in the Physical Review[4]. To select the type of interaction, he constructed a motorised cylinder that acted like a wheel of chance. Around the cylinder, he wrapped a sheet of paper with a graph representing interaction probabilities and used the detection of cosmic rays to indicate when the motor should stop. The first use of an electronic digital computer to study shower production was reported by Butcher and Messel[5] and independently by Varfolomeev and Svetlolobov[6].

In the context of particle interactions, the probability of interactions between the particles can be obtained using the cross sections of the different processes. The probability of interactions for the different processes are sampled using a computer based pseudo-random number generator. In fact, the success of Monte Carlo calculations resides mostly in a procedure that can give a long sequence of independent random numbers. A truly random number sequence is impractical and would be based on natural random processes. One important quality of a random number generator is its length of periodicity that must be long in order to avoid repetitions.

A detailed knowledge of the transport of radiation is very important in fields such as radiation dosimetry, radiotherapy and radiation protection. In these contexts, the Monte Carlo techniques can help calculate various useful quantities such as dose, fluence, detector-related quantities, shielding requirements, etc... Monte Carlo techniques can also help answer questions which cannot be answered experimentally such as the fraction of primary and scattered dose, and the electron or photon contamination from interactions in a specific region.

A typical Monte Carlo code has four components: (1) the cross section data, (2) the transport algorithm, (3) the geometry specification and (4) the tools to analyse the data. Since the physics of the interactions and transport of ionising radiation is relatively well understood, Monte Carlo code packages have been developed. In these packages, the cross section data and the transport algorithm are provided. The geometry and the method for data analysis are

chosen by the user. In a Monte Carlo simulation, particles are "born" according to a source distribution. The source can be defined as a spectrum, a monoenergetic source, a beam model or using the information following an accelerator simulation. The distance for particle interaction is then determined by sampling probability distributions based on the total cross sections. The type of interactions of the incident particle and its progeny is determined by the relative individual total cross sections and their energy and direction are then sampled from the individual differential cross sections. History starts when the particle is "born" until both the particle and its progeny are absorbed or leave the volume of interest. By simulating a large number of histories, we can calculate quantities of interest with low uncertainty.

I.A Photon transport

In the case of photon interactions, the cross section of the different processes are small enough so that all interactions can be simulated. Here is an example of how part of the photon transport is done considering only pair production and Compton scattering for simplicity.

The mean free path is:

$$\lambda = \frac{M}{N_a \rho \sigma_{total}}, \tag{3- 1}$$

where M is the molecular weight, N_a is Avogadro's number, ρ the physical density and σ_{total} the total cross section per molecule. The variable:

$$x = -\lambda \ln(1 - R_1), \tag{3- 2}$$

is distributed exponentially between zero and infinity with a mean of λ and R_1 is a random number uniformly distributed between zero and one. The photon will then travel x/λ mean free paths before interacting. If the distance d to a boundary is smaller than x, d/λ must be evaluated and the number of mean free paths in the new region becomes $(x-d)/\lambda$. To find the distance x in the new region, λ must be evaluated for the new medium. To determine the

interaction, another random number R_2 must be selected. If $R_2 \leq \frac{\sigma_{Compton}}{\sigma_{total}}$, it is a Compton interaction, otherwise it is a pair production interaction. The state of the particles after the interactions will then be sampled using proper theories.

I.B Electron transport

It is possible for neutrons and photons to simulate each of their interactions due to the low number of interactions compared to the number of electron interactions. For electrons, due to many elastic scattering events with the nuclei, this is not possible and the condensed history technique proposed by Berger[7] is used instead.

In the condensed history technique, the path of the electrons are divided into straight macroscopic steps which group together many electron interactions. The overall scattering due to the many soft collisions that electrons undergo during the course of a step is applied at the end of the step by sampling a scattering angle from a multiple scattering distribution. The electrons are followed in each step using multiple scattering theory and a continuous slowing down approximation. The choice of step size depends on many factors including geometric constraints, probability of discrete interactions, the maximum allowed distance and maximum allowed energy loss imposed by the user, as well as various limits set by the multiple scattering formalism. The size of the step is selected as the most restrictive of the above factors. Since the electrons do not travel in straight lines, corrections are required to permit correct calculation of the energy deposition. The path length correction (PLC) corrects for the curvature of the electron path. A correction is also required for the lateral displacement ρ of the electron during its step. These two effects are shown in Figure 3- 1.

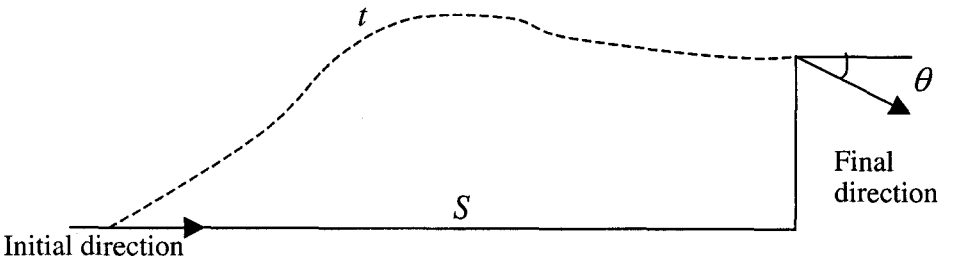

Figure 3- 1. Representation of a typical electron step.

In Figure 3- 1, S is the straight path, t is the curved path and θ is the angle between the initial and final direction of the electron. The PLC is given by:

$$PLC = \frac{t - S}{S}, \tag{3.1}$$

where S is obtained from t using a relation from Berger[7]:

$$S = \frac{t}{2}\left[1 + \cos\theta(t)\right]. \tag{3.2}$$

The lateral displacement ρ from Berger[7] is obtain by:

$$\rho = \frac{t}{2}\sin\theta(t). \tag{3.3}$$

The two previous corrections are insignificant for very high electron energies and very small step sizes. A transport algorithm must include corrections for both path length curvature and lateral displacement to avoid the need of using extremely small steps, which would result in very long calculation times.

There are two groups of condensed history algorithms, class I and class II. In a class I algorithm, many collisions are grouped together in steps of pre-selected lengths. The energy and direction of the primary electrons are calculated at the end of the step from a multiple scattering distribution. In the EGS4 (see Section II.A.2) class II algorithm, the small energy

losses are treated the same as in a class I algorithm, however the large energy losses are treated differently. The creation of bremsstrahlung photons and delta electrons are treated as catastrophic events only if their energy is above a certain threshold. These catastrophic events are followed individually and the incident particle is affected by their production. In a class II algorithm, thresholds for production of secondary particles are defined as *AE* and *AP* for the energy above which delta electrons and bremsstrahlung photons are created respectively. In both classes of algorithms, energy cut-offs are specified which represent the energy below which the particle ceases to be followed and its energy is deposited locally. The energy cut-offs are usually defined as *PCUT* for photons and *ECUT* for electrons. The two most well known electron-photon Monte Carlo systems are the ETRAN (Electron TRANsport)[8] and the EGS (Electron-Gamma-Shower)[9] systems that use a class I and class II algorithm, respectively. These two systems give rise to many codes that are currently applied in the context of radiation transport for medical physics and particle physics.

I.C Statistics and efficiency

The different uncertainties on a scored quantity are usually divided in two groups. Uncertainties of type A are errors of statistical nature. The uncertainties of type B include errors of systematic nature, for example, errors on the cross section data, programming errors, and approximations in the transport algorithm. These uncertainties are not usually taken into account when specifying the uncertainty on a Monte Carlo calculation. The computing efficiency of a calculation is expressed as:

$$\varepsilon = \frac{1}{Ts^2}, \tag{3.4}$$

where T is the calculation time and s is the statistical uncertainty. The calculation time is determined by the desired accuracy and is governed, in practice, by the number of histories N

that will be simulated. The statistical uncertainty is inversely proportional to $\sqrt{N}$, so when N is doubled, the statistical uncertainty is divided by $\sqrt{2}$ which does not change the efficiency. In order to improve the efficiency, one can use, for example, symmetry considerations or variance reduction techniques. Thus, there is a trade-off between reducing the statistical uncertainty and the computing time. One example of using symmetry considerations is when one wants to transport particles coming from a square beam in a medium consisting of horizontal slabs. In this case, one could add up contributions in different quadrants before analysing the data in order to increase the efficiency. The variance reduction techniques consist of using some "tricks" to reduce the time to get a certain statistical uncertainty and these will be discussed in greater detail in Section II.A.2. There are two ways of doing the statistical analysis: either using batches or an "on the fly" technique. When using batches, a simulation of N histories is separated into n independent batches, each of them simulating N/n histories. The uncertainty on a calculation is obtained by combining the uncertainties of each batch, which includes the uncertainty from all histories in that batch. The most probable estimate μ of a scored quantity that is Poisson distributed and, for large n, normally distributed is:

$$\bar{x} = \frac{1}{n}\sum_{i=1}^{n} x_i \tag{3.5}$$

while the most probable estimate of the variance σ^2 is:

$$s_x^2 = \frac{1}{n-1}\sum_{i=1}^{n}\left(x_i - \bar{x}\right)^2 . \tag{3.6}$$

The result is stated as $\bar{x} \pm s_{x,eom}$ where $s_{x,eom}$ is the statistical error on the mean $s_{x,eom} = \sqrt{\frac{s_x^2}{n}}$.

To reduce the statistical uncertainty, the number of batches should be as large as possible, however, due to storage requirements, the number of batches is usually between 10 and 30. In order to reduce the calculation time, parallel processing can be employed to separate the work on different machines. If the number of machines is m, the number of histories per machine will be N/m .The mean becomes:

$$\bar{x} = \sum_{j=1}^{m} \left(\frac{N_j}{N} \right) \bar{x}_j , \tag{3.7}$$

where the subscript j denotes the j^{th} machine. The estimate of the variance will be:

$$s_{\bar{x}}^2 = \sum_{j=1}^{m} \left(\frac{N_j}{N} \right)^2 s_{\bar{x}_j}^2 . \tag{3.8}$$

An "on the fly" way of handling statistics is much different. By considering a particular scoring volume, it can be shown that the standard deviation on a calculated quantity x can be described as a function of $\sum_{i=1}^{n} x_i$ and $\sum_{i=1}^{n} x_i^2$ where n is the total number of times the quantity x was evaluated in that scoring region. This is a history by history method since each history contributing to the fluence or dose in the scoring region contributes to evaluating the statistics of that scoring region.

II The EGS Monte Carlo family

The first version of the EGS family, EGS1 and its companion code PEGS1 (Preprocessor for EGS1) was written in Fortran IV in the early 70's when Ford and Nelson made modifications to the code SHOWER4 which is a child of few codes that were developed in the 60's and early 70's. With the discovery of the J/ψ particle and the rising of hexagonal modular NaI detector, very promising high-energy gamma-ray spectroscopy was possible. However, EGS1 could not be used in complex geometry; it was a one-region, one-medium code. Many EGS1 users requested a new version that could allow more complex geometry. EGS1 became a sub-program with two user-callable sub-routines, HATCH and SHOWER, which require two user-written subroutines, HOWFAR and AUSGAB (these four subroutines

will be explained in more detail in Section II.A.2). EGS1 and PEGS1 were rewritten in MORTRAN2, which was translated by a Macro Processor into Fortran. These versions were completed in 1975 and called EGS2 and PEGS2. These new versions had complex logic in the electron transport routine. For this reason, as well as problems such as handling bremsstrahlung angular distributions and for greater universality, the code was modified and released in 1978 as EGS3/PEGS3[9]. With this code, showers could be followed from a few thousand GeV to 0.1 MeV for photons and 1.5 MeV (total energy) for electrons in any element ranging from Z=1 to Z=100.

II.A The EGS4/PEGS4 package

The EGS4/PEGS4[10] Monte Carlo package was developed at the Stanford Linear Accelerator Center (SLAC) by W.R. Nelson, H. Hirayama and D.W.O. Rogers. The major changes to the EGS3/PEGS3 package includes modifications to the transport of low energy electrons, incorporation of Rayleigh scattering and fluorescent photons as well as improved geometrical options. The low energy limits for photon transport passed from 0.1 MeV to 10 keV and from 1.5 MeV to 521 keV (total energy) for electron and positron transport.

II.A.1 PEGS4

One important part of a Monte Carlo package is the cross section data. In the EGS4/PEGS4 package, the cross section data for any mixture can be created by PEGS4 to be used by EGS4. PEGS4 is the preparation code of EGS4 which prepares cross section data for material ranging from Z=1 to Z=100 with an energy range from a few keV to several thousand GeV. Unrestricted collisional stopping powers were obtained from Berger and Seltzer[11] and were adopted in the ICRU Report 37[12]. PEGS4 constructs a piecewise linear fit to the cross section data and branching ratio over a large number of energy intervals and prepares the data for use by EGS4. PEGS4 also contains a table for the mean excitation energies I for all elements from Berger and Seltzer. For a compound or mixture, PEGS4 determines the I values by doing a weighted average of the log of the I values of the different materials. For any

material, PEGS4 determines the density correction based on a formula from Sternheimer and Peierls[13], which depends on physical parameters, and on the *I* values. The bremsstrahlung cross sections are given by the standard Bethe-Heitler cross section[14] with a correction from data by Koch and Motz[15]. PEGS4 loads the cross sections for the photoelectric effect and pair production and calculates the total Compton cross section. PEGS4 is written in Mortran3 and needs only to be run once per material after which the data for that material can be used by EGS4 for as many times as needed.

II.A.2 EGS4

The EGS4 Monte Carlo code is a well-benchmarked code that has been and is still in use in various types of research in physics and engineering. The algorithm can transport photons and charged particles in matter to allow the user to calculate a wide variety of useful quantities. The physical processes that are taken into account are:

- Bremsstrahlung production
- Positron annihilation in flight or at rest
- Molière multiple-scattering theory
- Møller (e^-e^-) and Bhabha (e^+e^-) scatterings
- Pair production
- Compton and Rayleigh scattering
- Photoelectric effect

A particle and its progeny will be followed step by step and all the previous physical processes taken into account.

As mentioned previously, it is not efficient for electrons to simulate all interactions and instead, a condensed history Class II technique is used. The electron is assumed to travel in

straight lines within many small steps with the application of corrections mentioned previously. First, the distance to a discrete interaction must be found in the same way as for photons although here we consider the total cross section due to bremsstrahlung production above an energy threshold *AP* and delta ray production above an energy threshold *AE*. The step size is selected as mentioned in Section I.B. The electron is then transported to the smallest distance between the step size and the distance of the next discrete interaction. At that point, the new direction of the electron is sampled from the Molière multiple scattering which takes into account the elastic scattering collisions with nuclei and low energy inelastic scattering. The energy loss during that step is the product of the straight distance (corrected by path length correction) and the total restricted stopping power with energy thresholds *AE* and *AP* evaluated at the beginning of the step. If no discrete interaction has occurred, a new step is taken and the procedure repeated. At the time of a discrete interaction, the type of interaction is selected between bremsstrahlung and delta ray production in the same way as it was explained when selecting between Compton and pair production previously. The energy of the incident particle and the new particle is sampled using Møller theory for delta ray production and using Bethe-Heitler theory for bremsstrahlung production.

Shortly after the release of EGS4, an improved method of electron transport was established, EGS4/PRESTA (Parameter Reduced Electron Step Transport Algorithm)[16]. The default step size algorithm was found to be inadequate for the transport of low energy electrons[17]. As mentioned previously, artefacts like the path length correction and lateral displacement can become important when the steps are large. For this reason, in the standard EGS4 version, it was suggested to use small steps since the correction for these artefacts, was not adequate. By doing this, the user is then faced with long calculation times. Thus, the PRESTA algorithm provides a way to find the optimum step size. EGS4 does not allow performing a step through a boundary, however, large steps can be selected when far from a boundary and small steps selected in the vicinity of a boundary in PRESTA. PRESTA includes an improved path length correction (PLC) so that no large artefacts appear when taking large steps. Since large steps are now possible, lateral displacement becomes important, so PRESTA also incorporates an improved lateral correlation algorithm (LCA) which performs a translation perpendicular to the direction of motion during the electron step.

As mentioned in the introduction of this chapter, variance reduction techniques are a way to improve the efficiency of a calculation. EGS4 incorporates the possibility of using some of these techniques for photon and charged particle transport. One example for photon transport is the variance reduction known as interaction forcing. This technique can be used when photon interactions are of interest by forcing them to happen since otherwise some photons may leave the geometry without interacting, resulting in a loss in efficiency. The probability of interactions will be modified to force an interaction inside the geometry of interest. After doing this, the scored quantities are multiplied by a weighting factor that accounts for the probability that the photon would have actually interacted in the region. One example for the case of electron transport is the range rejection technique. In this technique, the transport of an electron is stopped if it does not have enough energy to reach a boundary and in that case, its energy is deposited locally. By doing this, considerable calculation time can be saved but the possibility that the electron might have produced a bremsstrahlung photon that may have escaped the local region is ignored. The PRESTA algorithm mentioned previously might also be considered a variance reduction technique since it optimises the selection of the step size.

A diagram representing the structure and sub-routines of EGS4 is shown in Figure 3-2. The diagram is divided in a user-written section and a section with the sub-routines included with EGS4. The communication between these two sections is performed through the use of variables that are common to both sections. The MAIN routine makes calls to the subroutines HATCH and SHOWER. HATCH is the sub-routine that reads the media data from PEGS4.

SHOWER is called once per history and takes care of the actual particle transport by calling the proper sub-routines for photons, electrons or positrons. The sub-routine UPHI is called to establish the direction of the particles after an interaction. The user-written sub-routine HOWFAR defines the geometry of the problem by defining composition and density of all materials in all regions. The user-written sub-routine AUSGAB handles the scoring of quantities of interest. In default conditions, AUSGAB can be called for five different reasons, for example, when the energy of the particles falls below *ECUT* for an electron or *PCUT* for a photon or a particle is going to be discarded because it leaves a region of interest. Except the five default reasons, there are twenty conditions that can be "switched-on" by the user to cause

an AUSGAB call. For example, just before a Compton interaction occurs by setting IAUSFLAG (17) = 1, the user can have EGS4 call AUSGAB to count the number of Compton interactions. AUSGAB will keep track of why it was called by assigning to each reason a particular value to a parameter called IARG. AUSGAB is not by default called in all 25 situations because it would be too time consuming.

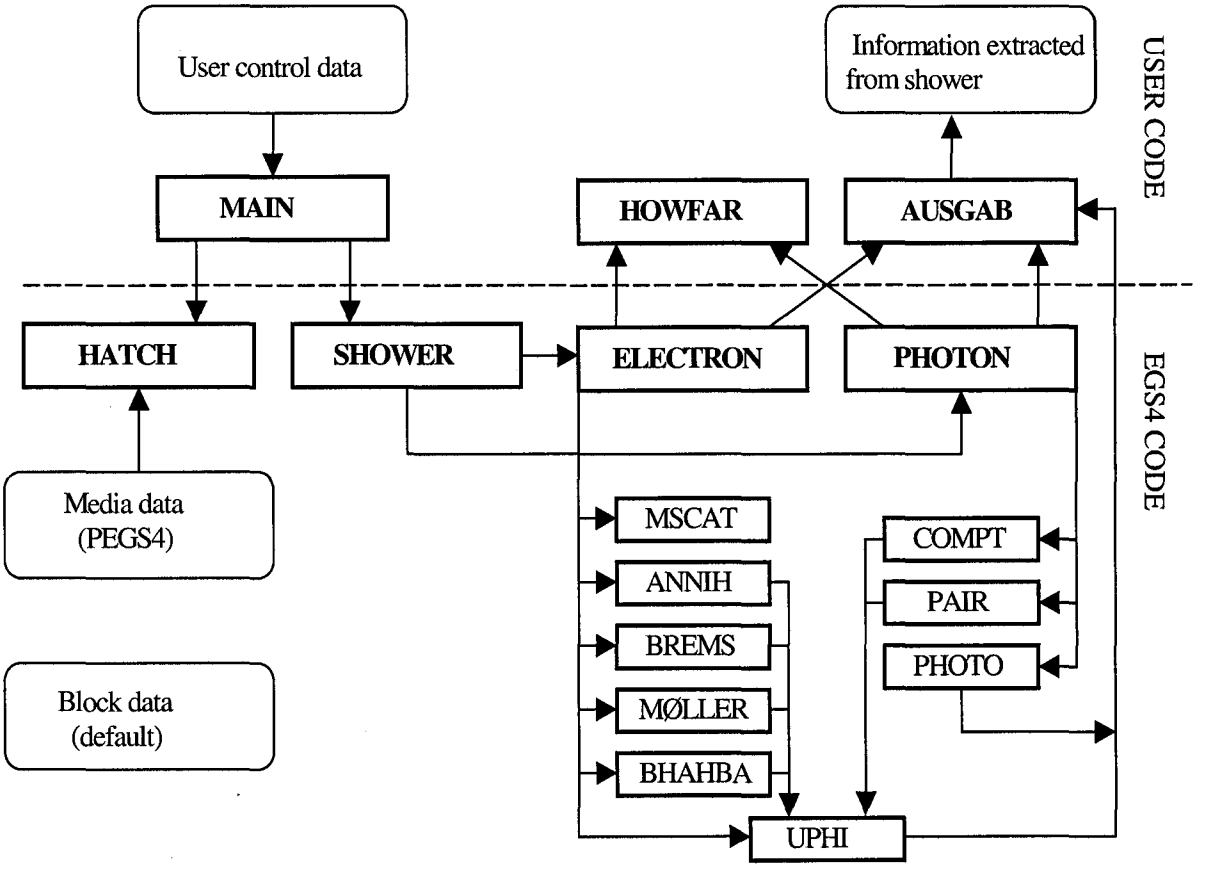

Figure 3- 2. Diagram representing the structure and sub-routines of EGS4.

II.B EGSnrc

EGSnrc[18] is a more recent version of EGS4. An improved electron transport algorithm has replaced the old PRESTA algorithm. Major improvements have been made in the calculation of energy losses, electron step size and boundary crossing. EGSnrc also uses PEGS4 to prepare the media data. This new version incorporates major physics changes. The

old multiple scattering theory has been replaced by a new theory which allows transfer to single scattering for short steps. In this new multiple scattering theory, relativistic spin effects are included in the cross section. Significant differences have been reported between percent depth dose calculations with and without this spin option "turned-on". Also, fluorescent photons from the K, L and M shells, Auger electrons and Coster-Kronig electrons can be created and followed. In addition, bremsstrahlung angular sampling has been improved as well as other physics-related changes, that are not mentioned here. EGSnrc also offers two different random number generators: RANMAR, which is also used in EGS4 and RANLUX which offers different luxury levels from 0 to 4 and a periodicity of 10^{165}.

II.B.1 EGSnrc user codes

The National Research Council of Canada (NRC) has for many years provided user codes that could be used with EGS4, the most popular being DOSRZ, SPRRZ and FLURZ. The user codes needed to be modified with the introduction of EGSnrc. The new user codes[19] that are part of the EGSnrc package are DOSRZnrc, SPRRZnrc, FLURZnrc and CAVRZnrc. These user codes all use similar input files. For example, specifications must be made concerning the geometry, the way the scoring is to be made, the cut-off and thresholds energies of secondary particle production, the number of histories and if special variance reduction techniques or physics options are to be used. These codes can use simple monoenergetic sources as input or more complex sources like a spectrum or a phase-space file. DOSRZnrc and DOSXYZnrc can score dose in right-cylindrical and cartesian geometries respectively. FLURZnrc is used to score a variety of fluence related parameters in a right-cylindrical geometry. CAVRZnrc calculates various ion chamber related quantities in a right-cylindrical geometry. SPRRZnrc calculates stopping power ratios in a right-cylindrical geometry.

II.C BEAM

The BEAM[20] code was created to meet the goal of the OMEGA project (Ottawa Madison Electron Gamma Algorithm) which was to develop a full 3-D electron beam treatment planning system based on Monte Carlo techniques. BEAM is based on the PRESTA extension of EGS4 and is used to model standard radiotherapy sources such as orthovoltage units, Cobalt-60 units and linear accelerators in photon and electron mode. BEAM runs on Unix (Linux) operating systems using about 2000 lines of script.

A radiotherapy unit is modelled using a series of component modules (CM) which are perpendicular to the z-axis and contained between two planes perpendicular to the z-axis. The z-axis is taken as the beam-axis. The CMs are independent and are not allowed to overlap. The CMs are geometrical objects that can be specified by providing dimensions, positions and material compositions by the user to reproduce the actual components inside the unit as close as possible.

There are 3 major outputs from a BEAM simulation, the listing file, the phase-space file and a graphic file. The listing file has different kinds of outputs. With a proper selection in the input file, a variety of fluence related parameters for each type of particles can be scored in different scoring planes in rectangular or circular regions. Dose and energy depositions can also be scored in selected regions. Finally, the phase-space file contains information about particles, namely their position on the plane, direction cosines, energy, charge, weight, LATCH and NPASS. The LATCH is used to "tag" a particle, for example, to find the last region a certain electron has interacted in. For example, it can provide the source of a particular bremsstrahlung photon. NPASS is a variable specifying the number of times a particle has crossed a particular plane. The memory requirement to store the information on a particle is 28 bytes but once created, the phase-space file can be used as input for further calculations. It can be used to restart the full unit simulation to increase the number of particles collected or used as input for a code that could simulate the radiation transport inside a phantom. A phase-space file can also be created below a certain CM in order to restart the simulation at this plane if simulations are needed where only the CMs below this plane are modified. The phase-space file can be analysed with BEAMDP which is part of the BEAM package to get a wide variety

of fluence related quantities. A plot of the particle fluence as a function of energy of photons and electrons for a 9.4 MeV phase-space file for the simulation of the Clinac 18 is shown in Figure 3- 3. The photon fluence is on the order of the electron fluence but of much lower energy.

The graphics output file is to be used by EGS_windows that displays the unit in 3-D and for which it is also possible to view a limited number of electron and photon tracks. For the work in this thesis, the Clinac 18 linear accelerator in the electron mode was used with a 10x10 cm^2 applicator and an SSD of 100 cm. Figure 3- 4 shows an EGS_windows image of the accelerator and some particle tracks. The radius of the electron monoenergetic pencil beam as it enters the treatment head as well as its energy must be selected by the user.

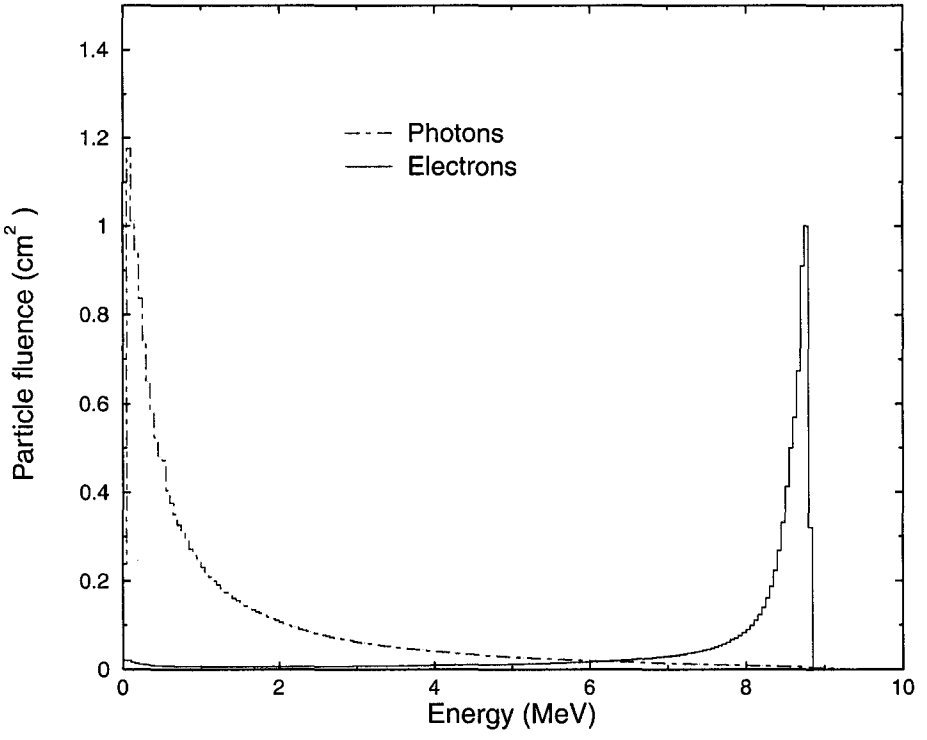

Figure 3- 3. Plot of the particle fluence of photons and electrons for a 9.4 MeV electron beam phase-space file from the simulation of the Clinac 18.

The energy of the electrons as they enter the simulated treatment head must be optimised in order to achieve the same beam characteristics for both the simulated and actual case. It is common to perform this comparison by looking at the measured and calculated R_{50}

in water. A phase-space file is created at a plane corresponding to the phantom surface and used as input to a Monte Carlo code that calculates dose in a phantom. This is done by "trial and error" by modifying the energy of the electron pencil beam in the simulation until an acceptable agreement is obtained between the two R_{50}s To verify that the geometry of the accelerator is properly modelled, measured and calculated beam profiles at different depths can be compared.

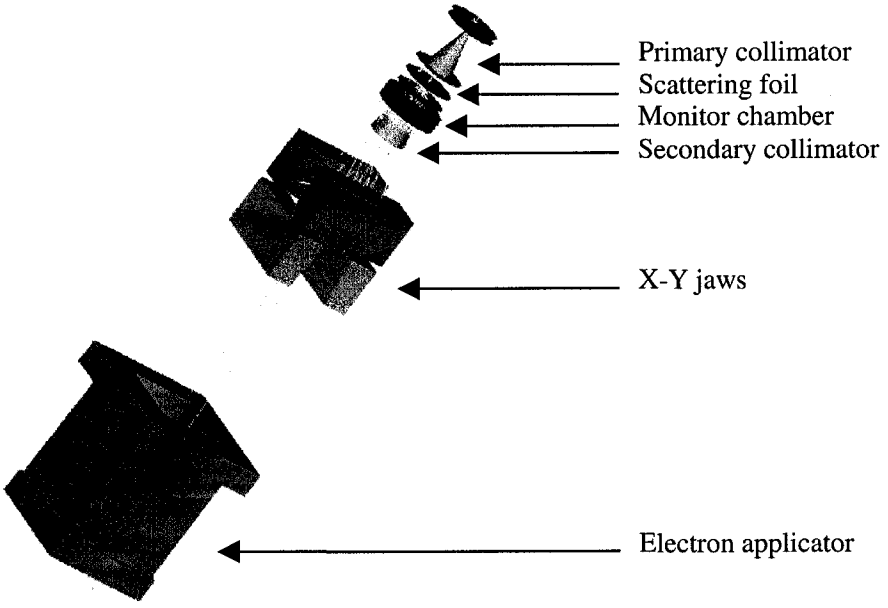

Figure 3- 4. A 3-D image of the Clinac 18 from EGS_windows.

III Voxel Monte Carlo system

EGS4 and EGSnrc were designed to simulate radiation transport for various energy, atomic number and mass density ranges that extended far beyond what is seen in current radiotherapy. The Voxel Monte Carlo (VMC)[21] system was created to simulate the transport of electrons and is applicable within an energy range of 1-30 MeV, low Z materials and physical density from 0 to 3 g/cm^3. VMC introduces many approximations to the transport

that make VMC faster than EGS4 by a factor of 30 to 40, thus it is commonly referred to as a type of *fast Monte Carlo* system. As EGS4 and EGSnrc, VMC uses a class II condensed history technique. VMC uses electrons that are either monoenergetic or from a spectrum, and either a phase-space file or beam model as input.

An important reason for the speed improvement is the reduction in the number of histories that are required to achieve a certain type A uncertainty. This is done by translating a history with starting point $\vec{x}_1$ to another starting point $\vec{x}_2$. By doing this, the sampling of probability of interactions, scattering angles and energy of secondary particles need only be done for the original history. The only condition in order to apply this approximation is that the points of the starting positions must be sufficiently separated so that the histories can't interfere. The number of history repetitions depends on the field size but it is common to use 5 repetitions per cm^2. It has been shown that this value is conservative[21]. Another reason for the improvement in speed is the reduction of the average number of electron steps per history. This is done by assuring that an electron travels a maximum fraction of its energy per step and even increasing this limit when the energy of the electron is low.

The bremsstrahlung production in VMC is treated in a very different way compared to EGSnrc. In VMC, the production of bremsstrahlung photons serves only as energy fluctuations for the electrons; the photons are not followed. With the energy and atomic number ranges in radiation therapy, the bremsstrahlung contribution to the dose is small. The photon background is extracted from a measured dose distribution in water and added to the calculation.

The Møller and bremsstrahlung cross sections are approximated. The collisional and radiative stopping powers are taken from ICRU Report 37. The energy losses for continuous processes (below an energy threshold) are obtained by subtracting the energy losses due to discrete interactions (above an energy threshold) from the ICRU Report 37 stopping powers. These discrete energy losses depend on the Møller and bremsstrahlung cross sections that are approximated resulting in an approximated energy loss due to continuous processes.

In the first version of VMC, the multiple scattering theory approximated by a Gaussian distribution underestimated the elastic scattering at large angles. The lateral displacements were

neglected and the path length correction was modelled simplistically using Fermi-Eyges theory. To overcome this, Kawrakow[22] worked out a new multiple scattering theory and a longitudinal and lateral correlation algorithm (LLCA).

The first step in the VMC system is to generate a history in a water phantom. The incident electron is followed until it reaches its cut-off energy. If in a step of size s, the electron looses the energy ΔE and has crossed a boundary of length Δs in its path, the energy deposited in the boundary is:

$$\Delta E_1 = \Delta E \frac{s_1}{s}. \tag{3.9}$$

If no boundary was crossed, the total energy is deposited in the first voxel.

To do the transport in a heterogeneous phantom, scattering powers and stopping powers (collisional and radiative) have to be known. VMC takes advantage of relations between physical density and the ICRU Report 37 mass stopping powers. The ratio of mass collisional stopping power from all body tissues to mass stopping power of water was plotted as a function of the ratio of the density of the same material to the density of water and fitted as:

$$\frac{S_c(\rho,E)/\rho}{S_c^0(E)/\rho_0} = f_c\left(\frac{\rho}{\rho_0}\right) = \left(\frac{\rho}{\rho_0}\right)^{-0.17}. \tag{3.10}$$

Eq.(3.10) is valid for a mass density larger than 0.8 g/cm^3. For lower mass densities, only data for lung was available so that no fit could be made and the right-hand side of Eq.(3.10) is taken as 1.039, which is the value for lung. The energy has to be stored in an array to get the information for all energies. The same procedure is applied for the mass radiative stopping power.

$$\frac{S_r(\rho,E)/\rho}{S_r^0(E)/\rho_0} = f_r\left(\frac{\rho}{\rho_0}\right) = \begin{cases} 1.13+0.56\ln(\rho/\rho_0-0.3), & \rho \geq 0.9 \text{ g/cm}^3 \\ 1.049-0.228\rho/\rho_0, & \text{all other } \rho \end{cases}. \tag{3.11}$$

The ratios of mass scattering powers are simply equal to the ratio of mass densities. In practice, CT images are available and a relation is used between the Hounsfield number and mass density. The Hounsfield numbers are calculated as a function of density of the body tissues from the total linear attenuation coefficients of the different tissues from ICRU Report 46[23]. Of course the x-ray energy needs to be known. From this relation, the density is calculated from the Hounsfield number of a particular voxel. In VMC, the voxels are rectangular and only the density needs to be specified.

To apply a history generated in water to a heterogeneous phantom, the path length, continuous energy losses by collisional and radiative processes, number of secondary electrons and multiple scattering angles must be re-evaluated. The path length is scaled by the ratio of total mass stopping powers medium to water. The energy losses and the number of secondary electrons are also a function of the stopping powers. The multiple scattering angles are evaluated in the heterogeneous phantom without considering the history generated in water.

III.A XVMC

XVMC[24] is a *fast Monte Carlo* system for coupled photon and electron transport based on VMC. The electron transport is done as in VMC, except the Møller scattering is sampled from the exact Møller cross section rather than from an approximated form as in VMC. In VMC, the energy distribution of bremsstrahlung photons was approximated by a simple formula[21], here it is replaced by sampling from the Bethe-Heitler cross section. Also in VMC, the bremsstrahlung photons were created and then discarded, whereas this approximation has been removed for XVMC.

In the original XVMC version, only Compton scattering and pair production were simulated. A new version[25] now includes the photoelectric process. The inclusion of the latter process has an effect of less than 1% for energies of 1-2 MeV and is negligible for higher energies. The probabilities of photon interaction are calculated from the linear attenuation coefficients and electron densities taken from ICRU Report 46[23]. To take into account different material densities, relationships similar to the relationships for the mass stopping and

scattering powers in VMC were formed[24]. To calculate the parameters of the particles resulting from these interactions, the method is the same as in EGS4.

XVMC can use as input monoenergetic electrons or photons, a phase-space file generated by BEAM, a spectrum or a beam model. If photons emerging from a point source are used (monoenergetic, spectrum or beam model) an initial ray tracing technique is used[24]. This technique calculates the number of photon interactions in each voxel and regular Monte Carlo is used after the interaction. In XVMC, this technique is faster than a regular Monte Carlo algorithm by a factor of about 1.7 to 1.8.

References:

[1]G. Comte de Buffon, "Essai d'arithmétique morale," in *Supplément à l'Histoire Naturelle volume 4* (1777).

[2]S. M. Ulam and J. von Newmann, "On combination of stochastic and deterministic processes," Bull. Amer. Math. Soc. **53**, 1120 (1947).

[3]M. L. Goldberger, "The interac tion of high energy neutrons and heavy nuclei," Phys. Rev. **74**, 1269-1277 (1948).

[4]R. R. Wilson, "Monte Carlo study of shower production," Phys. Rev. **86**, 261-269 (1952).

[5]J. C. Butcher and H. Messel, "Electron number distribution in electron-photon showers," Phys. Rev. **112**, 2096-2106 (1958).

[6]A. A. Varfolomeev and I. A. Svetlolobov, "Monte Carlo calculations of electromagnetic cascades with account of the influence of the medium on bremsstrahlung," Soviet Physics JETP **36**, 1263-1270 (1959).

[7]M. J. Berger, "Monte Carlo Calculation of the penetration and diffusion of fast charged particles," in *Methods in Comput. Phys.*, edited by B. Alder, S. Fernbach, and M. Rotenberg (Academic, New York, 1963), **1**, 135-215.

[8]M. J. Berger and S. M. Seltzer, ETRAN, Monte Carlo code system for electron and photon transport through extended media, RISC computer code, package CCC-107 (Oak Ridge National Laboratory, Oak Ridge, TN, 1973).

[9]R. L. Ford and W. R. Nelson, "The EGS Code system - Version 3," Stanford Linear Accelerator Center Report SLAC-210 (Stanford Calif.) (1978).

[11]M. J. Berger and S. M. Seltzer, "Stopping powers and ranges of electrons and positrons," Report NBSIR 82-2550-A, National Bureau of Standards, Washington D. C. (1983).

[12]ICRU, "Stopping powers for electrons and positrons," ICRU Report 37, International Commission on Radiation Units and Measurements, Bethesda, Maryland (1984).

[13]R. M. Sternheimer, "Density Effect for the Ionization Loss of Charged Particles in Various Substances," Atom. Data and Nucl. Data Tables **30**, 261-271 (1984).

[14]H. Bethe and W. Heitler, "On the stopping of fast particles and on the creation of positive electrons," Proc. Roy. Soc. A. **146**, 83-112 (1934).

[15]H.W. Koch and J.W. Motz, "Bremsstrahlung Cross-section Formulas and Related Data," Review of Modern Physics **31**, 920-955 (1959).

[16]A. F. Bielajew and D.W.O. Rogers, "PRESTA: the Parameter Reduced Electron-Step Transpost Algorithm," Nuclear Instruments and Methods in Physics Reasearch **B18**, 165-181 (1987).

[17]D.W.O. Rogers, "Low energy electron transport with EGS," Nuclear Instruments and Methods in Physics Research **227**, 535-548 (1984).

[18]I. Kawrakow and D. W. O. Rogers, "The EGSnrc Code System: Monte Carlo simulation of electron and photon transport," Technical Report PIRS-701, National Research Concil of Canada, Ottawa, Canada (2000).

[19]D. W. O. Rogers, I. Kawrakow, J. P. Seuntjens *et al.*, "NRC user codes for EGSnrc," Technical Report PIRS-702, National Research Concil of Canada, Ottawa, Canada (2000).

[20]D. W. Rogers, B. A. Faddegon, G. X. Ding *et al.*, "BEAM: a Monte Carlo code to simulate radiotherapy treatment units," Med. Phys. **22**, 503-524. (1995).

[21]I. Kawrakow, M. Fippel, and K. Friedrich, "3D electron dose calculation using a Voxel based Monte Carlo algorithm (VMC)," Med. Phys. **23**, 445-457 (1996).

[22]I. Kawrakow, "Improved modeling of multiple scattering in the Voxel Monte Carlo model," Med. Phys. **24**, 505-517. (1997).

[23]ICRU, "Photon, Electron, Proton and Neutron Interaction Data for Body Tissues," ICRU Report 46, Interantional Commission on Radiation Units and Measurements, Bethesda, Maryland (1992).

[24]M. Fippel, "Fast Monte Carlo dose calculation for photon beams based on the VMC electron algorithm," Med. Phys. **26**, 1466-1475 (1999).

[25]I. Kawrakow and M. Fippel, "Investigation of variance reduction techniques for Monte Carlo photon dose calculation using XVMC," Phys Med Biol **45**, 2163-83. (2000).

Chapter 4

Experimental Verification of Monte Carlo Calculated Dose Distributions for Clinical Electron Beams

I Introduction

With the aim to use Monte Carlo techniques for clinical electron beam treatment planning, we performed a comparison of dose distributions in heterogeneous phantoms calculated using the *fast Monte Carlo* system XVMC[1,2] (see Section III.A of Chapter 3) and using EGSnrc[3] (see Section II.B of Chapter 3) with experimentally measured dose distributions in phantoms constructed of materials of clinical interest. Percent depth doses and lateral profiles were measured and compared to Monte Carlo calculations.

II Materials and methods

II.A Measurements

All irradiations were performed using an isocentric linear accelerator (Clinac 18; Varian, Palo Alto, CA) with a 10x10 cm^2 applicator (15x15 cm^2 jaw setting) and an SSD of 100 cm. Percent depth doses were measured in heterogeneous phantoms using LiF thermoluminescent dosimeters (TLD-700; Harshaw Chemical Company, Solon, OH) with dimensions of 3.2x3.2x0.15 mm^3 in conjunction with a TLD reader (model 3500; Harshaw Chemical Company, Solon, OH). The size of the TLDs allow measuring percent depth dose curves in solid slab phantoms with high resolution near and inside heterogeneities. Before each irradiation, the TLDs were annealed for 1 hour at 400 °C and for 2 hours at 100 °C followed by a cool down period to about 30 °C. Between irradiation and reading, a waiting time of 12-15 hours was taken to reduce the importance of the low temperature glow peaks. A flow diagram of the procedure is shown in Figure 4- 1.

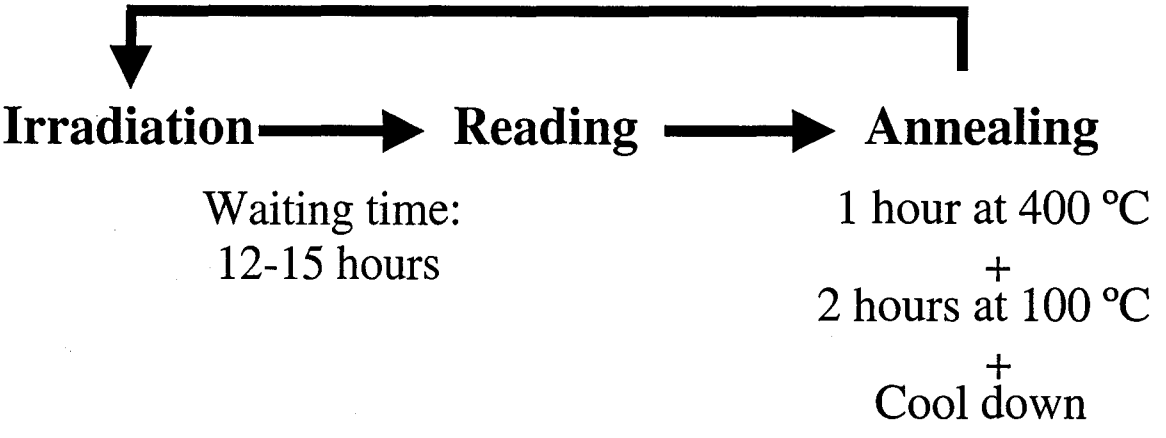

Figure 4- 1. Flow diagram representing the procedure for TLD irradiation, reading and annealing.

A test for linearity was performed in the dose range that was used in this study. The TLDs were placed in Solid Water™ (SW) (model 457; Gamex-RMI, Middleton, WI) at the

depth of dose maximum, d_{max} and the dose to SW was measured by a calibrated ionisation chamber.

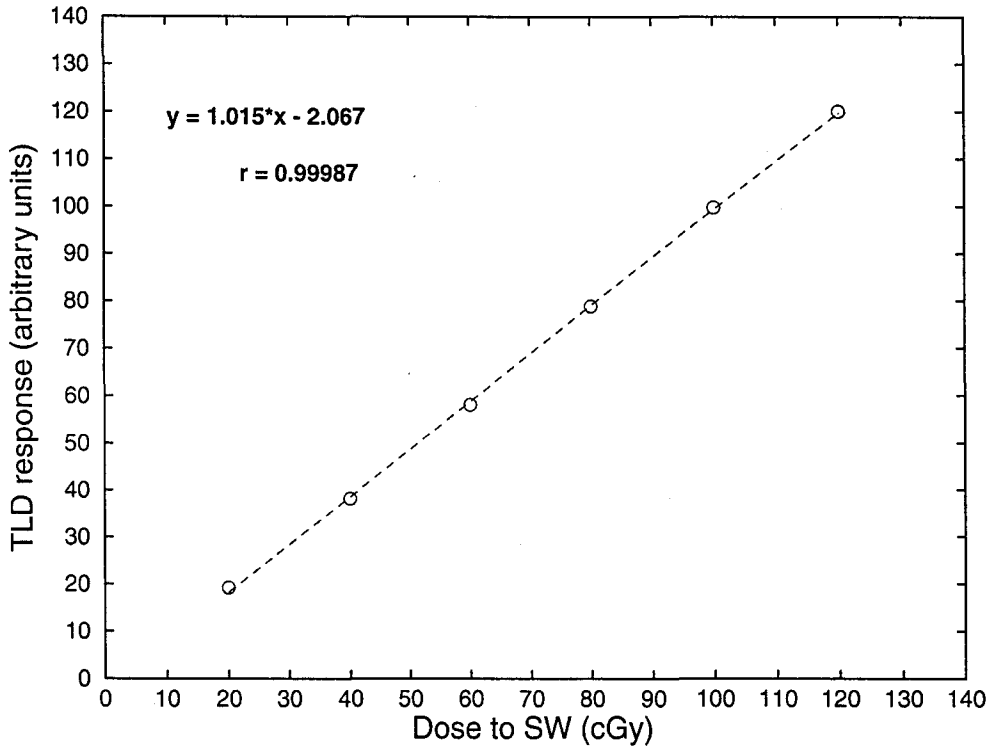

Figure 4- 2. A graph of the linearity test demonstrating the average TLD response for a set of 6 TLDs as a function of dose to SW.

The TLD response (test reading/calibration reading) was measured for 6 TLDs for a dose of 20, 40, 60, 80, 100 and 120 cGy and the average response of the set of 6 TLDs is plotted against the dose to SW in Figure 4- 2. No supralinearity was observed in the dose range studied. Based on Figure 4- 2, a linear behaviour is assumed.

A test for reproducibility was done by performing 6 calibrations for each TLD which yielded an average sample standard deviation for the TLDs of about 0.5%. The calibration consisted of irradiating the TLDs at d_{max} in SW with a known dose measured by a calibrated ion chamber. The calibration reading as a function of the accumulated dose to the medium in which the TLDs are placed for measurements and calibrations is shown in Figure 4- 3 for a typical TLD. The other TLDs used showed similar dose dependence.

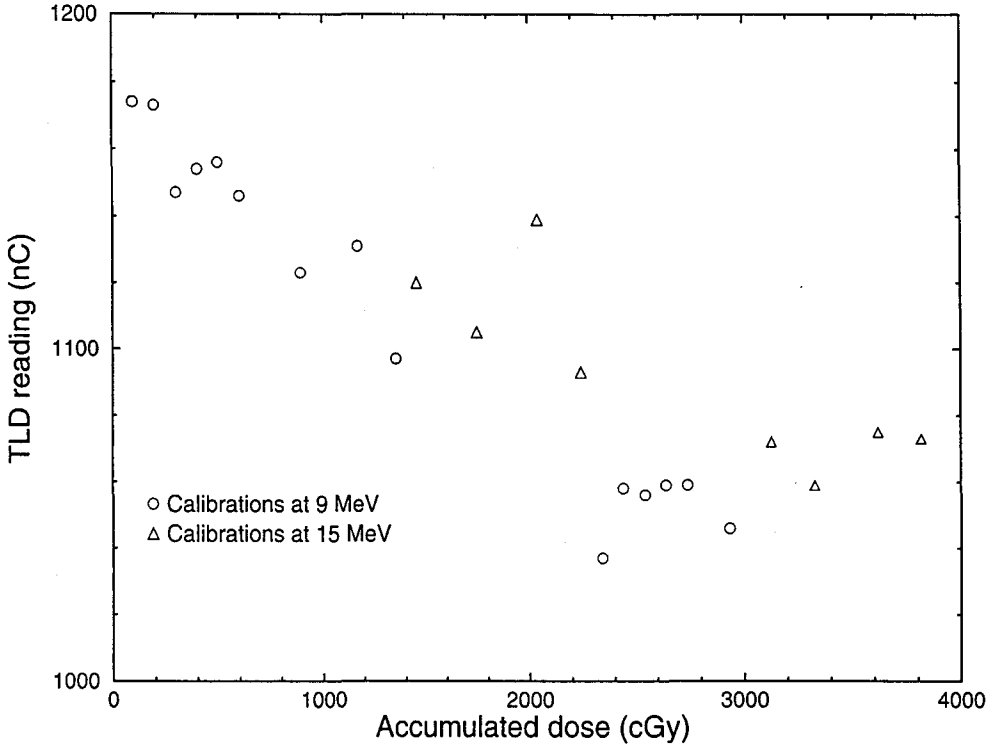

Figure 4- 3. Calibration readings of a typical TLD as a function of the accumulated dose to the medium at the depth of the TLD.

To account for the change in response as a function of the accumulated dose, an individual calibration factor was assigned to each TLD by taking the average of the calibration before and after each experiment. For each percent depth dose measurement, three TLDs were placed in a tight fitting hole in the phantom. All points on the percent depth dose curves are an average of six TLD readings (two experiments with 3 TLDs each). The beams used were the 9 MeV and 15 MeV electron beams from the Clinac 18. The first slab phantom Figure 4- 4(a) consisted of SW with a 1.1 cm layer of bone equivalent material (model SB3; Gammex-RMI, Middleton, WI) placed at a 1 cm depth in the SW. The second slab phantom Figure 4- 4(b) consisted of SW with a 6 cm layer of lung equivalent material (Gammex-RMI, Middleton, WI) placed at 3 cm depth in SW. Percent depth doses were also measured in homogeneous phantoms of SW.

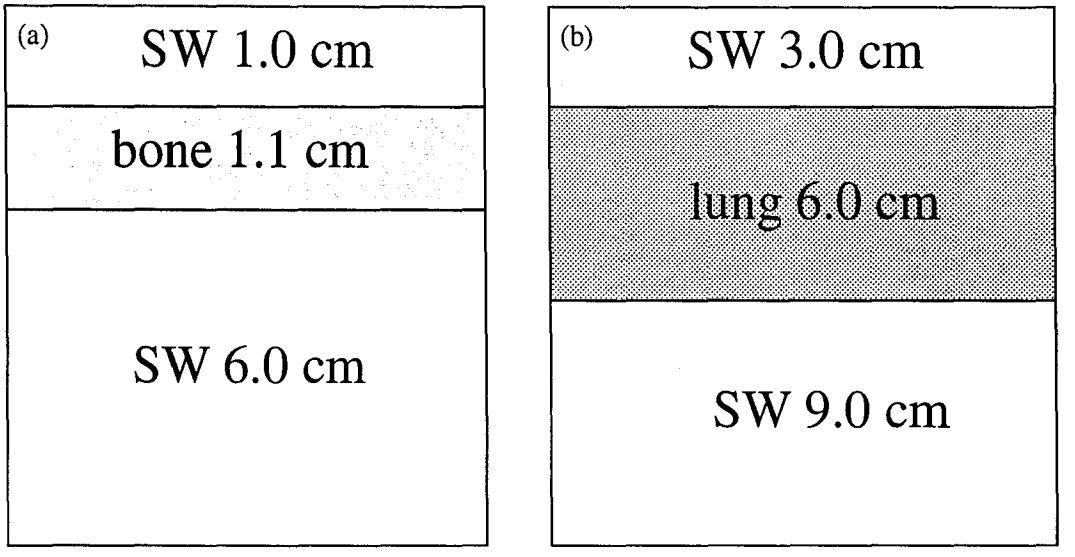

Figure 4- 4. Heterogeneous slab phantoms (not to scale): Panel (a) and (b) shows the SW phantoms containing the bone layer and the lung layer respectively. The beam is incident on the top of the phantoms with its central axis on the centre of the top slabs.

Lateral profiles in water were measured behind aluminum rods (Al 6061) of dimension 0.8x0.8x20 cm^3 using an electron diode (model F1421; Scanditronix, Uppsala, Sweden) in conjunction with a Scanditronix 3-D RFA-300 water tank scanning system for the 9 MeV beam and with a Wellhöfer WP700 3-D water tank scanning system for the 15 MeV beam. The effective measuring volume of the diode has a thickness of 0.06 mm and a diameter of 2.5 mm and was oriented for optimal resolution. The lateral profiles were measured at a depth of 2.6 cm, 3.0 cm and 3.4 cm for the 9 MeV beam and at a depth of 2.5 cm, 4 cm and 5 cm for the 15 MeV beam under different number of rods. For the 9 MeV beam, lateral profiles were measured under 1 and 2 rods. For the 15 MeV beam, lateral profiles were measured under 1, 2, 3 and 4 rods. The rods are placed at 1 cm depth in water and the separation between each rod is 2 cm. The variation in the output of the accelerator was taken into account for the 2-D heterogeneity experiments by using a reference detector placed on the applicator with its sensitive volume in the beam. Figure 4- 5 shows the configuration for 3 and 4 rods.

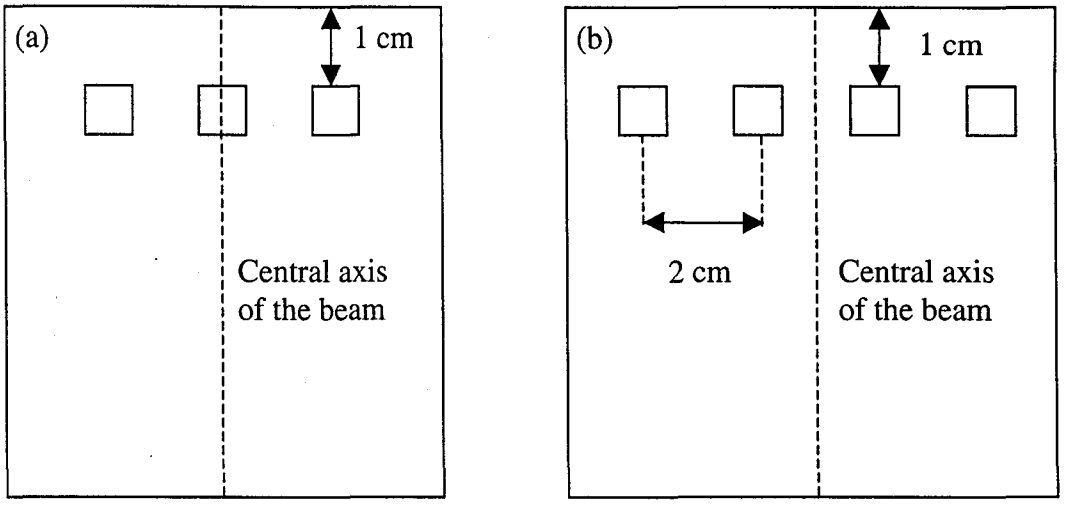

Figure 4- 5. 2-D heterogeneity phantoms (not to scale): Panel (a) and (b) shows the water phantoms containing 3 and 4 rods respectively. Figures for 1 and 2 rods can be deduce from this figure. The beam is incident on top of the phantoms.

II.B Dose to medium from measured detector dose

II.B.1 Method

The dose to the medium was determined from the dose measured by our detectors using the Bragg-Gray relationship,

$$D_{med}(d) = D_{\det}(d,med)\left(\bar{L}/\rho\right)_{\det}^{med}(d,med)P(d,med) \tag{4.1}$$

where $D_{\det}(d) = M_{\det}(d,med)N_{\det}$, $M_{\det}(d,med)$ is the detector reading at depth d in medium, $N_{\det}$ is the dose-to-detector calibration factor, $\left(\bar{L}/\rho\right)_{\det}^{med}(d,med)$ is the Spencer-Attix mean mass restricted collisional stopping power ratio for the medium to detector at a depth d in the medium and $P(d,med)$ is the electron fluence perturbation correction factor at a depth d in the medium. The detectors were calibrated at d_{max} in a homogeneous phantom

denoted as hp (SW or water). Again using the same relationship, the absorbed dose to the detector calibration factor N_{det} was derived from:

$$N_{\text{det}} = N_{hp}\left(\bar{L}/\rho\right)_{hp}^{\text{det}}(d_{\max}, hp)\,P(d_{\max}, hp) \tag{4.2}$$

so that the dose to the medium becomes

$$D_{med}(d) = M_{\text{det}} N_{hp} \frac{\left(\bar{L}/\rho\right)_{\text{det}}^{med}(d, med)}{\left(\bar{L}/\rho\right)_{\text{det}}^{hp}(d_{\max}, hp)} \frac{P(d, med)}{P(d_{\max}, hp)} \tag{4.3}$$

where N_{hp} is the dose-to-homogeneous-phantom (hp) calibration factor obtained from a calibration with a calibrated ionization chamber and application of the AAPM TG-51[4] protocol.

II.B.2 Conversion and correction factors

All measurements were corrected by the ratio of stopping power ratios for the medium to detector specified in Eq.(4.3). For the 1-D heterogeneity cases, the restricted stopping power ratios in equation (3) were calculated using EGSnrc/SPRRZnrc. The calculations used as input the EGS4/BEAM[5] generated phase-space files (see section II.C). The SPRRZnrc user code calculates stopping power ratios using a scoring-on-the-fly technique with the electron fluence at the point of interest[6]. Calculations were done for all depths of measurement in the heterogeneous slab phantoms as well as at $d_{\max}$ in SW. The energy threshold for production of secondary particles was set such that electrons have just enough energy to travel a distance equal to the average chord length of the sensitive volumes of our detectors. The thresholds used for the TLD material was 235 keV.

Some modifications (AUSGAB routine) were made to DOSXYZnrc to allow calculating stopping power ratios for a cartesian geometry. We then used the modified user code to compute stopping power ratios and applied them to the diode measurements. The threshold energy used for the silicon of our diode was 126 keV. It is interesting to look at the variation of $\left(\bar{L}/\rho\right)_{Si}^{water}(d,med)$ as a function of the lateral displacement downstream from 1 aluminum rod (0.8x0.8x20 cm^3) placed at a depth of 1 cm on the central axis (see Figure 4- 5). Figure 4- 6 shows the comparison for the latter phantom and homogeneous water phantom for the 9 MeV beam. Due to the presence of the rod, the relative number of low energy electrons downstream from the rod is increased and therefore the stopping power ratio for water to silicon increases.

No correction for the fluence perturbation of our detectors in the medium was applied to the measured data. These correction factors should be calculated at all points, however, due to calculation time constraints, we have calculated the value of the fluence perturbation correction factor at selected points in the slab phantoms. These results are used to explain some of the differences between measured and calculated points. DOSRZnrc was used to calculate the dose to a simulated TLD at a given depth in a simulated phantom and the dose without the TLD at that same depth. These dose ratios were divided by the corresponding stopping power ratios found with SPRRZnrc to arrive at the fluence perturbation correction factors. The calculated fluence perturbation corrections in the SW/bone phantom, relative to the depth of maximum dose in SW for the 9 MeV beam were 0.996 ± 0.4% at depth 1.0 cm (bone entrance), 1.014 ± 0.4% at depth 1.6 cm (d_{max} in bone region) and 1.017 ± 0.4% at depth 2.1 cm (downstream bone/SW interface); in the SW/lung phantom the correction was 1.029 ± 0.4% at depth of 6 cm for the 9 MeV beam. As expected, the correction decreases with increasing energy at depth.

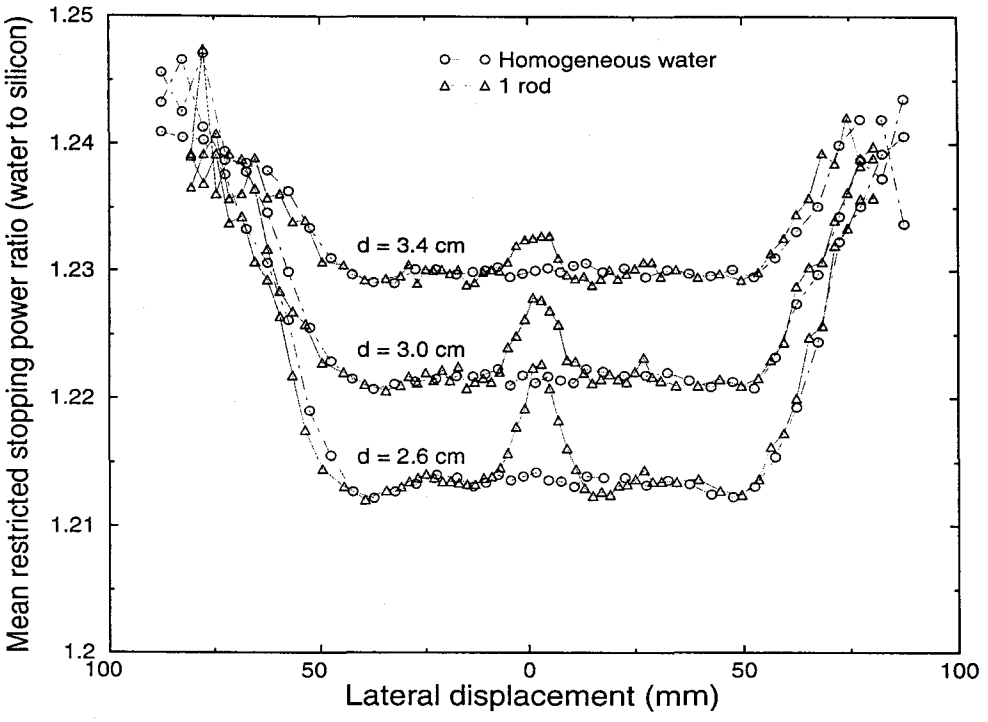

Figure 4- 6. Mean restricted stopping power ratio water to silicon for the 9 MeV beam with the phantom containing 1 aluminum rod.

II.C MC beam characterization

The 9 MeV and 15 MeV beams of the Clinac 18 accelerator were modeled using EGS4/BEAM. The accelerator geometry and component materials were modeled according to the manufacturer's specifications. The information, for about 10^7 particles including the particle position, direction, energy and charge was collected in a phase-space file at a plane corresponding to the surface of our phantoms and used as input for phantom calculations. The energy of the electron pencil beam (radius 1.0 mm) at the exit vacuum window was modified in order to match (within 0.4 mm) R_{50} measured in water with R_{50} calculated using DOSRZnrc/EGSnrc with relativistic spin option turned on and with R_{50} calculated using XVMC which does not have this option. This process is referred to as energy tuning. The depth ionisation curve was measured with a Roos plane parallel chamber (PTW-34001; PTW,

Freiburg, Germany) and the conversion to percent depth dose was performed using the $\left(\bar{L}/\rho\right)_{air}^{water}$ fit as a function of depth from Burns *et al*[7]:

$$\left(\frac{\bar{L}}{\rho}\right)_{air}^{water}(z,R_{50}) = \frac{a+b(\ln R_{50})+c(\ln R_{50})^2+d(z/R_{50})}{1+e(\ln R_{50})+f(\ln R_{50})^2+g(\ln R_{50})^3+h(z/R_{50})} \tag{4.4}$$

where a = 1.0752, b = -0.50867, c = 0.08867, d = -0.08402, e = -0.42806, f =0.064627, g = 0.003085 and h = -0.12460. The depth in water z and R_{50} are expressed in cm.

To verify whether the geometry of the accelerator was modelled properly, measured and calculated lateral profiles were compared. Figure 4- 7 shows the comparison between lateral profiles measured in water with an electron diode and calculation using a BEAM phase-space as the source in DOSXYZnrc for the 9 MeV beam.

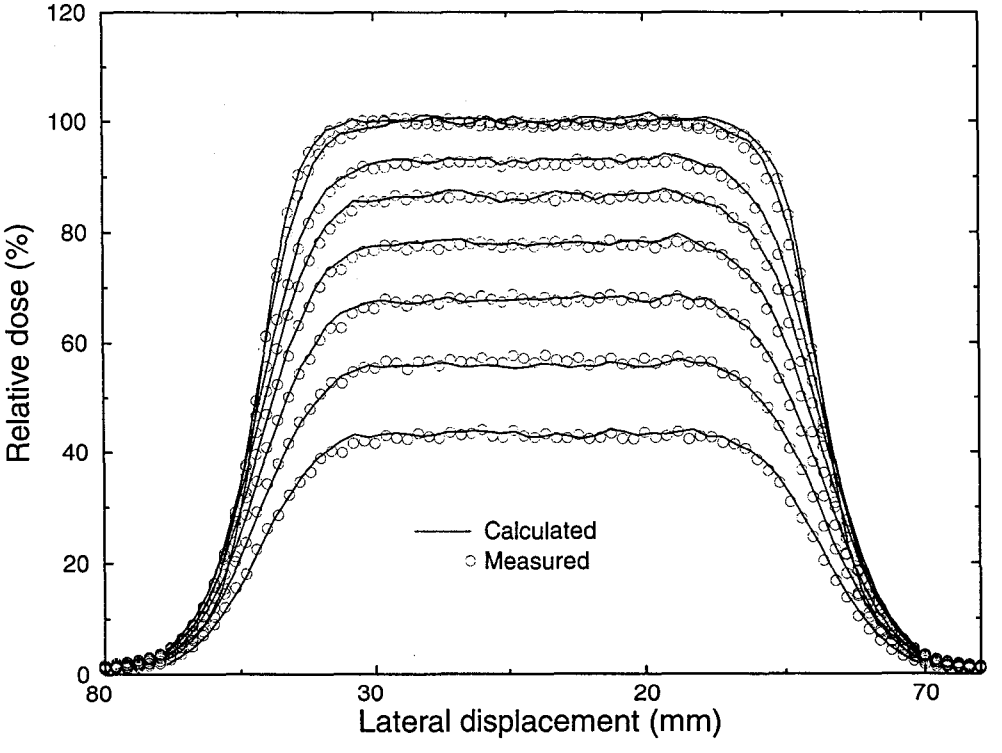

Figure 4- 7. Measured (electron diode) and calculated (DOSXYZnrc) lateral profiles in water for the 9 MeV beam at depths 1.8, 2.2, 2.6, 2.8, 3.0, 3.2, 3.4 and 3.6 cm after energy tuning of the phase-space where the primary energy was 9.4 MeV.

An energy tuning was done at the time of performing the slab phantom experiments and one at the time for the 2-D heterogeneity experiments. The first energy tuning resulted in 9.4 MeV and 15.1 MeV for EGSnrc and 9.5 MeV and 15.2 MeV for XVMC. The second energy tuning, which was done based on measurements performed about one year after the first energy tuning resulted in 9.5 MeV and 15.1 MeV for EGSnrc and 9.6 MeV and 15.2 MeV for XVMC. Figure 4- 8 shows the first energy tuning.

In Figure 4- 8, the measured and calculated curves agree very well except near the surface where the measurement points are systematically higher than calculations. This is due to the inability of our chamber to measure the dose accurately close to the surface.

In XVMC, a beam model (BM) was also used to characterise the Clinac 18 beams. A BM has the advantage of saving disk space and as with a phase-space, the source can be parameterised based on experimental measurements on the accelerator of interest. The BM is a geometric simplification of a phase-space.

Using the XVMC beam model, particles are sampled from two discrete sources, one representing the primary source and one representing the applicator. The energy of these sources is sampled from a parameterised spectrum. The parameters of the sources as well as their energy distribution require adjustment of fit parameters to the following experimental data sets: dose fall-off in air as a function of distance from the source, lateral profiles at 100 cm, 110 cm and 120 cm in air and percent depth dose in water at 100 cm SSD. In this work, the optimisation of the parameters, as above, is referred to as BM 1.

For the Clinac 18, when using this BM as a source for dose calculations in water, the dose near the penumbra of the lateral profiles occasionally underestimated the measured profile values. For lateral profile comparisons, we therefore further optimised the parameters of the BM so as to match measured lateral profiles in homogeneous water and used the latter parameters, referred to as BM 2, for further heterogeneous phantom calculations.

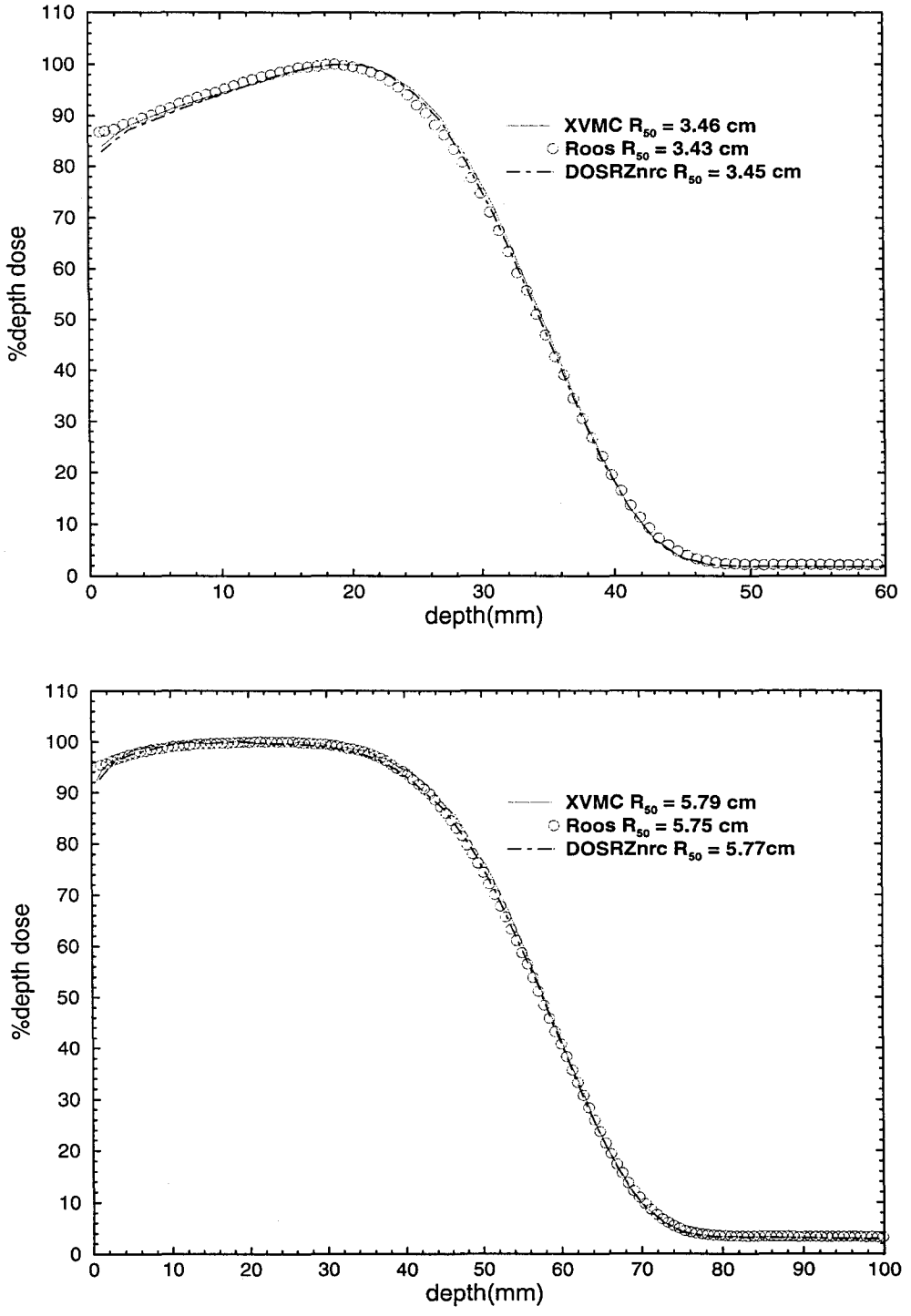

Figure 4- 8. Percent depth dose curves after the energy was optimized to match R_{50} from measurements and calculations for: (a) 9 MeV beam and (b) 15 MeV beam.

Figure 4- 9 shows comparisons of measured lateral profiles in water at depth 3.0 cm for the 9 MeV beam and at depth 2.5 cm for the 15 MeV beam with calculations using XVMC

with the parameters optimised to match the 3 previous experimental data sets (BM 1) and the parameters modified to match measured lateral profiles in water (BM 2).

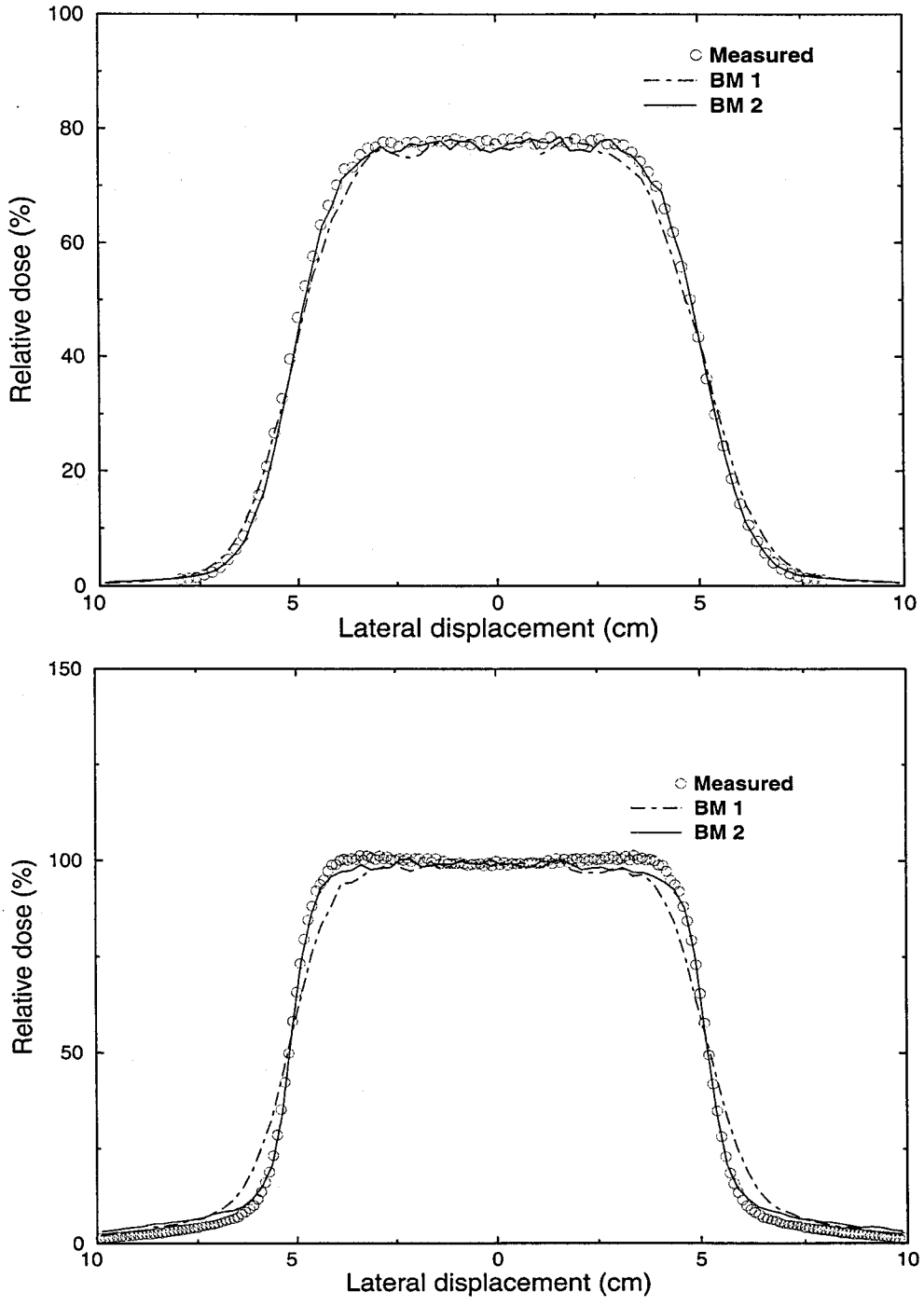

Figure 4- 9. Measurements (electron diode) and calculations using XVMC with BM 1 and BM 2 of lateral profiles in water at depth 3.0 cm for: (a) 9 MeV beam and (b). 15 MeV beam.

As mentioned, the BM 2 yields better agreement with measurements.

II.D MC calculation of dose distributions

For dose calculations with EGSnrc, the transport parameters *ECUT* = 521 keV and *PCUT* = 10 keV were used and the number of histories was selected in order to get a type A uncertainty on the dose calculations of about 0.2 to 0.4% near the point of maximum dose in the specific calculations. For calculation of dose distributions in the slab phantoms, the user code DOSRZnrc was used since cylindrical symmetry increases calculation efficiency for slab geometry. For dose distributions in the 2-D heterogeneity phantoms the user code DOSXYZnrc was used. For EGSnrc calculations, the materials were simulated with the compositions given by the manufacturer combined with measured densities. The percentage composition for the SW, lung, bone materials are shown in Table 4- 1.

The percentage composition of the aluminum 6061 rods was Al 0.97875, Mg 0.01, Si 0.006, Cu 0.00275 and Cr 0.0025. The composition of the materials does not need to be specified in XVMC, rather a scaling according to the density is used (see section III of chapter 3).

Table 4- 1. Percentage composition of the materials used for the slab phantoms.

Material	Atomic symbol					
	H	C	N	O	Cl	Ca
Lung	8.62	68.87	2.26	17.62	0.11	2.52
Bone	3.1	31.26	0.99	37.57	0.05	27.03
SW	8.09	67.22	2.4	19.84	0.13	2.32

The measured densities were 1.84 g/cm^3 for the bone equivalent material, 2.7 g/cm^3 for the aluminum rods, 0.27 g/cm^3 for the lung equivalent material and 1.035 g/cm^3 for SW. These densities and a density of 1.0 g/cm^3 for water were used for the materials simulated in the EGSnrc calculations, but for XVMC a density of 0.998 g/ cm^3 was used for SW. This density was different than the measured physical density since the interaction data (collisional and radiative stopping powers) for SW did not fall on the numerical fits relating them to

physical density[8] (see Eq. (3.10) and Eq. (3.11) of Chapter 3) . So, using the energy optimised for R_{50} in water, an additional optimisation of the density for SW was performed to match R_{50} in SW from XVMC to R_{50} in SW from the EGSnrc calculations (3.48 cm), as shown in Figure 4- 10.

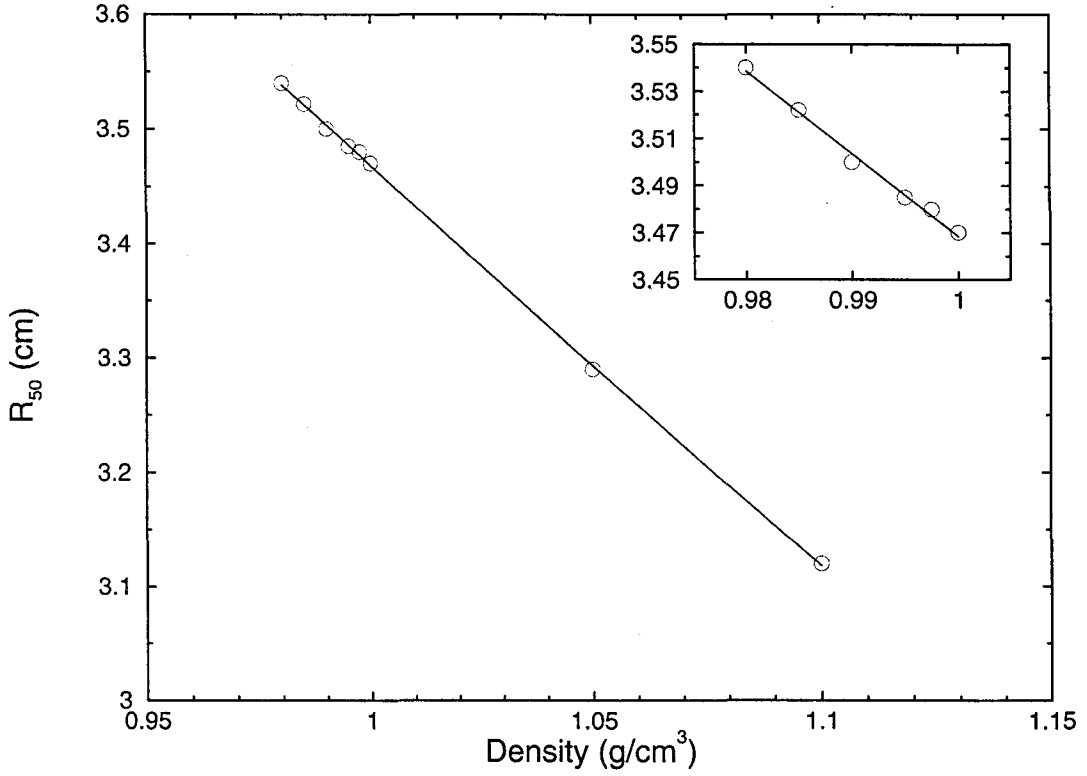

Figure 4- 10. R_{50} calculated with the *fast Monte Carlo* system XVMC as a function of density of SW for the 9 MeV electron beam. The purpose of the density was to reproduce R_{50} calculated with EGSnrc.

The EGSnrc calculations were performed on a 24 Pentium III 500 to 900 MHz CPU parallel processing platform. The XVMC calculations were performed on a single Pentium III 500 MHz CPU. A test to compare the speed of the different codes was done by simulating the 9 MeV beam incident on a 20x20x20 cm^3 water phantom with voxels of 0.5x0.5x0.5 cm^3. To obtain a 2% average statistical uncertainty in regions where the dose is larger than 50%, it took about 45 minutes with all processors in parallel for DOSXYZnrc, 8 minutes for XVMC when using the phase-space file and 30 seconds for XVMC when using the beam model.

III Results and discussions

III.A Homogeneous and heterogeneous slab phantoms

Percent depth doses for homogeneous phantoms of SW are shown in Figure 4- 11 and Figure 4- 12. Percent depth doses for heterogeneous phantoms are shown in Figure 4- 16. As mentioned before, the measured points represent an average of six TLD readings. Both measured and calculated curves are normalised to 100% at the depth of dose maximum in SW. As mentioned before, the measured data were corrected by the restricted stopping power ratios. For what follows, percentage differences are quoted as the percentage of the dose at d_{max} in SW (not as percentage of the local dose).

For the homogeneous SW phantom irradiated with a 9 MeV beam, all calculations are in agreement with measurements to within 2% except for 2 points. For the same phantom with the 15 MeV beam, all calculations are in agreement with measurements to within 2%.

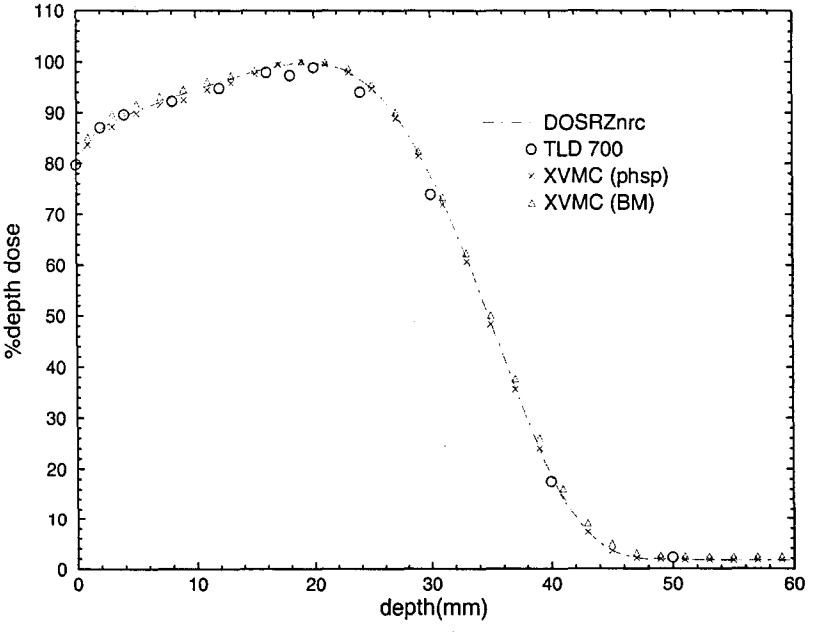

Figure 4- 11. Percent depth dose in SW for the 9 MeV beam measured with TLDs (o) and calculated with DOSRZnrc (dashed line) and with the *fast Monte Carlo* system XVMC using a phase-space (x) and using its BM (Δ).

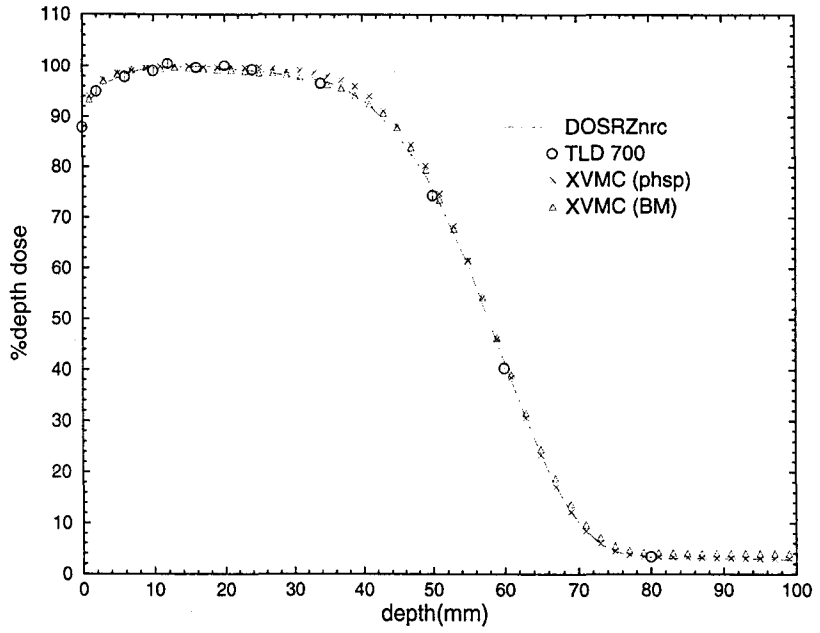

Figure 4- 12. Percent depth dose in SW for the 15 MeV beam measured with TLDs (o) and calculated with DOSRZnrc (dashed line) and with the *fast Monte Carlo* system XVMC using a phase-space (X) and using its BM (Δ).

For the SW/bone phantom irradiated with a 9 MeV beam (see Figure 4- 13), the agreement between measurements and calculations is excellent upstream and downstream from the bone region. However, inside the bone, the difference between measurements and calculations is less than 2% for DOSRZnrc, less than 2% for XVMC using the phase-space (phsp) file, and less than 1% for XVMC using the BM. Some of the discrepancy inside the bone region can be explained by the fact that the fluence perturbation correction factors mentioned previously were not used to correct the data. The fluence perturbation correction at depth of 16 mm, if applied, would increase the measured point by 1.4% making the agreement better.

For the same phantom irradiated with a 15 MeV beam (see Figure 4- 14), the agreement between measurements and calculations is within 1% before the bone. Inside the bone, the agreement between measurements and calculations is within 0.5% for DOSRZnrc and XVMC (BM) and 1.5% for XVMC (phsp). Downstream from the bone, the agreement with measurements is within 1% for DOSRZnrc and 2% for XVMC calculations.

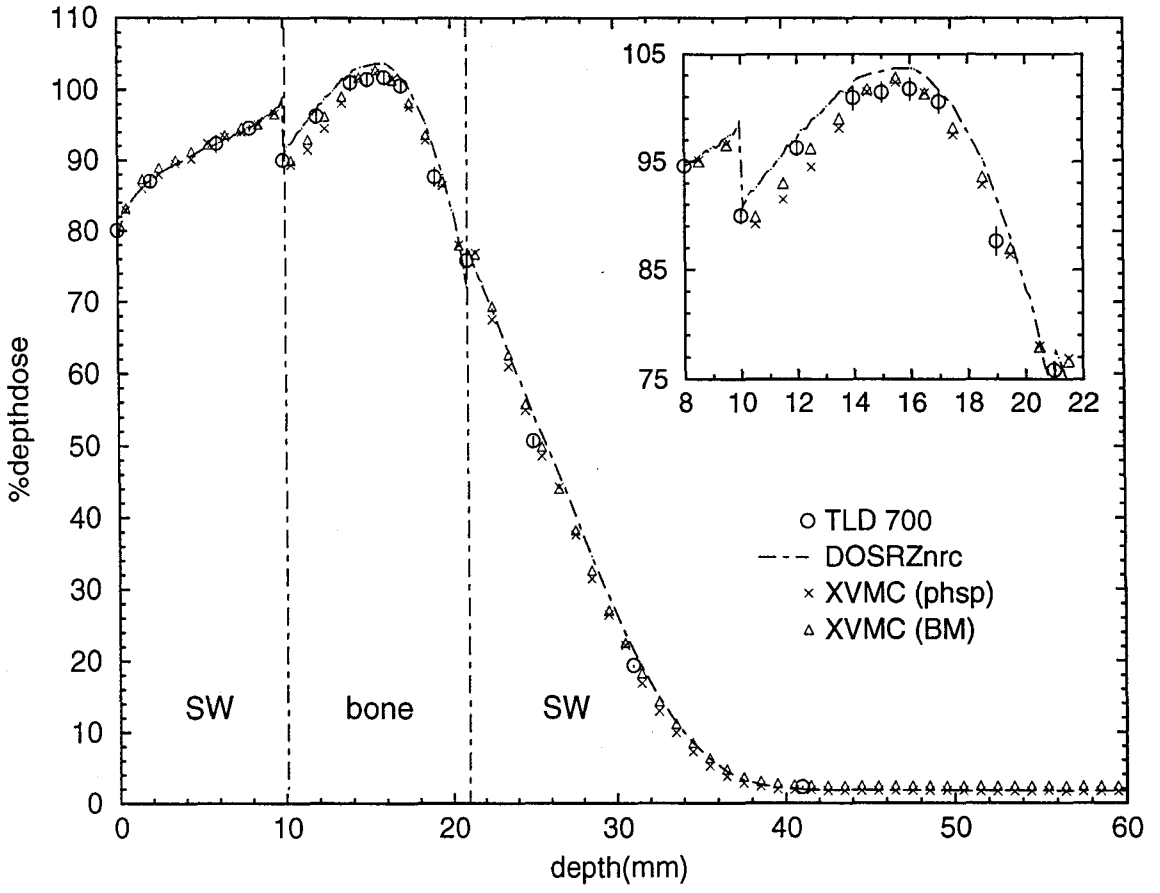

Figure 4- 13. Percent depth dose in the SW/bone phantom for the 9 MeV beam measured with TLDs (o) and calculated with DOSRZnrc (dashed line) and with the *fast Monte Carlo* system XVMC using a phase-space (X) and using its BM (Δ).

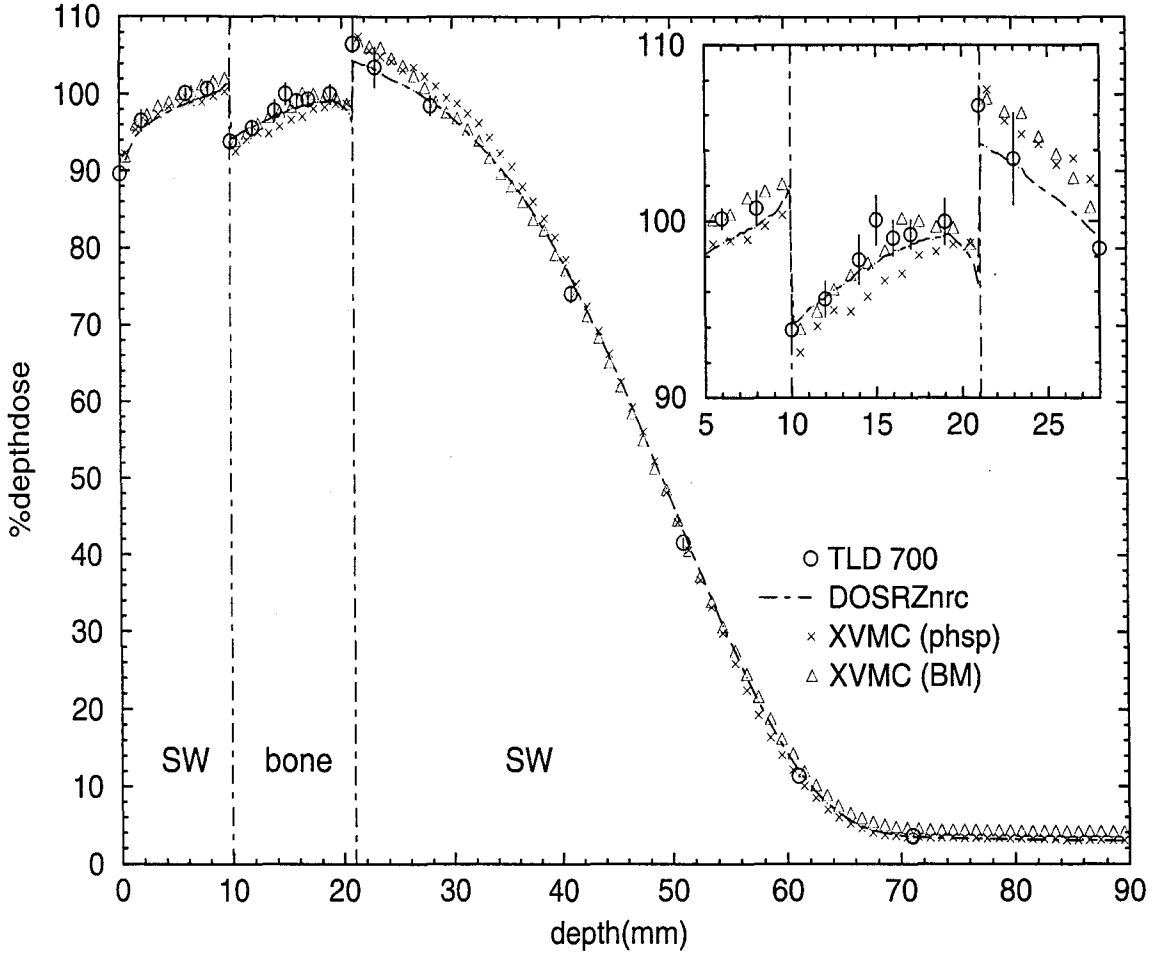

Figure 4- 14. Percent depth dose in the SW/bone phantom for the 15 MeV beam measured with TLDs (o) and calculated with DOSRZnrc (dashed line) and with the *fast Monte Carlo* system XVMC using a phase-space (x) and using its BM (Δ).

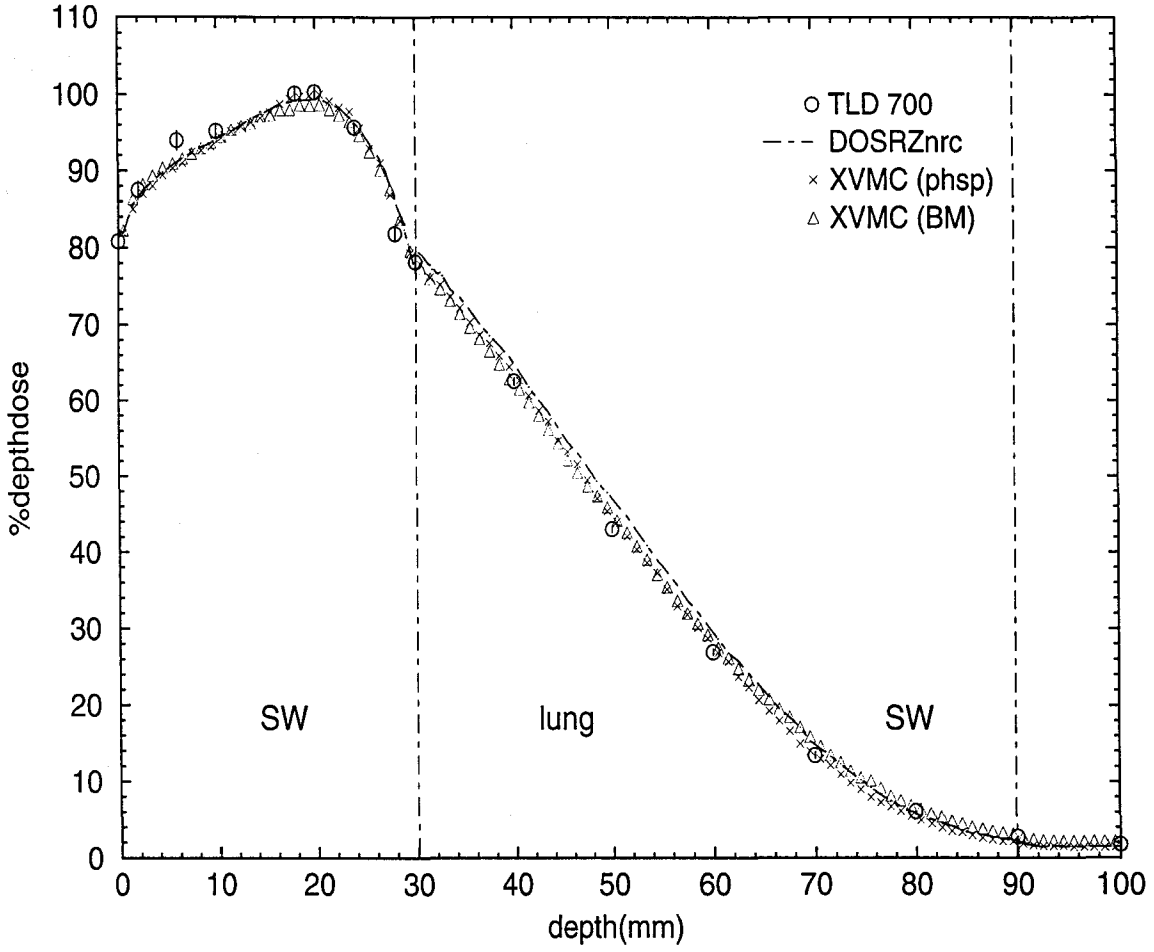

Figure 4- 15. Percent depth dose in the SW/lung phantom for the 9 MeV beam measured with TLDs (o) and calculated with DOSRZnrc (dashed line) and with the *fast Monte Carlo* system XVMC using a phase-space (X) and using its BM (Δ).

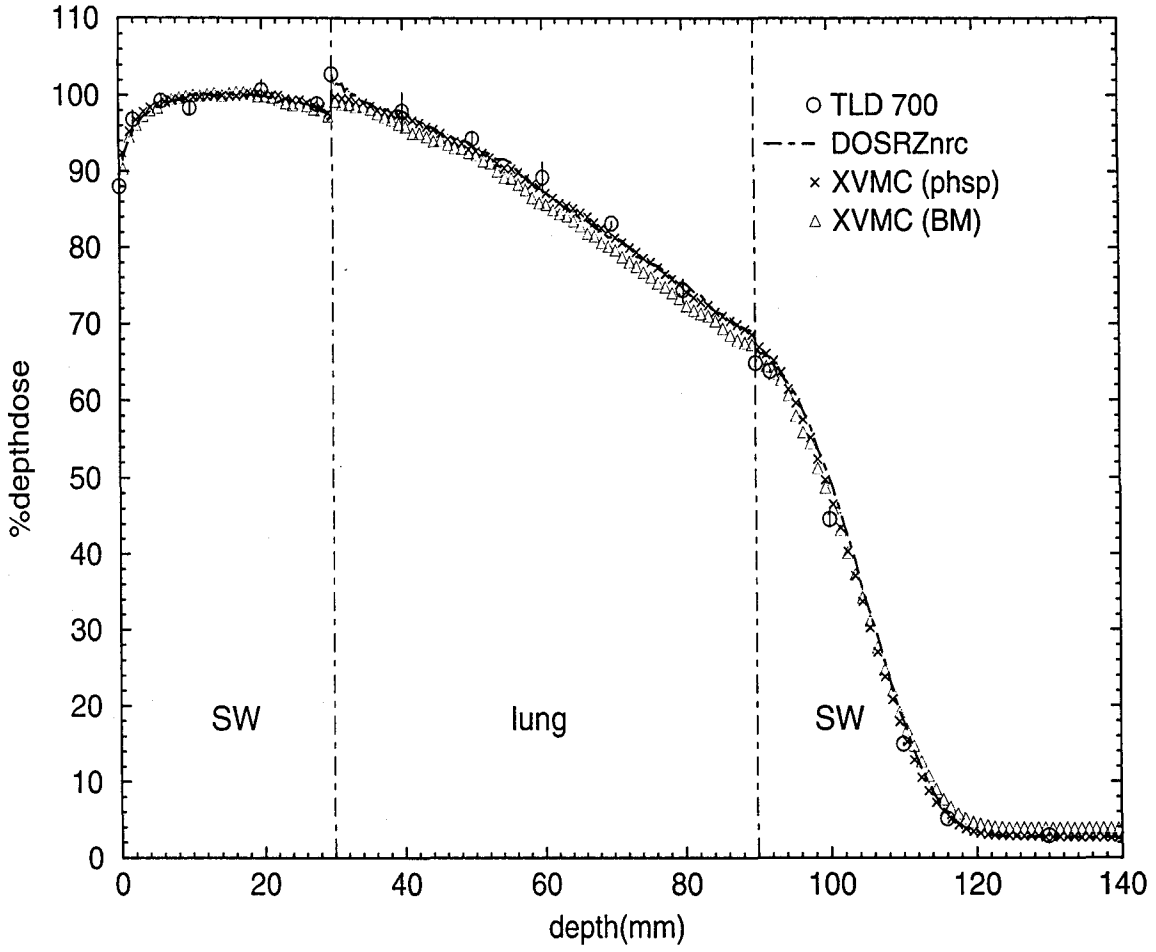

Figure 4- 16. Percent depth dose in the SW/lung phantom for the 15 MeV beam measured with TLDs (o) and calculated with DOSRZnrc (dashed line) and with the *fast Monte Carlo* system XVMC using a phase-space (X) and using its BM (Δ).

For the SW/lung phantom irradiated with a 9 MeV beam (see Figure 4- 15), the agreement with measurements is within 2% before the lung for all calculations except for one point where the difference is 3%. Inside the lung, the agreement is within 2.5% for all calculations, however, if the calculated fluence perturbation correction factor in lung at 60 mm (1.029 ± 0.4%) had been applied, the agreement would have been improved.

For the same phantom irradiated with a 15 MeV beam (see Figure 4- 16), the agreement with measurements is within 1% before the lung for all calculations. Inside the lung, the agreement with measurements is within 1% for DOSRZnrc, 2% for XVMC (phsp) and 3% for XVMC (BM).

It should be noted that the lung material is not of uniform density as in the calculations (0.27 g/cm^3) but rather consists of air cavities distributed over a material of lung composition with normal tissue density. Reported differences[9] in density effect between the latter and a homogeneous lung material of 0.27 g/cm^3 density may explain some of the discrepancies found in the dose calculation in the phantom containing the lung equivalent material.

III.B 2-dimensional heterogeneities

The results for the 2-D heterogeneity phantoms are shown in Figure 4- 17 to Figure 4- 22. Both the calculated and measured curves were normalised to 100% at the depth of dose maximum in water. Again, the measured profiles were corrected solely by stopping power ratios. In the following section, the percentage values are percentage of dose maximum in a homogeneous water phantom.

For the 1 rod phantom irradiated with a 9 MeV beam (see Figure 4- 17(a)), all calculations are in agreement with measurements to within 1% at depths 2.6 cm and 3.4 cm and within 2% at depth 3.0 cm.

For the phantom containing 2 rods irradiated with a 9 MeV beam (see Figure 4- 18(a)) at depth 2.6 cm, the calculations are in agreement with measurements to within 1% near the global maxima region. Downstream from the rods, the agreement with

measurements is within 1% for XVMC calculations and within 2% for DOSXYZnrc. On the central axis, the measured dose is underestimated by DOSXYZnrc and XVMC (BM) by about 2.5% and by 4% for XVMC (phsp). At a depth of 3.0 cm, the agreement with measurements is within 1.5% for all calculations except on central axis where XVMC (phsp) is in agreement with the measurements to within 2%. At a depth of 3.4 cm, all calculations are in agreement with measurements to within 1.5%.

For the phantom containing 1 rod irradiated with a 15 MeV beam (see Figure 4-19(a)) at depth 2.5 cm, calculations are in agreement with measurements to within 1% except on the edge of the lateral profiles where XVMC (BM) underestimates the measured dose by about 2%. For the 15 MeV beam of the Clinac 18, it was not possible to obtain a good agreement between measured and calculated lateral profiles in homogeneous water using our BM 2 in XVMC. An underestimation of dose near the penumbra (see Figure 4- 9(b)) resulted in the same phenomenon for the comparison of lateral profiles in heterogeneous phantoms. At a depth of 4.0 cm, the agreement is within 1% except on the edge of the profiles where XVMC (BM) underestimates the measured dose by about 2%. At a depth of 5.0 cm, the agreement is within 1% for DOSXYZnrc and 2% for XVMC calculations.

For the phantom containing 2 rods irradiated with a 15 MeV beam (see Figure 4-20(a)) at depth 2.5 cm, the calculations are in agreement with measurements to within 1.5% except on the edge of the lateral profiles where XVMC (BM) underestimates the measured dose by about 2.5%. At a depth of 4.0 cm, the agreement is within 2% except on the edge of the lateral profiles were XVMC (BM) underestimates the measured dose by about 3%. At depth 5.0 cm, the agreement is within 2% for all calculations.

For the phantom containing 3 rods irradiated with a 15 MeV beam (see Figure 4-21(a)), the dose underestimation by XVMC (BM) can also be seen at a depth of 2.5 cm and 4.0 cm. At a depth of 2.5 cm and 4.0 cm, the agreement between measurements and calculations is within 2%. At a depth of 5.0 cm, the agreement with measurements is within 1% for DOSXYZnrc and XVMC (BM) and within 2% for XVMC (phsp).

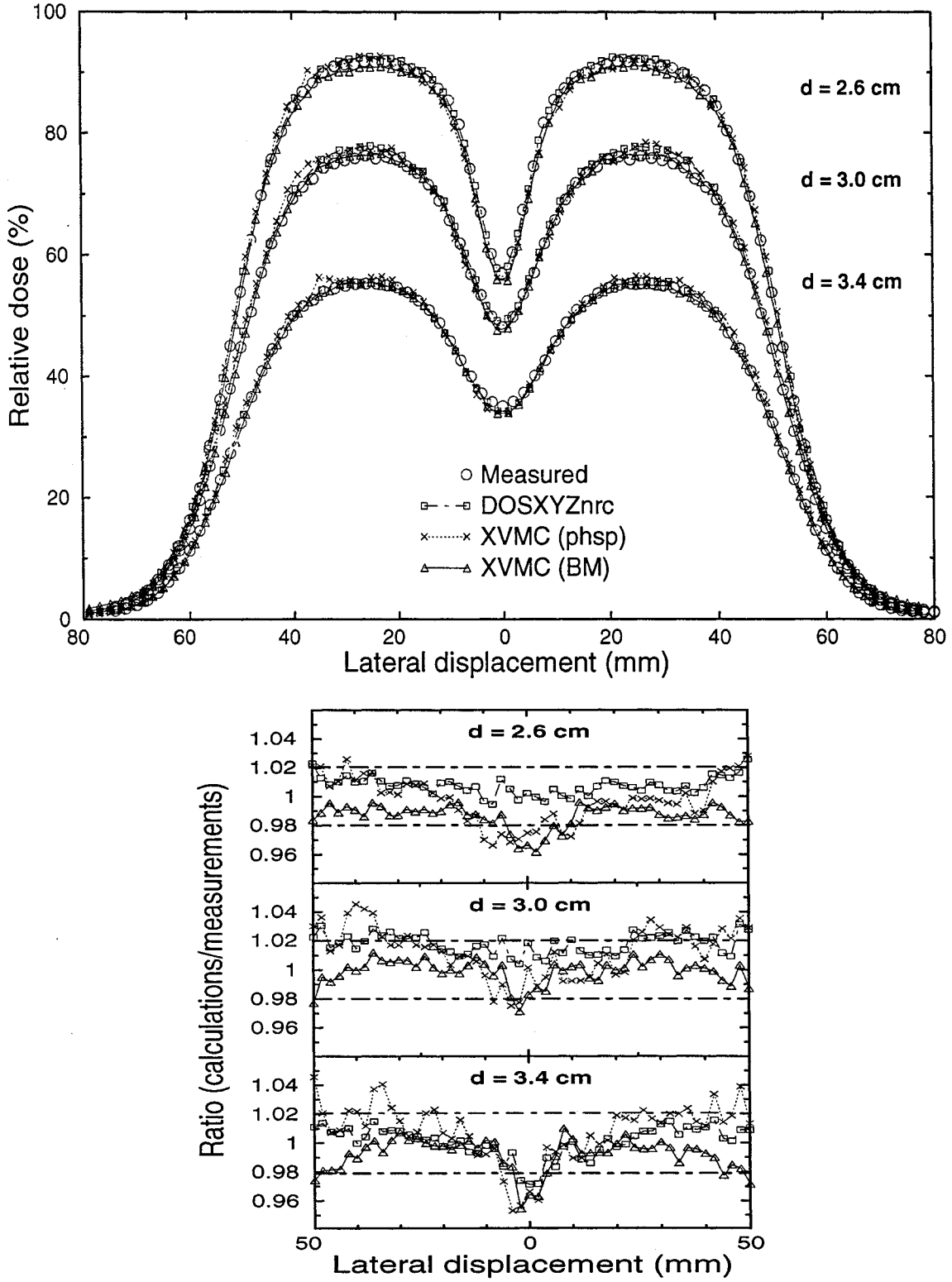

Figure 4- 17. Lateral profiles (a) and ratio calculations/measurements (b) in the water phantom containing 1 rod for the 9 MeV beam: measured with TLDs (o) and calculated with DOSRZnrc (dashed line) and with the *fast Monte Carlo* system XVMC using a phase-space (X) and using its BM (Δ).

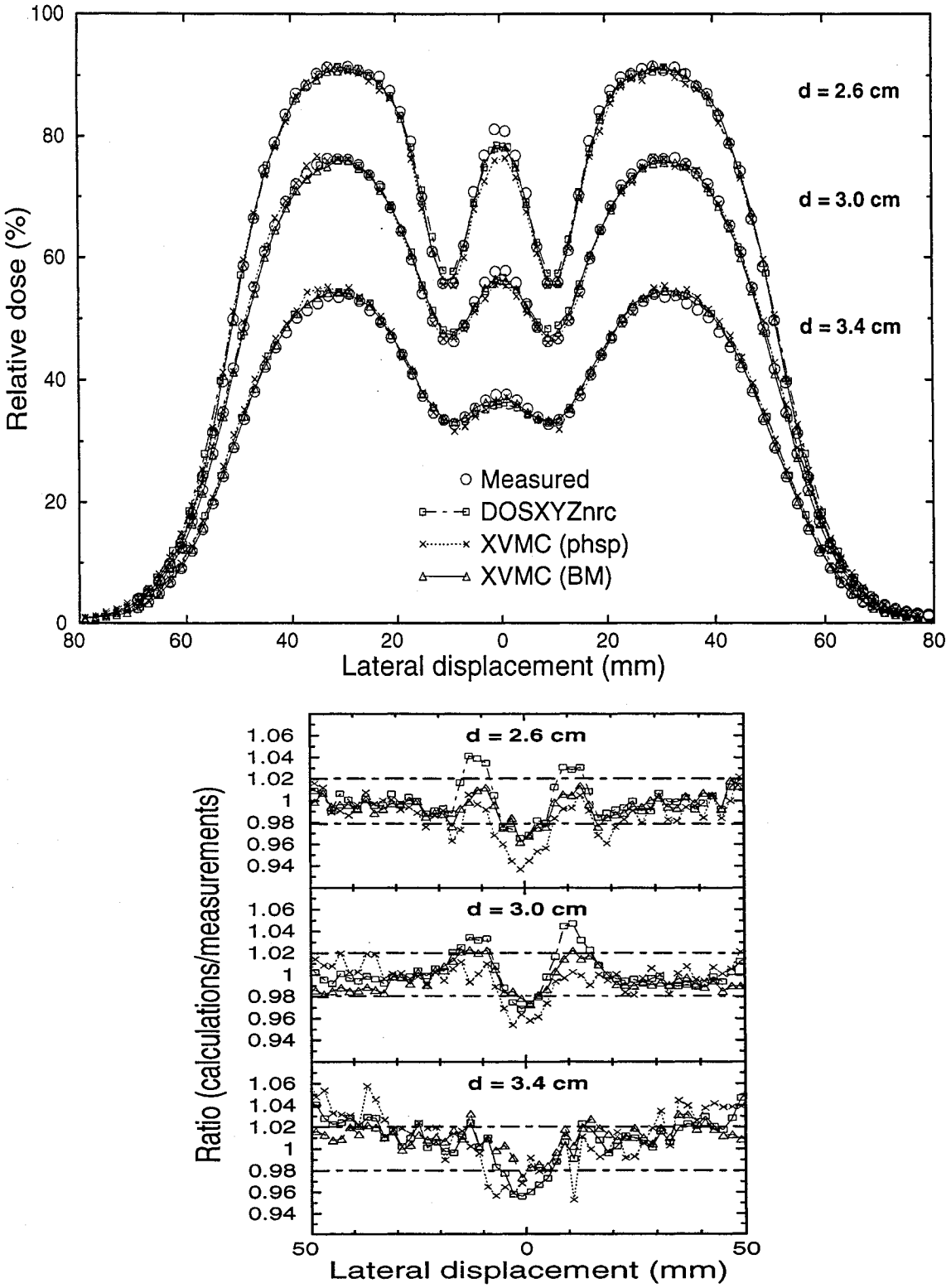

Figure 4- 18. Lateral profiles (a) and ratio calculations/measurements (b) in the water phantom containing 2 rods for the 9 MeV beam: measured with TLDs (o) and calculated with DOSRZnrc (dashed line) and with the *fast Monte Carlo* system XVMC using a phase-space (X) and using its BM (Δ).

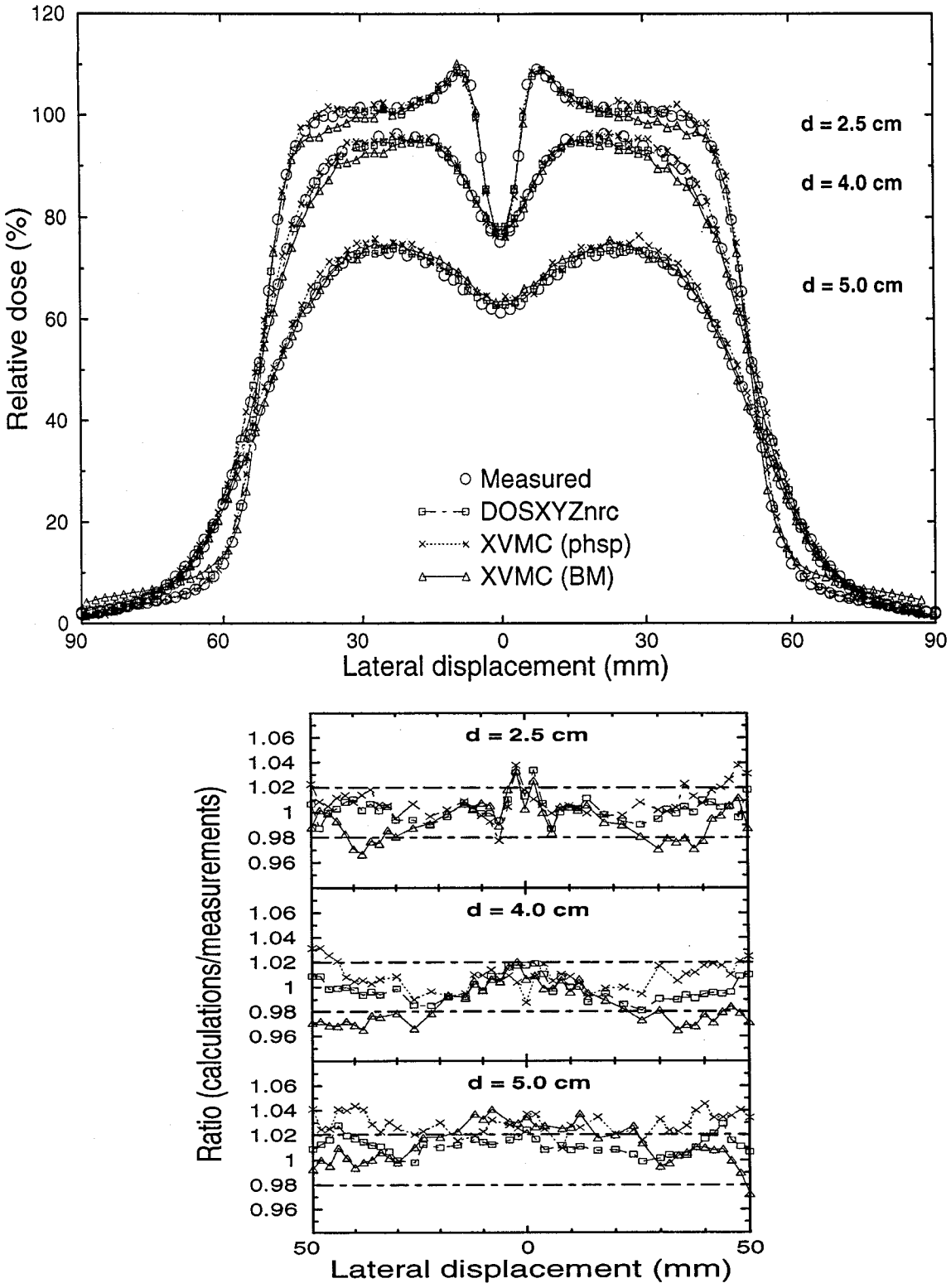

Figure 4- 19. Lateral profiles (a) and ratio calculations/measurements (b) in the water phantom containing 1 rod for the 15 MeV beam: measured with TLDs (o) and calculated with OSRZnrc (dashed line) and with the *fast Monte Carlo* system XVMC using a phase-space (X) and using its BM (Δ).

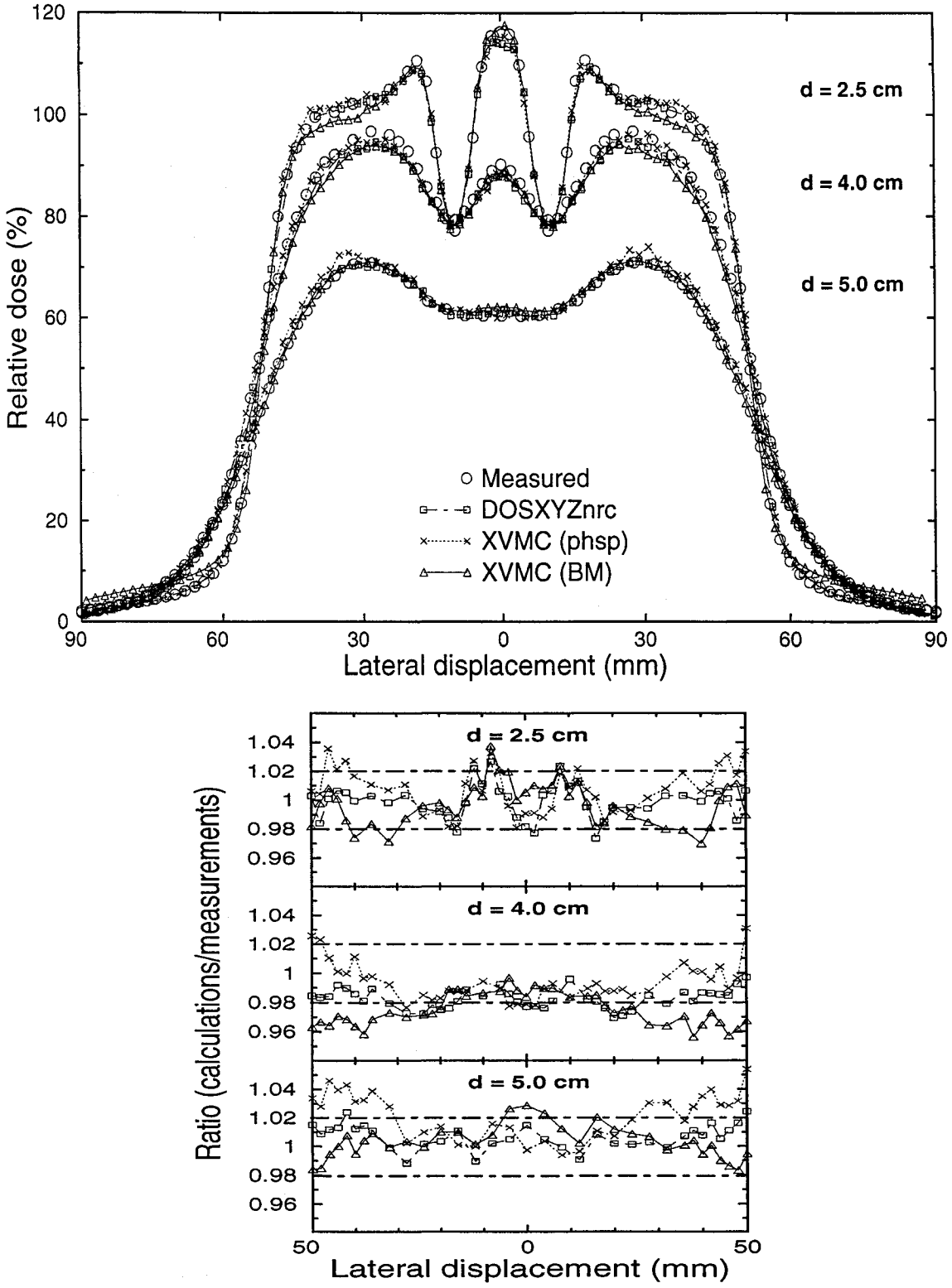

Figure 4- 20. Lateral profiles (a) and ratio calculations/measurements (b) in the water phantom containing 2 rods for the 15 MeV beam: measured with TLDs (o) and calculated with DOSRZnrc (dashed line) and with the *fast Monte Carlo* system XVMC using a phase-space (X) and using its BM (Δ).

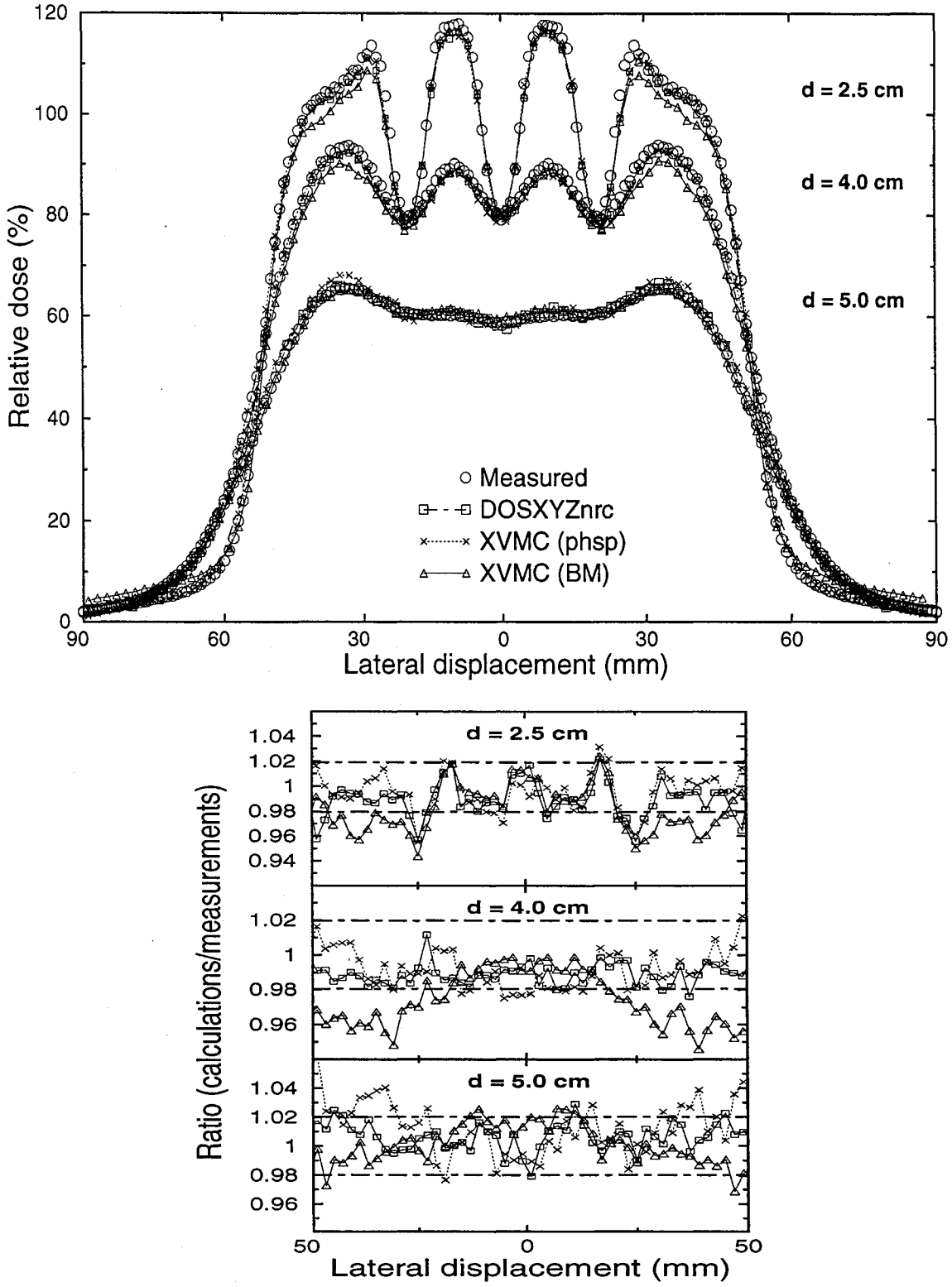

Figure 4- 21. Lateral profiles (a) and ratio calculations/measurements (b) in the water phantom containing 3 rods for the 15 MeV beam: measured with TLDs (o) and calculated with DOSRZnrc (dashed line) and with the *fast Monte Carlo* system XVMC using a phase-space (X) and using its BM (Δ).

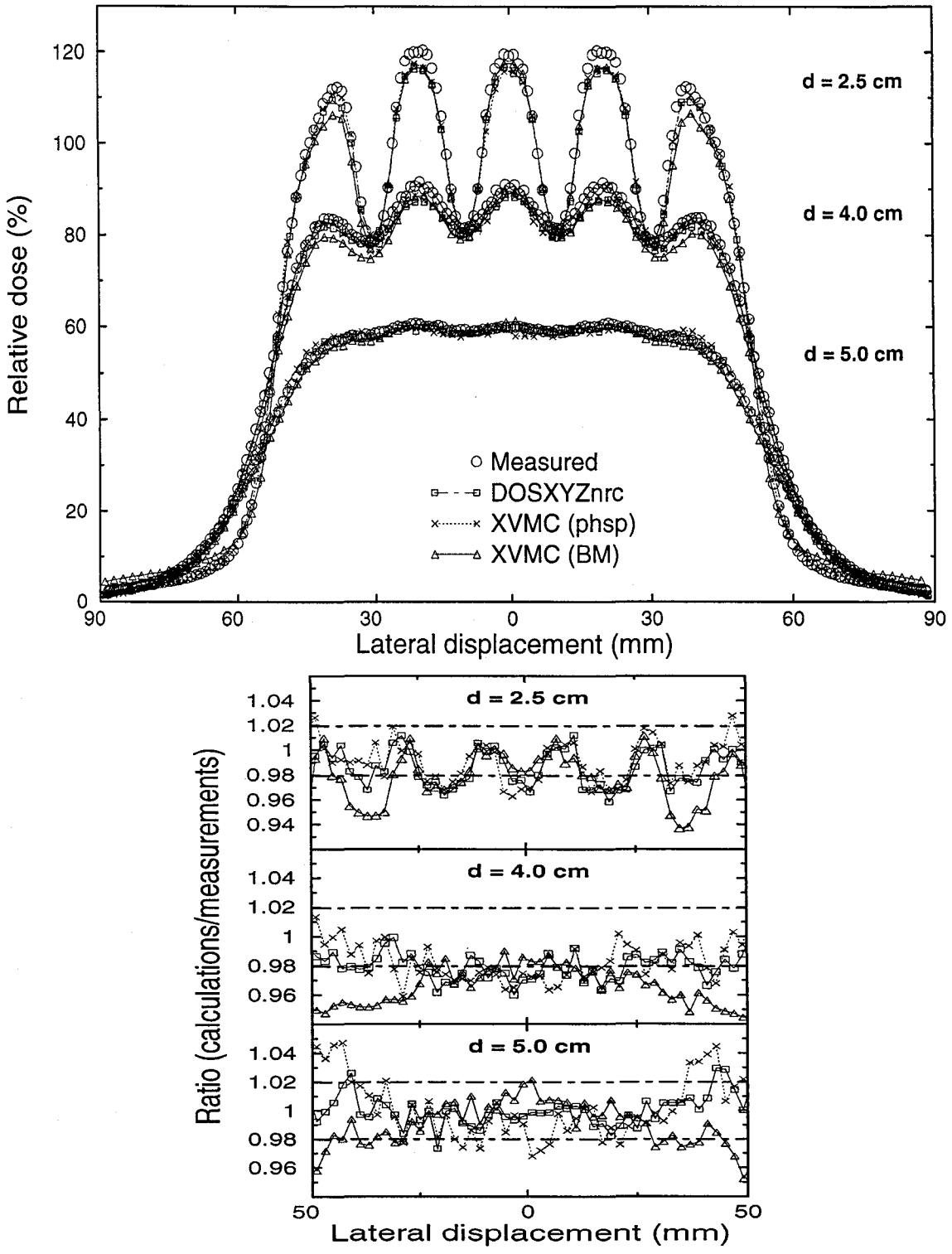

Figure 4- 22. Lateral profiles (a) and ratio calculations/measurements (b) in the water phantom containing 4 rods for the 15 MeV beam: measured with TLDs (o) and calculated with DOSRZnrc (dashed line) and with the *fast Monte Carlo* system XVMC using a phase-space (X) and using its BM (Δ).

For the phantom containing 4 rods irradiated with a 15 MeV beam (see Figure 4-22(a)), the underestimation of dose by XVMC (BM) can also be seen at depths of 2.5 cm and 4.0 cm. The agreement between measurements and calculations is within 3% and 2.5% at depths 2.5 cm and 4.0 cm respectively. At a depth of 5.0 cm, the agreement with measurements is within 1%.

To investigate in more detail the effect of the rods, the ratios calculations/measurements are shown in Figure 4- 17(b), Figure 4- 18(b), Figure 4- 19(b), Figure 4- 20(b), Figure 4- 21(b), and Figure 4- 22(b). Points are not shown for the penumbra region because the dose values are small in this region and the plotted ratios would show large values. In these graphs, lines representing the region of ±2% variation on the local dose were drawn and the majority of the points for these ratios are within the ±2% region. For the phantom containing 2 rods irradiated with a 9 MeV beam (see Figure 4- 18(b)) there seems to be a trend at a depth of 2.6 cm and 3.0 cm that produces a dose underestimation on the central axis and a dose overestimation downstream from the rods which may suggest some fluence perturbation effects. A more precise energy optimisation of the beams would not change this trend significantly. For the 15 MeV beam, it is easy to see by looking at the plotted ratios that there is an underestimation of dose by XVMC (BM) near the penumbra region. For all phantoms for the 15 MeV beam (see Figure 4- 19(b), Figure 4- 20(b), Figure 4- 21(b) and Figure 4- 22(b)), it seems that a more accurate choice of energy for the beams would improve the results slightly. The way the energy optimisation was performed, i.e. matching calculated and measured R_{50} within 0.4 mm (see section II.C), explains in part this observation.

IV Conclusions

In this study, EGSnrc and the *fast Monte Carlo* system XVMC were validated against measurements for determining the dose distribution in clinically relevant phantoms. Percent depth dose measurements were performed using TLD detectors in SW, SW/bone and

SW/lung phantoms. Profiles were measured at 3 different depths with an electron diode in a phantom consisting of water and a different number of aluminium rods. Overall, the agreement between XVMC, EGSnrc and measurements is better than 2% except in lung at 15 MeV where differences are up to 4% are observed and in some regions of the 2-D heterogeneity phantoms. Possible reasons for these discrepancies were suggested. The good agreement between XVMC and EGSnrc as well as accurate measurements and the speed improvement make XVMC very promising for Monte Carlo based electron beam treatment planning. However, for the accelerator used (Clinac 18), the parameter fit limitations in the standard XVMC beam model introduce systematic discrepancies near the beam penumbra.

References:

[1]M. Fippel, "Fast Monte Carlo dose calculation for photon beams based on the VMC electron algorithm," Med. Phys. **26**, 1466-1475 (1999).

[2]I. Kawrakow and M. Fippel, "Investigation of variance reduction techniques for Monte Carlo photon dose calculation using XVMC," Phys Med Biol **45**, 2163-2183. (2000).

[3]I. Kawrakow and D. W. O. Rogers, "The EGSnrc Code System: Monte Carlo simulation of electron and photon transport," Technical Report PIRS-701, National Research Concil of Canada, Ottawa, Canada (2000).

[4]P. R. Almond, P. J. Biggs, B. M. Coursey *et al.*, "AAPM's TG-51 protocol for clinical reference dosimetry of high-energy photon and electron beams," Med. Phys. **26**, 1847-1870 (1999).

[5]D. W. Rogers, B. A. Faddegon, G. X. Ding *et al.*, "BEAM: a Monte Carlo code to simulate radiotherapy treatment units," Med. Phys. **22**, 503-524. (1995).

[6]A. Kosunen and D. W. Rogers, "Beam quality specification for photon beam dosimetry," Med. Phys. **20**, 1181-1188. (1993).

[7]D.T. Burns, G.X. Ding, and D.W.O. Rogers, "R50 as a beam quality specifier for selecting stopping-power ratios and reference depths for electron dosimetry," Med. Phys. **19**, 317-323 (1996).

[8]I. Kawrakow, M. Fippel, and K. Friedrich, "3D electron dose calculation using a Voxel based Monte Carlo algorithm (VMC)," Med. Phys. **23**, 445-457 (1996).

[9]J. Tickner, "Particle transport in inhomogeneous media," Programme of the Monte Carlo 2000 Meeting, Lisbon , 22-23 (2000).

Chapter 5

Summary and Future Work

I Summary

The main objective of this thesis was to examine whether the *fast Monte Carlo* system XVMC could calculate dose distributions in phantoms made of materials of clinical interest with accuracy comparable to well-benchmarked general-purpose Monte Carlo code EGSnrc. The 9 and 15 MeV beams on the Clinac 18 were modeled and compared to accurate measurements. Overall, the agreement between calculations and measurements was excellent.

Percent depth doses were measured with TLDs in SW, SW/bone and SW/lung phantoms. The calculations were in agreement with measurements to well within 2% except at certain depths in the SW/lung slab phantom. For the latter case, these discrepancies were mainly attributed to the fact that the lung equivalent material used in the experiments, although being non-uniform, was assumed in the calculations to have a uniform density.

Lateral profiles were measured with an electron diode in water phantoms containing a different number of immersed aluminium rods. In general, the calculations were in agreement with measurements to within 2%, except on the edge of most lateral profiles when using

XVMC with the beam model option. This was due to the inability of the beam model to simulate the Clinac 18, the applicator of which produces a large amount of low energy electrons.

The precision in the energy tuning required for the simulation of the Clinac 18 has been revealed to be significant, mostly in the case of lateral profiles. The uncertainty in the knowledge of the fluence perturbation correction factors explains part of the small remaining disagreement between calculations and measurements.

II Future work

For such a comparison between calculation and measurements to be improved, all detector related correction factors must be known accurately. The fluence perturbation correction factors play an important role in these corrections and a further study of the magnitude of this correction as a function of different parameters is recommended. It has been shown that this correction is more important for low mean electron energies at depth. A systematic study of this should be performed. Furthermore, a practical method is needed to characterise the mean energy as a function of depth in heterogeneous phantoms of clinical interest without having to resort to sophisticated Monte Carlo calculations.

The present work shows that good accuracy can be achieved when the density of the material is well known. However, for a Monte Carlo system to become clinically useful it also needs reliable density and interaction coefficient information from CT digitised phantom information.

List of Figures

Chapter 1 Introduction

Chapter 2 The Physics of Electron Beam Therapy

Chapter 3 Monte Carlo Techniques

Chapter 4 Experimental Verification of Monte Carlo Calculated Dose Distributions for Clinical Electron Beams

List of Tables

Chapter 4 Experimental Verification of Monte Carlo Calculated Dose Distributions for Clinical Electron Beams

Bibliography

P. R. Almond, P. J. Biggs, B. M. Coursey *et al.*, "AAPM's TG-51 protocol for clinical reference dosimetry of high-energy photon and electron beams," Med. Phys. **26**, 1847-1870 (1999)..5, 67

American Association of Physicists In Medicine AAPM TG-21, RTC Task Group, "A Protocol for the Determination of Absorbed Dose from High-Energy Photon and Electron Beams," Med. Phys. **10**, 741-771 (1983).....32, 32

Frank H. Attix, *Introduction to radiological physics and radiation dosimetry* (Wiley & Son, New York, 1986).....21

M. J. Berger, "Monte Carlo calculation of the penetration and diffusion of fast charged particles," in *Methods in Comput. Phys.*, edited by B. Alder, S. Fernbach, and M. Rotenberg (Academic, New York, 1963), **1**, 135-215.....41

M. J. Berger and S. M. Seltzer, ETRAN, Monte Carlo code system for electron and photon transport through extended media, RISC computer code, package CCC-107 (Oak Ridge National Laboratory, Oak Ridge, TN, 1973).....42

M. J. Berger and S. M. Seltzer, "Stopping powers and ranges of electrons and positrons," Report NBSIR 82-2550-A, National Bureau of Standards, Washington D. C. (1983).....45

H. Bethe and W. Heitler, "On the stopping of fast particles and on the creation of positive electrons," Proc. Roy. Soc. **A146**, 83-112 (1934).....19, 46

H.J. Bhabba, "The scattering of positrons by electrons with exchange on Dirac's theory of the positron," Proc. Roy. Soc. **A154**,195-206 (1936).....20

A. F. Bielajew and D.W.O. Rogers, "PRESTA: the Parameter Reduced Electron-Step Transpost Algorithm," Nuclear Instruments and Methods in Physics Reasearch **B18**, 165-181 (1987).....47

D.T. Burns, G.X. Ding, and D.W.O. Rogers, "R_{50} as a beam quality specifier for selecting stopping-power ratios and reference depths for electron dosimetry," Med. Phys. **19**, 317-323 (1996).....70

J. C. Butcher and H. Messel, "Electron number distribution in electron-photon showers," Phys. Rev. **112**, 2096-2106 (1958).....38

G. Comte de Buffon, "Essai d'arithmétique morale," in *Supplément à l'Histoire Naturelle volume 4* (1777).....37

F. Daniels, C.A. Boyd, and D.F. Saunders, Science **117**, 343-349 (1953).....8

E. El-Khatib, J. Antolak, and J. Scrimger, "Evaluation of film and thermoluminecsent dosimetry of high energy electron beams in heterogeneous phantoms," Med. Phys. **19**, 317-323 (1992).....10

M.M. Elkind, "DNA damage and cell killing: cause and effect?," Cancer **56**, 2351-2363 (1985).....2

M. Fippel, "Fast Monte Carlo dose calculation for photon beams based on the VMC electron algorithm," Med. Phys. **26**, 1466-1475 (1999).....10, 56, 61

R. L. Ford and W. R. Nelson, "The EGS Code system - Version 3," Stanford Linear Accelerator Center Report SLAC-210 (Stanford Calif.) (1978).....45

M. L. Goldberger, "The interaction of high energy neutrons and heavy nuclei," Phys. Rev. **74**, 1269-1277 (1948).....38

S. Goudsmit and J. L. Saunderson, "Multiple Scattering of Electrons," Phys. Rev. **57**, 24-29 (1940).....25

J.G. Holt, G.R. Edelstein, and T.E. Clark, "Energy Dependance of the Response of Lithium Fluoride TLD Rods in High Energy Electron Fields," Phys. Med. Biol. **20**, 559-570 (1975)....8

ICRU, "Determination of absorbed dose in a patient irradiated by beams of X or gamma rays in radiotherapy procedures," ICRU Report 24, International Commission on Radiation Units and Measurements, Washington D.C. (1976).....2

ICRU, "Radiation dosimetry : electron beams with energies between 1 and 50 MeV," ICRU Report 35, International Commission on Radiation Units and Measurements, Bethesda, Maryland (1984).....32

ICRU, "Stopping powers for electrons and positrons," ICRU Report 37, International Commission on Radiation Units and Measurements, Bethesda, Maryland (1984)..19, 19, 21, 45

ICRU, "Photon, Electron, Proton and Neutron Interaction Data for Body Tissues," ICRU Report 46, Interantional Commission on Radiation Units and Measurements, Bethesda, Maryland (1992).....56, 56

I. Kawrakow, M. Fippel, and K. Friedrich, "3D electron dose calculation using a Voxel based Monte Carlo algorithm (VMC)," Med. Phys. **23**, 445-457 (1996).....10, 53, 54, 56, 75

I. Kawrakow, "Improved modelling of multiple scattering in the Voxel Monte Carlo model," Med. Phys. **24**, 505-517. (1997).....55

I. Kawrakow and D. W. O. Rogers, "The EGSnrc Code System: Monte Carlo simulation of electron and photon transport," Technical Report PIRS-701, National Research Concil of Canada, Ottawa, Canada (2000).....10, 49, 61

I. Kawrakow and M. Fippel, "Investigation of variance reduction techniques for Monte Carlo photon dose calculation using XVMC," Phys Med Bio21 **45**, 2163-2183. (2000).....56, 61

H.W. Koch and J.W. Motz, "Bremsstrahlung Cross-section Formulas and Related Data," Review of Modern Physics **31**, 920-955 (1959).....46

A. Kosunen and D. W. Rogers, "Beam quality specification for photon beam dosimetry," Med. Phys. **20**, 1181-1188. (1993).....67

T. Kron, P. Metcalfe, and T. Wong, "Thermoluminescence dosimetry of therapeutic x-rays with LiF ribbons and rods," Phys. Med. Biol. **38**, 833-845 (1993).....8

I. Lax, "Inhomogeneity corrections in electron-beam dose planning. Limitations of the semi-infinite slab approximation.," Phys. Med. Biol. **31**, 879-892 (1986).....9

C. M. Ma, E. Mok, A. Kapur *et al.*, "Clinical implementation of a Monte Carlo treatment planning system," Med. Phys. **26**, 2133-2143 (1999).....10, 10

A.F. McKinley, *Thermoluminescence dosimetry* (Adam Hilger Ltd, Bristol, 1981).....8

P. N. Mobit, G. A. Sandison, and A. E. Nahum, "Electron fluence perturbation correction factors for solid state detectors irradiated in megavoltage electron beams," Phys. Med. Biol. **45**, 255-265 (2000).....31

G. Z. Molière, "Theorie der Streuung schneller geladener Teilchen I: Einzelstreuung am abgeschirmten Coulomb-Feld," Z. Naturforsch **2a**, 133-145 (1947).....25

C. Moller, "Zur Theories des Durchgangs schneller Elektronen durch Materie," Ann. Phys. **14**, 568-577 (1932).....20, 25

A. E. Nahum, "Water/Air Mass Stopping Power Ratios for Megavoltage Photon and Electron Beams," Phys. Med. Biol. **23**, 24-38 (1978).....30

National Cancer Institute of Canada, "Canadian Cancer Statistics 2001," Toronto, Canada (2001).....1

W. R. Nelson, H. Hirayama, and D. W. O. Rogers, "The EGS4 Code system," Stanford Linear Accelerator Center Report SLAC-256 (Stanford Calif.) (1985).....10, 45

G. Rikner and E. Grusell, "General specifications for silicon diodes for use in radiation dosimetry," Phys. Med. Biol. **32**, 1109-1117 (1987).....5

D.W.O. Rogers, "Low energy electron transport with EGS," Nuclear Instruments and Methods in Physics Research **227**, 535-548 (1984).....47

D. W. Rogers, B. A. Faddegon, G. X. Ding *et al.*, "BEAM: a Monte Carlo code to simulate radiotherapy treatment units," Med. Phys. **22**, 503-524. (1995).....51, 67

D.W.O. Rogers, I. Kawrakow, and B. Walters, "Revised relationship between R_{50} and E_0 for electron beams," Conf. Proc. of the IEEE 2000 (2000).....32

D. W. O. Rogers, I. Kawrakow, J. P. Seuntjens *et al.*, "NRC user codes for EGSnrc," Technical Report PIRS-702, National Research Council of Canada, Ottawa, Canada (2000).....50

F. Rohlrich and B.C. Carlson, "Positron-electron differences in energy loss and multiple scattering," Phys. Rev. **93**, 38-44 (1953).....20

B. Rossi, *High Energy Particles* (Prentice-Hall, Englewood Cliffs NJ, 1952).....25

J. Seuntjens, A. Van Der Plaetsen, and H. Thierens, "Comparison of measured and calculated dose distributions in lung after electron beam treatment of the chest wall," Med. Phys. **21**, 1959-1968 (1994).....10

K. R. Shortt, C. K. Ross, A. F. Bielajew *et al.*, "Electron beam dose distributions near standard inhomogeneities," Phys. Med. Biol. **31**, 235-249 (1986).....9, 10

L.V. Spencer and F.H. Attix, "A theory of cavity ionization," Radiat. Res. **3**, 239-254 (1955)..10

R. M. Sternheimer, "Density Effect for the Ionization Loss of Charged Particles in Various Substances," Atom. Data and Nucl. Data Tables **30**, 261-271 (1984).....46

Supplement to the recommendations by the Nordic Association of Clinical Physics NACP, "Electron Beams with Mean Energies at the phantom surface below 15 MeV," Acta Radiol. Oncol. Rad. Phys. **20**, 402-415 (1981).....32

S.M. Sze, *Physics of Semiconductor devices* (Willey, New York, 1969).....5

J.Tickner, "Particle transport in inhomogeneous media," Programme of the Monte Carlo 2000 Meeting, Lisbon , 22-23 (2000).....82

S. M. Ulam and J. von Newmann, "On combination of stochastic and deterministic processes," Bull. Amer. Math. Soc. **53**, 1120 (1947) 37

J. Van Dyk (editor), *The modern technology of radiation oncology : a compendium for medical physicists and radiation oncologists* (Medical Physics Pub., Madison, Wis., 1999).....2

A. A. Varfolomeev and I. A. Svetlolobov, "Monte Carlo calculations of electromagnetic cascades with account of the influence of the medium on bremsstrahlung," Soviet Physics JETP **36**, 1263-1270 (1959).....38

R. R. Wilson, "Monte Carlo study of shower production," Phys. Rev. **86**, 261-269 (1952).....38